UNDERSTANDING TYPE IA SUPERNOVA SPECTRA

by

Kevin D. Wilk

B.S. of Physics, University of Illinois at Chicago, 2012

B.S. of Mathematics, University of Illinois at Chicago, 2012

M.S. of Physics, University of Pittsburgh, 2014

Submitted to the Graduate Faculty of

the Kenneth P. Dietrich School of Arts and Sciences in partial fulfillment

of the requirements for the degree of

Doctor of Philosophy

University of Pittsburgh

2019

UNIVERSITY OF PITTSBURGH

DIETRICH SCHOOL OF ARTS AND SCIENCES

This dissertation was presented

by

Kevin D. Wilk

It was defended on

14 December 2018

and approved by

Dr. D. John Hillier, Department of Physics and Astronomy

Dr. Carles Badenes, Department of Physics and Astronomy

Dr. Michael Wood-Vasey, Department of Physics and Astronomy

Dr. Adam Leibovich, Department of Physics and Astronomy

Dr. Matthew Walker, Department of Physics, Carnegie Mellon University

Dissertation Director: Dr. D. John Hillier, Department of Physics and Astronomy

D. John Hillier

UNDERSTANDING TYPE IA SUPERNOVA SPECTRA

Kevin D. Wilk, PhD

University of Pittsburgh, 2019

Some stars end their lives in spectacular explosive deaths called supernovae. We understand this process happens in predominantly two ways, the collapse of the stellar core in massive stars or the thermonuclear explosion of white dwarf (WD) stars at or near the Chandrasekhar mass (M_{Ch}). This thesis focuses on the thermonuclear supernovae, called Type Ia (SNe Ia). Despite the decades of theoretical work and observational constraints of SNe Ia coming from WDs, the nature of the progenitor systems and explosion scenario is unknown. The fundamental questions still unanswered are: "Do SNe Ia come from WDs with non-degenerate companions or WD companions?" and "How/why do WDs explode?" To investigate the nature of SNe Ia, I performed time series radiative transfer calculations of various hydrodynamic ejecta models. Since we cannot observe the explosion itself, spectra are tools to probe the progenitor properties. My aims were to determine ejecta mass diagnostics of SNe Ia by comparing radiative transfer calculations of four hydrodynamic ejecta models in the mass range of 1.0–1.7 M_{Ch}. Because nebular spectra are dominated by emission lines from the innermost part of the ejecta, I also investigate the physics of nebular SN Ia spectra to determine the properties of the progenitor and explosion physics. The luminosity of SNe Ia is powered by the radioactive decay of ^{56}Ni and subsequent decay of ^{56}Co. Gamma-rays produced during these decays scatter in the ejecta before either escaping or being absorbed. This thesis contains work modeling the gamma-ray flux and energy deposition function. To date, SN2014J is the only SN Ia with gamma-ray observations. Detailed gamma-ray modeling will be compared to all future observations to add additional constraints on the production of ^{56}Ni and ejecta density structure.

TABLE OF CONTENTS

LIST OF TABLES

LIST OF FIGURES

LIST OF EQUATIONS

PREFACE

"Somewhere, something incredible is waiting to be known."–Carl Sagan

Without the continued help of John Hillier, this thesis would not be possible. His patience never faltered, while entertaining my incessant barrage of questions. Encouraging me to always "stop and think," John has fostered much of my scientific growth. Learning from him has truly been inspiring, and I am honored to have learned even a small fraction of his knowledge and skills. He and his wife Janice have been real friends to me these past 6+ years, and for that I am grateful. I would also like to thank my collaborator Luc Dessart for all of the help and feedback with my research that he has given me. I would like to thank my committee members – Carles Badenes, Michael Wood-Vasey, Adam Leibovich, and Matthew Walker – for their constructive criticism and encouragement.

I would also like to thank all of my teachers that have gotten me to this point. I would like to thank my undergraduate professors Wai-Yee Keung and Mark Schlossman for encouraging me to go forward with graduate school. Of the many professors I have had at the University of Pittsburgh, I have had the most fun and interesting experiences learning from Adam Leibovich, Ayres Freitas, Carles Badenes, Arthur Kosowsky, and Jeffrey Newman. Leyla Hirschfeld is really the glue holding this graduate program together, and without her, I would be lost. Leyla keeps the ball rolling and looks out for all of us.

I am very grateful to also have my fellow graduate students/friends off whom I have bounced ideas and questions. Héctor Martínez Rodriguez and Brian Flores have been on the receiving end of many questions and always willing to help. I would also like to thank my many friends and roommates in graduate school that have made this experience palatable – Dritan Kodra, Kara Ponder, Tim Licquia, Sumit Sarbadhicary, Louis Lello, Daniel Wiegand, Nathan Herring, Cat Fielder, Daniel Perrefort, and many others.

Saving the best for last, I would like to dedicate this thesis to my parents for everything they have done and given to me to get me where I am today. If not for my father, David Wilk, who showed me the night sky through a telescope and encouraged me to be curious about the cosmos, and my mother, Frances Wilk, who encouraged my scientific curiosity by teaching me about biology and medicine, my path in life may not have brought me to Pittsburgh to pursue a Ph.D. in physics and astronomy. I would like to thank my brother, Daniel Wilk, who has encouraged me to get after what I want out of life. His intrigue and questions about the universe remind me why I love astronomy and physics when I lose perspective. If not for my oldest brother Joseph Wilk, who has lived in Pittsburgh since 2000, I would never be here at the University of Pittsburgh getting my Ph.D. He guided my transition to moving here and getting acclimated. Lastly, I owe many thanks to my partner, Olivia Lanes, for putting up with all of my stress and idiosyncrasies. Olivia has given me my most valued memories in graduate school, and for that I am grateful. I hope this partnership lasts as long as this Ph.D.

1 INTRODUCTION

Humans have been staring up at the sky for as long as we have been on this Earth. While most of their attention was placed on planets against the backdrop of the stars and constellations, new luminous and long lasting (weeks to months) objects in the sky garnished special attention. These most luminous (a few hundred million to a few billion times more luminous than the sun) new objects called "guest stars" or "new stars," seen in the sky over in the millennia, are what we know today as supernovae. The less luminous events are known as novae. Within the last century, our observational capabilities have led us to uncover many mysteries, but there is still much to discover. We began to understand how stars fuse elements, the advent of quantum mechanics allowed us to understand white dwarf stars and even predict neutron stars, and general relativity predicted black holes. As Dr. Carl Sagan famously said, "We are made of star stuff." Whether the atoms inside us were fused inside stars or from their very deaths, we are connected to the universe atomically, and Dr. Sagan so beautifully remarked, "we are the way for the universe to know itself." This thesis will focus on supernovae known as Type Ia, which will be explained below. Understanding the progenitor systems of these supernovae will better improve their use as cosmological probes (Riess et al., 1998; Perlmutter et al., 1999), and it will allow us to probe binary stellar evolution.

1.1 HISTORICAL PERSPECTIVE

Some of the first known recorded observations of supernovae were conducted by Chinese astronomers. Over a period of 1500 years, seven supernovae were observed in the night sky

before the advent of modern astronomy. These seven historical supernovae are the following: SN185, SN393, SN1006, SN1054 "Crab Nebula", SN1181, SN1572 "Tycho SN", SN1604 "Kepler SN" (Stephenson & Clark, 1976). It is important to distinguish between these long lasting new stars and those that were visible to older civilizations for much shorter durations. Classical novae, which are just minor thermonuclear explosions off a white dwarf's surface, only last for weeks and are 10 thousand times less luminous than SNe.

Prior to 1000 A.D., much of what we know about these historical SNe comes almost exclusively from Chinese astronomers, who were employed by the Chinese royal court (Green, 2015). After 1000 A.D. many monasteries around Europe began recording events in the sky ranging from comets to eclipses, but these events also included two SNe. Most notably, these supernovae are SN1006 (which was as bright as the moon) and SN1054, the supernova that gave rise to the Crab Nebula and the pulsar within that remnant.

The two famous historical supernovae SN1572 (also called Tycho's supernova) and SN1604 (also called Kepler's supernova), which occurred after the scientific revolution, have been a unique subject of study in modern times due to the observational records taken at the time. SN1604 was carefully observed not only by Kepler and David Fabricius but also by astronomers in the Far East, while Tycho's supernova was written about at length in his memoirs (Stephenson & Clark, 1976). Tycho first discovered his SN on the 11^{th} of November 1572, at a time when the heavens were believed to be immutable, and it was as bright as Jupiter. Shortly after its discovery, it became as bright as Venus and was visible during the day for two weeks. Tycho's supernova would be undetectable by March of 1574 (Dick, 2013). Based on Tycho's observations, Walter Baade was able to produce a light curve (Stephenson & Clark, 1976), resembling that of a Type Ia SN (see section 1.2).

A few years after the death of Tycho Brahe, Johannes Kepler was able to observe the supernova named after him. His first observation came on 17 October 1604, eight days after others had first observed it. From his observations, Kepler determined it was celestial (i.e. beyond that of the moon, planets, and comets) based on parallax measurements (Dick, 2013). For Kepler's supernova, Baade also reconstructed a light curve, which resembled that of a Type Ia, much like that of Tycho's supernova.

The distinction made earlier regarding the difference between classical novae and supernovae carries important historical significance. Until extra-galactic observations were made, there was no distinction between "classical-novae" and "super-novae", henceforth referred to as novae and supernovae. The people who coined the term supernova(e) were Walter Baade and Fritz Zwicky in 1934 (Baade & Zwicky, 1934b). Their paper titled "On Super-Novae" (Baade & Zwicky, 1934b) begins reading:

> The extensive investigations of extragalactic systems during recent years have brought to light the remarkable fact that there exist two well-defined types of new stars or novae which might be distinguished as *common novae* and *super-novae*. No intermediate objects have so far been observed.

Although previous conceptions of a separate class of novae already existed, it took the ability to accurately measure absolute magnitudes and luminosities to distinguish a separate class. Once astronomers were able to determine luminosities, Swedish astronomer Knut Lundmark wrote of "giant novae", "much more luminous novae", and "upper class novae." Around that same time, Edwin Hubble referred to them as "exceptional novae" (Dick, 2013).

Baade and Zwicky in 1934 tried to make sense of supernovae by using the visual magnitude photometric observations taken of SN1885 in Andromeda. To interpret the data, they assumed that the visual luminosity arises from the Rayleigh-Jeans tail of a blackbody. With their simplistic approach, they constrain the radius of the event to be less than 400 $R_\odot$ with a temperature of a few by 10^5 K. A follow-up paper to their original Baade and Zwicky paper of 1934 hypothesized that these objects are the transitional phase of a massive star into a neutron star (Baade & Zwicky, 1934a). It would take many more observations of supernovae before researchers understood progenitor systems and supernovae as a separate class with sub-classes of their own.

1.2 SUPERNOVA TYPES

As more observations of supernovae were made, including spectral observations, the need to classify them became apparent. In 1941, Rudolph Minkowski developed a classification scheme to discern various types of supernovae (Minkowski, 1941). His classification method

was to first discern between the presence/absence of hydrogen. Type II supernovae were those that showed emission near Hα, while those of Type I did not. The advent of larger telescopes and charged-coupled devices in the 1980s caused an increase in observations of SNe, necessitating the need to further subdivide the classes of Type I and Type II (Wheeler & Levreault, 1985; Elias et al., 1985; Branch, 1986; Wheeler & Harkness, 1990). Type I are further sub-divided into three main sub-classes: strong Si II (Ia), strong He I (Ib), and lacking both strong Si II and strong He I (Ic) (Filippenko, 1997). Figure 1 depicts the tree classification scheme showing the sub-classes of SNe. Type II sub-classes are predominantly

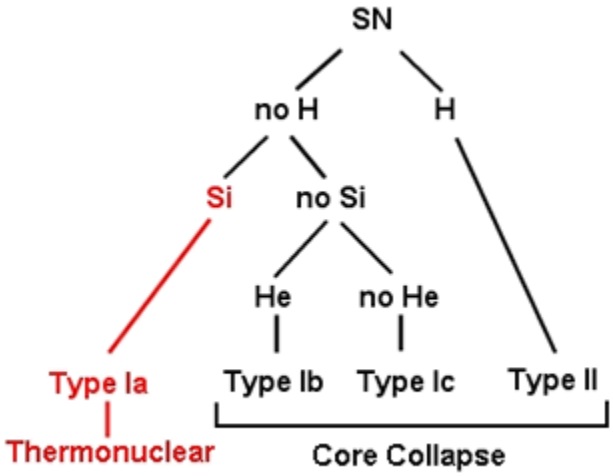

Figure 1 Spectral classification scheme of supernovae.

made by photometric classification rather than spectral classification. The main Type II classifications are plateau (II-P) and linear (II-L). Type II-P exhibit a plateau phase in their light curve post maximum, where the luminosity roughly remains constant. Type II-L, on the other hand, exhibit a linear decline in their light curve post maximum (Filippenko, 1997). This clear dichotomy may not actually exist, as there seems to be a continuous distribution from II-P to II-L (Anderson et al., 2014; Galbany et al., 2016). There is also a sub-class Type IIb where the SN begins as a Type II but evolves towards a Type Ib. Type II supernovae that have a narrow hydrogen emission component are designated as IIn (Filippenko, 1997). These spectral classifications are a way to organize all of the observations, but are not necessarily representative of the physical scenarios that produce the SNe. The physical scenarios are explained below.

1.2.1 Core-Collapse

When massive stars reach the end of their lives, they have built up an onion-like structure with an iron core surrounded by silicon, oxygen, neon, carbon, helium, and the outermost layer of hydrogen. The gravitational energy release from the core collapsing powers the explosion. The remaining stellar envelope begins to collapse alongside the core. The core's collapse is halted by the formation of a (proto) neutron star as the inner core's collapse overshoots its equilibrium state, causing it to bounce back and produce a shock propagating outwards. The resulting dynamics of the explosion is thought to be driven by a small fraction of the neutrino luminosity ($\sim 10^{53}$ ergs) being deposited into the stellar envelope or magnetorotational effects to revive the stall (Janka, 2012; Burrows, 2013; Janka, 2017; Müller, 2017).

All core-collapse supernovae (CCSNe) are believed to explode this way. The evidence suggests that all Type II, Ib, and Ic explode as CCSNe. The explanation why CCSNe are not all classified as the same type or sub-type is related to the envelope mass and composition. When a massive star explodes we observe very different properties of its evolution based on how much hydrogen is present in the envelope. Massive stars that explode as red supergiants are observed as II-P supernovae and stars with little hydrogen mass (or early circumstellar material interaction – see Morozova et al. (2017)) are observed as II-L. The strength of the plateau is related to the hydrogen as the ionization front moves through the hydrogen-rich envelope. It is believed that Wolf-Rayet stars (like WC, WO, and WN stars) are the progenitors of Ib and Ic SNe as they have lost the entirety of their hydrogen envelope (thus the Type I classification). It is believed that the remnant of a CCSNe will be a neutron star or pulsar. It is unclear whether some CCSNe produce black holes. The rest of the thesis will not focus on understanding CCSNe, but instead on thermonuclear supernovae.

1.2.2 Thermonuclear

For nearly 60 years, the astrophysics community has believed that SNe Ia are the thermonuclear explosions of degenerate material, i.e. a white dwarf (WD) star (Hoyle & Fowler, 1960; Woosley et al., 1986). This thermonuclear reaction happens at or near the center of the WD

when the temperature and density are high enough ($T \sim 10^9$ K, $\rho \sim 10^9$ g cm^{-3}) to ignite the degenerate carbon-oxygen (C/O) WD (at or near the Chandrasekhar mass $\sim$1.4 M$_\odot$). The burning produces unstable isotopes (with ^{56}Ni as the most abundant isotope) and stable isotopes with often most of the stable mass in iron group elements (IGEs) and the rest as intermediate mass elements (IMEs). Details about the explosion scenarios are discussed in section 1.4. The production of ^{56}Ni is responsible for the thermal evolution of SNe Ia after the explosion (Colgate & McKee, 1969; Arnett, 1982). The ^{56}Ni decays into ^{56}Co, releasing 1.718 MeV in γ-rays (available as a heating source to the gas). However, ^{56}Co is itself unstable and decays into ^{56}Fe releasing 3.633 MeV in γ-rays and 0.116 MeV in kinetic energy by release of positrons (an additional heating source along with the γ-rays). Without this non-thermal energy source, SNe Ia would not be the incredibly luminous events we see in the sky. The ejecta rapidly expands with large hydrodynamic velocities ($\sim 10^4$ km s^{-1}) from a small progenitor. Without additional energy, the ejecta quickly cool.

Because the luminosity of these thermonuclear SNe is powered by the production and decay of the ^{56}Ni in WDs of nearly the same mass, the brightness of SNe Ia is correlated with the rate at which their light curves (LCs) decline after maximum light. This is known as the width luminosity relation (WLR). The relationship indicates that brighter SNe Ia decline in the B-band more slowly than less luminous SNe Ia. The characteristic parameter used to measure the decline is known as $\Delta M_{15}(B)$, which is the difference in magnitude at maximum and 15 days after maximum (Phillips, 1993). After the discovery of the WLR, astronomers quickly used the relationship as a means to turn SNe Ia into standardizable candles (see Figure 2) for determination of distances. Riess et al. (1998); Perlmutter et al. (1999) used their accurate distances to measure the expansion rate of the universe. This lead to the discovery of dark energy and secured them the Nobel Prize in 2011.

1.3 TYPE IA PROGENITOR CHANNELS

While it is generally accepted that the progenitor system of a SNe Ia involves at least one WD, the progenitor system is not well-known as it has never been directly detected. All evidence

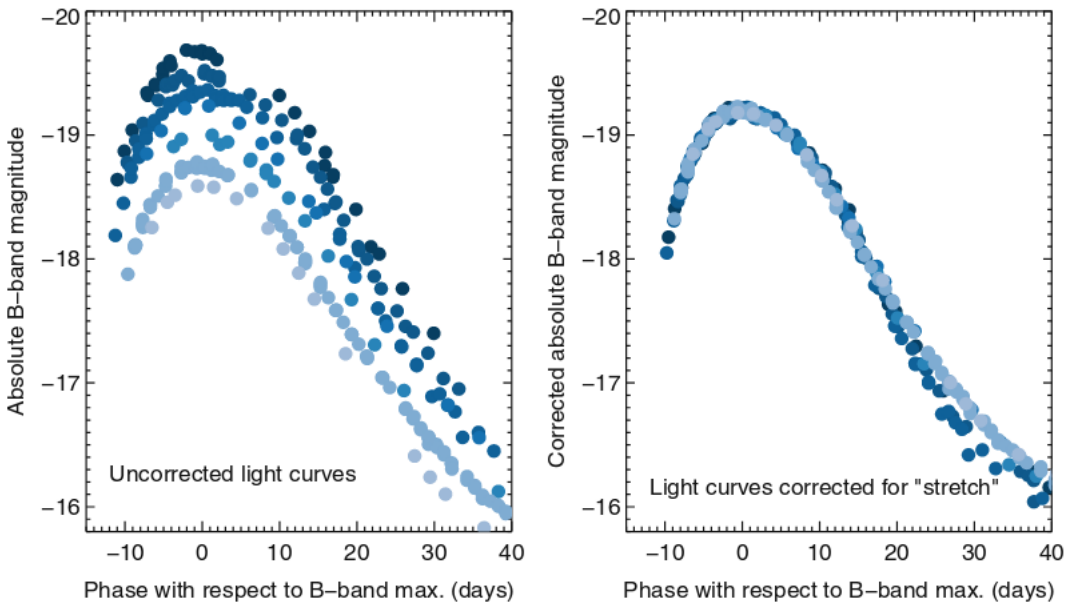

Figure 2 The absolute B-band magnitude light curves with respect to time (figure 2 from Maguire (2017) used with permission). The WLR is that brighter SNe Ia have wider light curves. Cosmologists can then correct for this stretch (seen in the right plot) when using SNe Ia as standardizable candles.

of progenitor systems comes from indirect evidence (e.g. delay time distribution constraints, remnant mass ratios, lack of hydrogen and/or shock interaction with companion).

1.3.1 Single Degenerate Scenario

The single degenerate (SD) scenario is the "classic" story (the one often taught to introductory astronomy students) in which SNe Ia originate when a C/O WD accretes from a non-degenerate companion. The WD then approaches what is known as the Chandrasekhar mass (M_{Ch}) limit, and a thermonuclear explosion ensues (Whelan & Iben, 1973; Nomoto, 1982). The non-degenerate companion can either be a main sequence dwarf, a subgiant, a giant, or a helium star and it typically transfers mass via Roche lobe overflow (RLO). RLO means the material flows through the critical gravitational equipotential point known as the L1 Lagrangian point – see Figure 3. Accretion is not limited to just RLO. In symbiotic systems, wind mass-loss can mediate the mass transfer (see review Maoz et al., 2014).

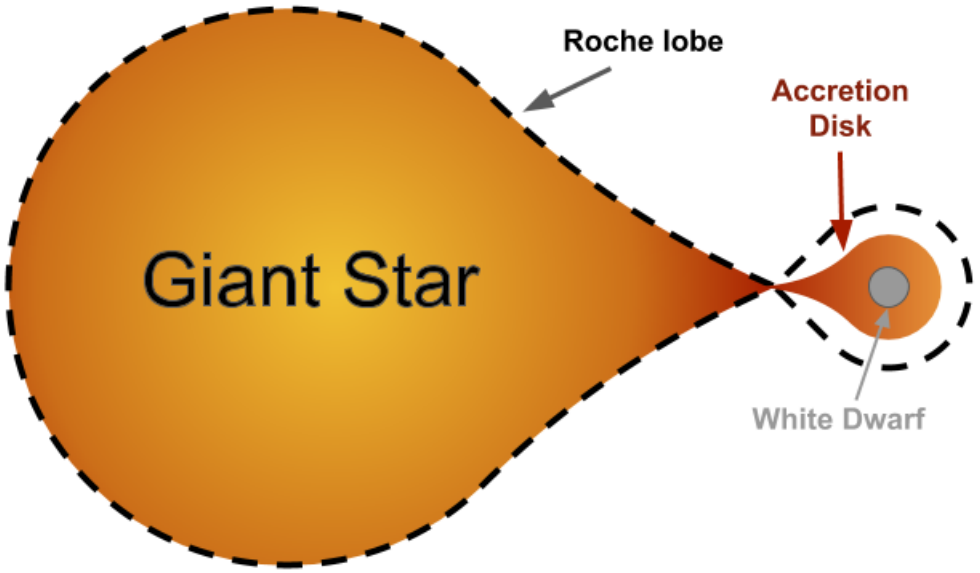

Figure 3 Roche lobe overflow scenario in the SD channel.

The SD channel requires some fine-tuning of the mass accretion rate onto the WD (Nomoto, 1982). For WDs of about 0.8 (1.4) $M_\odot$ the stable accretion rate of hydrogen is in a narrow range of about a factor of three around $\dot{M} = 10^{-7}$ (5×10^{-7}) $M_\odot$ year^{-1}. As the WD accretes from its companion, mass can be lost via nova eruptions, winds from the accretion disk, or helium flashes. High accretion can lead to the formation of a red-giant-like phase (Iben & Tutukov, 1984), and if the accretion process is too slow, then a cold degenerate accretion layer can form until it ignites in a thermonuclear nova outburst (Starrfield et al., 1972).

Recent observations and modeling suggest recurrent novae could be progenitors of SNe Ia (Darnley et al., 2015; Hillman et al., 2016). As long as the WD retains some mass after each explosion, the WD may reach M_{Ch}. Currently, there are 400 known novae in the Milky Way, but only 10 of those are known to be recurrent novae (Darnley et al., 2015). More galactic novae could be recurrent, but the timescale for the next eruption could be longer than our current observations. These systems broaden the parameter space of SD progenitors for SNe Ia.

1.3.2 Double Degenerate Scenario

In the double degenerate (DD) channel, two degenerate WDs (the primary being a C/O WD) give rise to a SN Ia (Iben & Tutukov, 1984; Webbink, 1984). The way in which two WDs come together to give rise to a SN Ia can happen in multiple ways. Two WDs can directly collide (also called a violent merger), the primary WD can accrete material from the secondary, or the system can form in what is known as a core-degenerate scenario.

The classical picture of the merger scenario is that the system loses angular momentum via gravitational wave emission. The less massive WD is tidally disrupted and begins accreting onto the more massive primary WD. However, depending on the mass ratio between the two WDs, this merger process can occur in different ways (Sato et al., 2015). Provided both WDs are within a mass range of 0.9–1.1 $M_{\odot}$, an explosion can take place during the merger phase. If these masses are less, then the merger can cause the temperature to increase, lifting degeneracy and expanding the material, thereby quenching the thermonuclear runaway (Pakmor et al., 2010). However, if the primary is much more massive, then the explosion can take place during the merger remnant phase. Typically in the merger scenario, half of the secondary WD is lost to the primary, while the rest forms a debris region around the primary. Very little mass is expected to be ejected during the merger process ($\sim 10^{-3}$ $M_{\odot}$).

The collision scenario is believed to exist in much denser stellar systems, such as globular clusters which contain many older stellar populations. This collision typically involves interaction within a triple system (Kushnir et al., 2013). This scenario gained further interest when it was shown that the collision can lead to a SN Ia under certain circumstances (Hawley et al., 2012). Early models focused on head-on collisions, but others have worked to explore the parameter space of mass, velocities and impact parameters, and core composition. Head-on collisions allowed the systems to explode in just one mass transfer event, while grazing collisions required several mass transfer episodes.

While the DD would explain the lack of observed companions in SNe Ia remnants, this channel does have issues. Rapid accretion of carbon and oxygen can lead to off-center ignitions before the WD collapses and turns into an oxygen-neon WD (Saio & Nomoto,

1985). Rapid mass transfer can also prompt the collapse of the WD into a neutron star without leading to a SN Ia.

1.4 TYPE IA EXPLOSION SCENARIOS

In either the SD or DD channel, triggering the thermonuclear runaway and the subsequent SN Ia is inevitable. How this occurs has been a matter of study for decades. Over the years different explosion mechanisms have been proposed including pure detonations/supersonic burning (Arnett, 1969), pure deflagration/subsonic burning (Nomoto et al., 1976), delayed detonation and pulsating delayed detonation (Khokhlov, 1991a,b; Gamezo et al., 2005; Livne et al., 2005; Röpke & Niemeyer, 2007; Jackson et al., 2010; Seitenzahl et al., 2013), gravitationally-confined detonation (GCD) (Plewa et al., 2004; Seitenzahl et al., 2016), and double detonations for sub-M_{Ch} WDs (Woosley & Weaver, 1994; Livne & Arnett, 1995; Fink et al., 2007, 2010).

Pure detonation models have just a pure supersonic burning front. In this explosion scenario, a large amount of ^{56}Ni is produced ($\sim 0.8-0.9$ $M_{\odot}$). In the pure deflagration explosion scenario, the flame propagates subsonically allowing for the WD to expand, lowering the fuel density and suppressing the amount of ^{56}Ni produced, while enhancing the production of intermediate elements (IMEs). One of the most successful theories at reproducing standard SNe Ia observables is the delayed detonation transition (DDT) model. The DDT model begins as a deflagration front and transitions to a detonation at some density ρ_t. This model is artificial, but it is able to reproduce the chemical stratification observed in "standard" SNe Ia spectra (i.e. a balance of IMEs and ^{56}Ni). Pulsational delayed detonations (PDD) are similar to DDT models except that the burning is halted before the WD is completely unbound, after which gravity causes the bound material to infall, triggering a detonation at some transition density. This leaves the outer material largely unburnt and unaffected by the interior detonation, while showing lower expansion velocities than a standard DDT model (Hoeflich et al., 1996a, and references therein).

GCD is a type of explosion mechanism by which the WD undergoes a deflagration phase that creates buoyancy-driven bubbles which rise to the surface. The bubbles break out of the WD surface still confined by the gravity of the WD and spread laterally across the surface of the WD. This creates an ignition on the opposite side of the WD and subsequent final explosion (Plewa et al., 2004). This model generates inhomogeneities and enhances the possible mixing between burnt layers.

The double detonation model involves a sub-M_{Ch} C/O WD and a He WD. The C/O WD accretes helium from the donor, until the built-up helium ignites on the surface, creating a pressure wave towards the center. The central density is then high enough to ignite ^{12}C in a final detonation. Early models suggested that an appreciable helium layer (~ 0.2 $M_\odot$) was necessary to trigger ignition in the center (Nomoto, 1982; Woosley et al., 1986). Such a larger helium ash layer would certainly have an observable effect on early-time spectra and light curves. However, recent modeling suggests that this layer may need not be as large (10 – 100 times smaller) in order to trigger ignition in the center (Bildsten et al., 2007; Shen & Bildsten, 2014) and leave few signatures on the spectra.

1.5 SPECTRA OF TYPE IA SUPERNOVAE

SNe Ia form a relatively homogeneous spectroscopic class of objects, making them ideal for cosmological distance indicators. Their early spectra all share the identifying Si II λ6347, 6371 (often collectively called λ6355), Ca II H&K lines $\lambda\lambda$3934, 3968, as well as the Ca II NIR triplet $\lambda\lambda$8498, 8542, 8662 (Filippenko, 1997). Iron (such as Fe II) accounts for most of the spectral features once the photosphere recedes inwards ($t \gtrsim 2$ weeks). The early spectrum is dominated by electron scattering and line scattering (Hoeflich et al., 1986), while much of the nebular spectrum is emission from forbidden transitions.

As more SNe Ia were discovered, it was apparent that subtypes exist within SNe Ia. Early attempts to distinguish SNe Ia broke them into "normal" and "peculiar" (Branch et al., 1993). The historical archetypes of peculiar SNe Ia are SN1991bg and SN1991T (Filippenko, 1997), with many blurring the line between "normal" and "peculiar" SNe Ia. Subtypes are thought to come from not only differences in progenitor systems or explosion mechanisms but also differences in the structure of the SN ejecta – i.e. density, abundances, and temperature, etc. (Nugent et al., 1995; Lentz et al., 2000; Benetti et al., 2005; Branch et al., 2009; Höflich et al., 2010; Dessart et al., 2014a). Some attempts to classify SNe Ia distinguished them by Si II absorption (Branch et al., 2006; Blondin et al., 2012) by relating the pseudo-equivalent widths (pEWs[1]) of the Si II features around 5750 and 6100 Å at maximum. These subtypes were called 'core-normal', 'broad-line', 'cool', and 'shallow-silicon' (Branch et al., 2006).

Branch et al. (2006) argued that core-normal SNe Ia form a relatively homogeneous sample with nearly identical pEWs of the 6100 Å feature. Noted differences are the Ca II NIR triplet at high velocity in some objects. Broad-line subtypes are also "normal" in the usual sense, but they differ from core-normal SNe by having much broader 6100 Å absorption. Cool subtypes have similar 6100 Å absorption to those of core-normal, but unlike core-normal, they show a strong absorption trough between 4000-4400 Å, associated with Ti II. Shallow-silicon is an inhomogeneous subtype with a unifying low value of pEWs of 5750 and 6100 Å. The cool and shallow-silicon types are shown against a core-normal subtype in Figure 4.

1.5.1 Pre-Maximum

After the explosion, the ejecta is optically thick and much of the spectrum is determined by the outermost part of the ejecta (up until ∼5 days prior to maximum). Due to the explosion physics discussed in section 1.4, the spectrum is predominantly composed of IME features such as calcium, silicon, sulfur, oxygen, and magnesium with absorption profiles indicating velocities of 10 000–25 000 km s^{-1} (Maguire, 2017). Additionally, iron and cobalt

[1]pEWs are distinguished from equivalent widths (EWs). A distinction is made because SNe Ia have no true continuum like stars. The continuum is typically approximated in SNe as a straight line between the peaks on either side of an absorption profile.

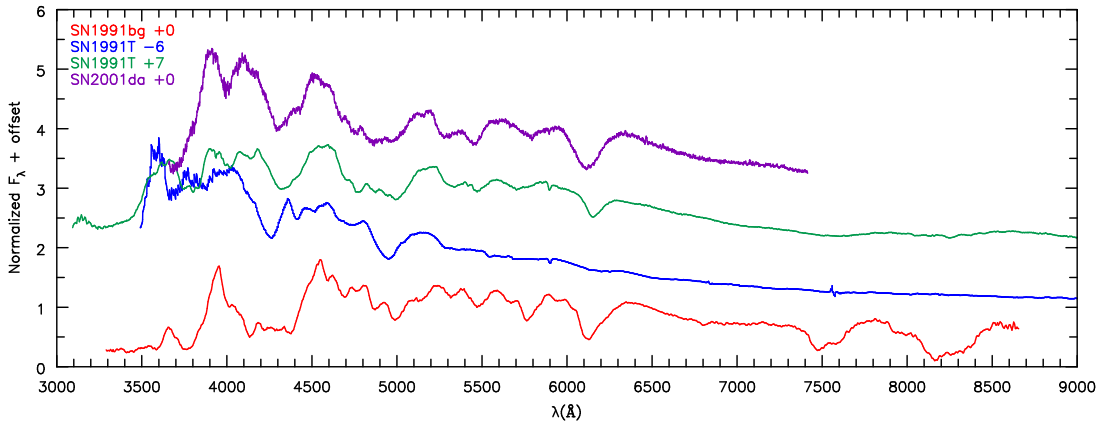

Figure 4 Peculiar cool (SN1991bg) and shallow-silicon (SN1991T) subtypes for comparison against a "normal" broad-line (SN2001da) subtype. The numbers to the right of the SN name indicate the phase (in days) relative to time of B-band maximum.

also contribute absorption, particularly towards the UV (Filippenko, 1997). Examples of pre-maximum spectra are plotted in Figure 5.

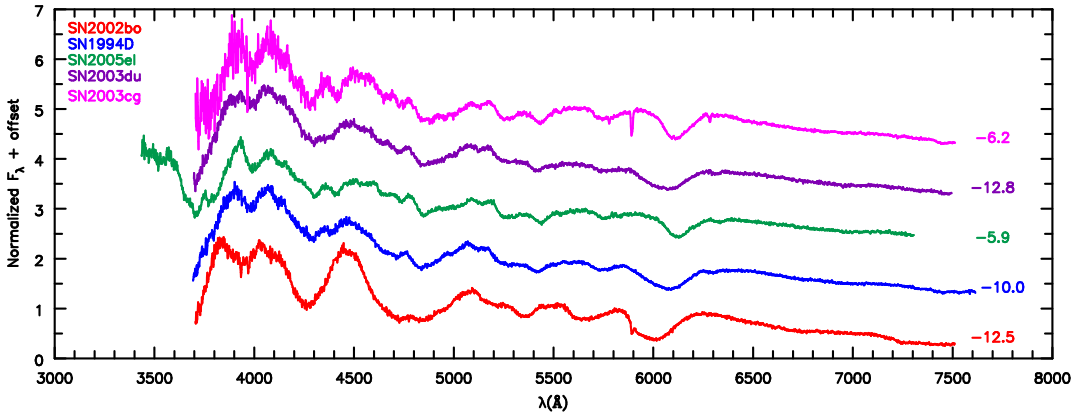

Figure 5 Pre-maximum spectra of five SNe Ia. The numbers to the right of the spectra indicate the phase (in days) relative to time of B-band maximum. SN2002bo and SN2003cg have been de-reddened with values ($E(B-V)$=0.41, R_V=3.1) and ($E(B-V)$=1.15, R_V=2.0) respectively. The spectra have been normalized such that the integral between 4000-7000 Å of $F_\lambda \mathrm{d}\lambda$ is 1 erg cm^{-2} s^{-1} Å^{-1}. Spectra taken from public CfA data.

Some early-time spectra also show high velocity features (HVFs) (particularly with

the Ca II NIR triplet and less often with the Si II λ6355 doublet), which are absorption features that exhibit velocities a few thousand km s^{-1} higher than the photospheric component. The two strongest lines in the Ca II NIR triplet (λ8542 and λ8662) are separated by roughly 4000 km s^{-1}, and this can complicate the interpretation of the Ca II profile. Early observations of SN2011fe ($\sim$1.5 days after explosion) even showed signs of high velocity O I $\lambda\lambda$7772, 7774, 7775 (Nugent et al., 2011). HVFs help constrain the explosion scenario (e.g. PDD vs. DDT) by constraining where the mass is in the ejecta.

Diversity in early spectra of SNe Ia is not only limited to differences in pEWs but also includes differences in the velocity of the centroid absorption components for many IME features (Blondin et al., 2012). For example, absorption centroids for Si II λ6355 can vary between roughly $-10\,000$ and $-20\,000$ km s^{-1}, however the emission peak generally tends to be around $\sim -6\,000$ km s^{-1}. The velocity of the emission peak might indicate the presence of steep density gradients that restrict the emission and absorption regions (Dessart & Hillier, 2005b). In roughly 30% of SNe Ia, the emission profile of Si II λ6355 shows C II λ6580 absorption in pre-maximum spectra (Parrent et al., 2011). This evidence of unburnt carbon in SNe Ia helps shed light on the physics of the explosion.

1.5.2 Maximum

Much of the classification of SNe Ia into subtypes is done by comparing spectra at maximum light (B-band maximum). However, their spectra are largely homogeneous (see figure 11 Blondin et al., 2012). Many of the IME features are still present at maximum (Si II λ6355, Si II λ5972, Si II λ4130, Ca II NIR triplet, Ca II H&K lines, and the S II "w" feature near 5400 Å), although features from IGEs are becoming stronger in absorption (Fe II, Fe III, and Co II). Examples of maximum spectra are plotted in Figure 6. Because of the degeneracy between luminosity and temperature, the presence of the O I λ7774 triplet can distinguish between SNe Ia of different luminosities, with its presence predominantly in lower luminosity SNe Ia (Nugent et al., 1995).

Typically, at maximum, the spectral color begins to shift redward because much of the decay luminosity has began to escape during the expansion, allowing the ejecta to cool.

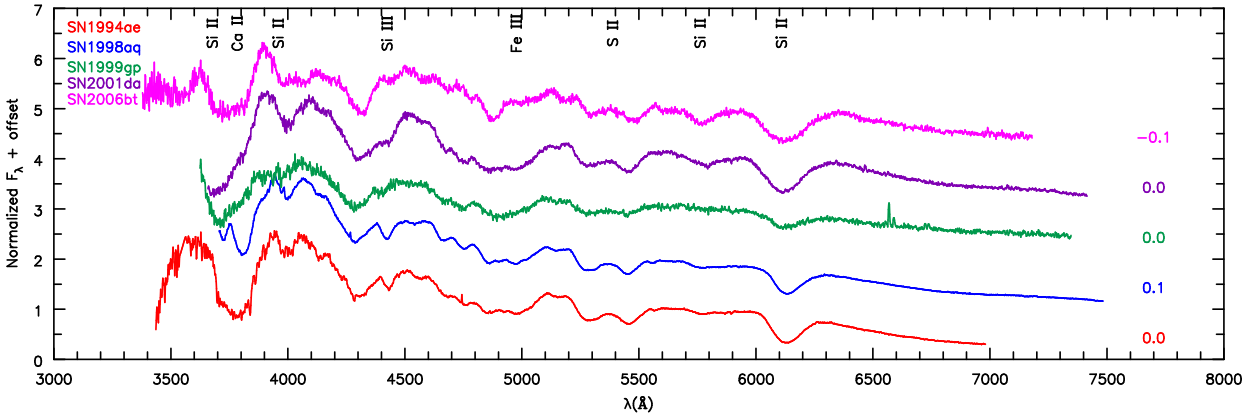

Figure 6 Maximum spectra of five SNe Ia. The numbers to the right of the spectra indicate the phase (in days) relative to time of B-band maximum. The spectra have been normalized such that the integral between 4000-7000 Å of $F_\lambda \mathrm{d}\lambda$ is 1 erg cm^{-2} s^{-1} Å^{-1}. Spectra taken from public CfA data.

As this "photosphere" begins to recede inwards, the centroid absorption velocities begin to shift toward lower velocities. Typical absorption centroid velocities now range between 8 000 - 15 000 km s^{-1} (Maguire, 2017). At this stage, many of the HVFs observed in pre-maximum spectra begin to fade. Some SN Ia spectra still show HVFs persisting until or just after maximum (Silverman et al., 2015).

1.5.3 Post-Maximum

After maximum, the iron and cobalt features begin to dominate the spectra. The photosphere continues to recede inwards, and the velocities of many features fall below 8 000 km s^{-1}. Features from IMEs (such as the Ca II NIR triplet and Si II λ6355) continue to persist. During this time, the spectra show forbidden transitions such as [Fe III] λ4658.

1.5.4 Nebular Phase

At late times ($\gtrsim$ 100 days) the photosphere has completely receded and the ejecta is optically thin to both continuum and many lines, although some transitions are optically thick (like

many UV transitions). The luminosity at nebular times is powered by the decay of ^{56}Co (the decay luminosity deposited is the luminosity emitted by the ejecta via line emission – see section 1.7.1). The spectra (optical and near infrared) is dominated by emission lines of forbidden transitions of IGEs, reflecting the NSE burning. Lines by IMEs may still be present like the Ca II NIR triplet; [Ca II] $\lambda\lambda$7291, 7324; [S II] λ10320; [S III] $\lambda\lambda$9068, 9530.

Nebular lines have been observed with shifts of a few thousand km s^{-1} (either towards blue or red) in their centroid emission, interpreted as an off-center ignition (Maeda et al., 2010b; Maguire et al., 2018). Typical line velocities are a few thousand km s^{-1}, often indicating the width of the emitting region (Jerkstrand, 2017). It has even been shown that the ^{56}Ni mass can be determined by measuring the late-time line emission of [Co III] λ5893 (Childress et al., 2015). Because nebular spectra reflect the very interior parts of the SN ejecta, understanding nebular spectra can help to place constraints on the conditions of the explosion (such as central density and on/off center).

1.6 RADIATIVE TRANSFER

The way to uncover the nature of SNe Ia is by understanding their spectral evolution. In order to do this, it is necessary to simulate the explosions of WDs by means explained in section 1.4. However, SNe are observed after the explosion has taken place. Therefore, it is necessary to perform radiative transfer simulations using the hydrodynamic explosion models to support or rule out certain possibilities. The following is mostly based on Hubeny & Mihalas (2014).

1.6.1 Radiative Transfer Equation

The radiation transport equation describes changes in the specific intensity (I_ν) as the radiation propagates. The specific intensity is the amount of energy (dE) that passes through a surface $d\vec{A}$ at position $\vec{r}$ into a solid angle $d\Omega$ from direction $\hat{n}$ in a time interval dt and

frequency interval $(\nu, \nu + d\nu)$. Formally, I_ν is defined as

$$dE = I_\nu(\vec{r}, \hat{n}, t)\hat{n} \cdot d\vec{A}d\Omega d\nu dt = I_\nu(\vec{r}, \hat{n}, t)dA\cos\theta d\Omega d\nu dt \qquad [\text{ergs}], \tag{1.1}$$

where $\cos\theta$ accounts for the component of $\hat{n}$ perpendicular to the surface $d\vec{A}$. Equation 1.1, however, ignores polarization of the radiation field.

In 1D, integration of the specific intensity I_ν against powers of $\cos\theta$ for all solid angle $d\Omega$ relates to physically meaningful quantities called the *moments of the radiation field*. If we assume azimuthal symmetry (i.e. $I_\nu \neq I_\nu(\phi)$), then the moments are defined (for $\mu = \cos\theta$) as

$$[J_\nu, H_\nu, K_\nu, \ldots] = \frac{1}{2}\int_{-1}^{1}[\mu^0, \mu^1, \mu^2, \ldots]I_\nu d\mu. \tag{1.2}$$

Here, θ is the angle between the normal to the atmosphere/ejecta and the direction of the beam of radiation – see Figure 7. From equations 1.1 and 1.2, it is obvious that J_ν (also called the 0^{th} moment or the mean intensity) relates to the chromatic energy density (U_ν) as

$$U_\nu = \frac{4\pi}{c}J_\nu \tag{1.3}$$

The flux (F_ν) that one measures (in a telescope for instance) is related to the 1^{st} moment of the radiation (also called the Eddington flux) field by

$$H_\nu = \frac{1}{4\pi}F_\nu, \tag{1.4}$$

and the radiation pressure is related to the 2^{nd} moment of the radiation field by

$$P_\nu^{(\text{rad.})} = \frac{4\pi}{c}K_\nu, \tag{1.5}$$

and for an isotropic radiation field

$$P_\nu^{*\,(\text{rad.})} = \frac{1}{3}U_\nu^* \Rightarrow K_\nu = \frac{1}{3}J_\nu \tag{1.6}$$

As I_ν propagates through space and time, processes can contribute to the field or remove energy/photons from the radiation field. Processes such as scattering, absorption, and emission

modify the radiation field. The changes to the radiation field are described by the radiative transfer equation. The radiative transfer equation is

$$\frac{1}{c}\frac{\partial I_\nu}{\partial t} + \hat{n}\cdot\vec{\nabla} I_\nu = \eta_\nu - \chi I_\nu, \tag{1.7}$$

where $\eta_\nu = \eta(\vec{r}, \hat{n}, \nu, t)$ is the emission coefficient (either thermal or scattering redistribution) and $\chi_\nu = \chi(\vec{r}, \hat{n}, \nu, t)$ is the extinction coefficient (such as absorption or scattering).

As for radiative transfer in massive stars with expanding atmospheres, it is more convenient to go to the comoving frame (CMF) for radiative transfer in SN ejecta. Scattering, redistribution, and emission are also simplified in the CMF as the emissivity and opacity can be often assumed to be isotropic. The transfer equation can be written for all orders of (v/c) in the CMF as

$$\begin{aligned}\frac{\gamma}{c}(1+\beta\mu)\frac{\partial I_\nu}{\partial t} + \gamma(\mu+\beta)\frac{\partial I_\nu}{\partial r} + \gamma(1-\mu^2)\left[\frac{1+\beta\mu}{r} - \Lambda\right]\frac{\partial I_\nu}{\partial \mu} \\ -\gamma\nu\left[\frac{\beta(1-\mu^2)}{r} + \mu\Lambda\right]\frac{\partial I_\nu}{\partial \nu} + 3\gamma\left[\frac{\beta(1-\mu^2)}{r} + \mu\Lambda\right] I_\nu = \eta_\nu - \chi_\nu I_\nu,\end{aligned} \tag{1.8}$$

where $\beta = v/c$, $\gamma = 1/\sqrt{1-\beta^2}$, $\mu = \cos\theta$, and

$$\Lambda = \frac{\gamma^2(1+\beta\mu)}{c}\frac{\partial \beta}{\partial t} + \gamma^2(\mu+\beta)\frac{\partial \beta}{\partial r}. \tag{1.9}$$

1.6.2 Moment Equations of the Radiative Transfer Equation

The moments of the radiation field discussed above have useful application in radiative transfer theory. For instance, J_ν is used in the rate equations (see sections 1.7.2 and 1.8) and the energy balance equations. If we integrate equation 1.8 against $d\Omega$, take first order in v/c, and define $D/Dt = \partial/\partial t + v\partial/\partial r$ for spherical symmetry, then we obtain the following moment equations of the spherical radiative transfer equation:

$$\frac{1}{cr^3}\frac{D(r^3 J_\nu)}{Dt} + \frac{1}{r^2}\frac{\partial(r^2 H_\nu)}{\partial r} - \frac{\nu v}{rc}\frac{\partial J_\nu}{\partial \nu} = \eta_\nu - \chi_\nu J_\nu \tag{1.10}$$

and

$$\frac{1}{cr^3}\frac{D(r^3 H_\nu)}{Dt} + \frac{1}{r^2}\frac{\partial(r^2 K_\nu)}{\partial r} + \frac{K_\nu - J_\nu}{r} - \frac{\nu v}{rc}\frac{\partial H_\nu}{\partial \nu} = -\chi_\nu H_\nu. \tag{1.11}$$

In order to close these moment equations, it is customary to introduce a factor f_ν (called the Eddington factor), defined by

$$f_\nu = K_\nu / J_\nu. \tag{1.12}$$

The Eddington factor is motivated such that when the radiation field is isotropic we expect $f_\nu = 1/3$, while the Eddington factor approaches 1 near the outer boundary. In the moment equations, f_ν is assumed to be known, while J_ν and η_ν are determined. In order to calculate f_ν, the formal solution to the relativistic radiative transfer equation is used where χ_ν and η_ν are known. Let us now focus on the sources of extinction that go into equation 1.8.

1.6.3 Opacity

Much of the interaction of radiation with matter in SN Ia ejecta is electron scattering and line scattering (Hoeflich et al., 1986; Wagoner et al., 1991). Electron scattering is simply Thomson scattering (σ_e) off free electrons in the ejecta, which is coherent in the frame of the electron. Unlike electron scattering, line scattering is a bound-bound process where a photon is absorbed by a bound electron, exciting the electron to a higher level, and then being re-emitted in another direction as the electron decays back down to its original level.

Velocity gradients in SN ejecta complicate line transfer. Velocity gradients create Doppler shifts between regions in the ejecta and also between the ejecta and observer. This

sets up resonance zones, which are regions of constant velocity. Any observed frequencies must have come from such a resonance zone. If we consider a frequency observed at ν, then its frequency in the CMF is denoted as

$$\nu' = \nu\,\gamma(1 - \mu V/c). \tag{1.13}$$

SN ejecta expand as a Hubble flow ($V = a \cdot r$ for a constant a), so using the geometry of Figure 7 we can write the relationship between the observed and CMF frequency (to first order in V/c) as

$$\nu' = \nu(1 - \mu \cdot ar/c) = \nu(1 - (z/r) \cdot ar/c) = \nu(1 - az/c). \tag{1.14}$$

This means that the observed frequencies associated with a single transition come from a plane of constant z emitted in the ejecta. This effect also describes the optical depth of an emission line from a particular point interacting with other line transitions as it travels through the ejecta. Doppler shifts in the ejecta define the other lines that can interact with the emission line. Each interaction will occur at a particular resonance zone $z_{\rm res}$, which is unique to the emission frequency and interacting line frequency. The optical depth arising from multiple lines can be quite large.

1.7 NEBULAR PHYSICS

At late times, the optical depth drops significantly, and the time dependence becomes negligible. Nebular spectra can largely be understood by time independent transfer of optically thin emission lines from forbidden transitions. Much of the emission comes from collisionally excited lines that have excitation energies of a few eV. The following is based on Hubeny & Mihalas (2014) and Osterbrock & Ferland (2006).

1.7.1 Energy Balance

Since the time dependence has become negligible, the luminosity deposited by non-thermal processes like γ-rays and positrons is the luminosity radiated by the ejecta. The forbidden lines in the ejecta act as strong coolants and dominate the energy loss, so we can represent the energy balance as

$$E_\gamma + E_{\rm pos} \simeq L_{\rm C}, \tag{1.15}$$

where E_γ [ergs s^{-1} cm^{-3}] is the energy deposited from γ-ray scattering, $E_{\rm pos}$ [ergs s^{-1} cm^{-3}] is the energy deposited (assumed local) by the kinetic energy of the positrons emitted from radioactive decays, and $L_{\rm C}$ [ergs s^{-1} cm^{-3}] is the cooling function from bound bound transitions. The cooling function can be written as

$$L_{\rm C} = \sum_{k=1}^{N_{\rm ion}} \sum_{j=1}^{N} n_{j[k]} \sum_{i<j} A_{ji[k]} h\nu_{ij[k]}, \tag{1.16}$$

where $n_{j[k]}$ [cm^{-3}] is the atomic population of the $j^{\rm th}$ level for the $k^{\rm th}$ ion, $A_{ji[k]}$ [s^{-1}] is the Einstein A coefficient for the transition from level j to level i for the $k^{\rm th}$ ion, and $h\nu_{ij[k]}$ [ergs] is the energy of the transition from level j to level i for the $k^{\rm th}$ ion. In order to determine which lines will have the largest contribution to the right hand side in equation 1.16, the ionization structure and level populations need to be determined allowing for coupling to the radiation field.

1.7.2 Radiative and Collisional Processes

Many of the emission lines in nebular spectra can be understood by radiative and collisional processes in statistical equilibrium. The radiation field J_ν does influence the emission of lines that are coupled to UV transitions where the optical depth can still be large. The simplified rate equations can be written as

$$\sum_{k=1}^{N_{\rm ion}} \sum_{i=1}^{N} \frac{D(n_{i[k]}/\rho)}{\rho Dt} \equiv 0 = \sum_{k=1}^{N_{\rm ion}} \left[\sum_{j\neq i} (n_{j[k]} P_{ji[k]}) - n_{i[k]} \sum_{j\neq i} P_{ij[k]} \right], \tag{1.17}$$

where $D/Dt \equiv \partial/\partial t + v \cdot \partial/\partial r$ for spherical symmetry and

$$P_{ij} = R_{ij} + n_e C_{ij}. \tag{1.18}$$

R_{ij} is the radiative rate from level $i \rightarrow j$, n_e is the electron density, and C_{ij} is the collision rate from level $i \rightarrow j$. The collision rates are functions of temperature and given by

$$C_{ij} = \frac{8.629 \times 10^{-6}}{\sqrt{T}} \frac{\Upsilon_{ij}(T)}{g_i} \exp(-h\nu_{ij}/k_B T) \ \ [\mathrm{cm}^3\ \mathrm{s}^{-1}] \quad \text{and} \quad C_{ji} = \frac{g_i}{g_j} C_{ij} \exp(h\nu_{ij}/k_B T), \tag{1.19}$$

where $g_{i/j}$ are the statistical weights for levels i/j and $\Upsilon_{ij}(T)$ is the velocity averaged collision strength and has a weak dependence on temperature.

The radiative rates are defined as

$$R_{ij} = B_{ij}\bar{J}_{ij} \ \ [\mathrm{s}^{-1}] \qquad \text{and} \qquad R_{ji} = A_{ji} + B_{ji}\bar{J}_{ij} \ \ [\mathrm{s}^{-1}], \tag{1.20}$$

where $B_{ij/ji}$ are the Einstein B coefficients and $\bar{J}_{ij}$ is frequency averaged mean intensity. For many optical and near infrared transitions, $B_{ij/ji}\bar{J}_{ij}$ can be ignored to understand the emission features.

Once an ionization structure is calculated using CMFGEN, one can calculate a simple emission spectrum for each ionization species. For lines that are blended with two or more transitions, calculating an emission spectra highlights the relative contribution of each component to the total feature.

1.8 RADIATIVE TRANSFER CODE: CMFGEN

CMFGEN is a radiative transfer code originally developed to study the atmospheres and winds of massive stars (Hillier, 1987, 1990; Hillier & Miller, 1998), and was later developed to study SNe (Dessart & Hillier, 2005a,b, 2008, 2010; Hillier & Dessart, 2012). CMFGEN is a one dimensional (1D) radiative transfer code that solves the radiative transfer equation in conjunction with the statistical equilibrium equations in the CMF for spherically symmetric hydrodynamic winds or SN ejecta. It is used with one of three main modes to treat line transfer (blanketing, Sobolev, or CMF). The most successful option to date is the blanketing mode which treats line overlap and the effect of lines on the continuum energy distribution. CMFGEN contains two main programs. The first program is cmfgen_dev.exe and is used to

compute the atmospheric structure. The second is called cmf_flux.exe, and it is used to calculate the observed spectrum after cmfgen_dev.exe has reached convergence.

To solve for the radiation field, CMFGEN solves the spherically symmetric moment equations (see section 1.6.2) in the CMF. CMFGEN linearizes the moments of the transfer equation using a radial grid, discretized into ND radial points ($R = \{R_i, i = 1, .., ND\}$). The moment equations are often more stable for convergence and simplify non-coherent electron scattering by integrating out angular redistribution. However, as mentioned earlier, a formal solution is necessary to obtain I_ν so that f_ν can be computed. I_ν can then be transformed at the outer boundary to obtain an observer's frame spectra.

The relativistic radiative transfer equation (equation 1.8) is written in spherical coordinates, but it is often convenient to use a different coordinate system using z and parallel rays defined by a set of impact parameters ($P = \{p_i, i = 1, .., NP\}$), where NP is the number of impact parameters. The spherical relativistic radiative transfer equation can be transformed from $(r, \mu) \rightarrow (p, z)$ meaning that these rays are characteristics to the relativistic radiative transfer equation. CMFGEN also includes an additional number of rays (NC) that strike the core radius (R_{ND}), such that $NP = ND + NC$. See Figure 7 for the spatial grid geometry used in CMFGEN.

Mentioned earlier in section 1.7.2, there is coupling of the atomic level populations to the radiation field and vice versa. This complicates solving the relativistic radiative transfer equation and statistical equilibrium equations self-consistently. To achieve consistency, CMFGEN linearizes the statistical equilibrium equations and radiative transfer equation. Consider a vector ψ_d for ($d = 1, \ldots, ND$), NF frequencies, and N atomic levels

$$\psi_d = \{\bar{J}_{1d}, \ldots, \bar{J}_{md}, \ldots, \bar{J}_{NFd}, n_{1d}, \ldots, n_{kd}, \ldots, n_{Nd}, n_{e,d}, T_d\}. \tag{1.21}$$

Then the statistical equilibrium equations (one for each atomic level) can be represented by

$$\mathcal{M}_d(\psi_d) = 0. \tag{1.22}$$

For each iteration, the radiation field is calculated. However, the statistical equilibrium equations are not satisfied. Instead, $\mathcal{M}_d(\psi_d) = \Delta\mathcal{M}_d$, which is linearized as

$$\delta\mathcal{M}_d \cdot \delta\psi_d = -\Delta\mathcal{M}_d, \tag{1.23}$$

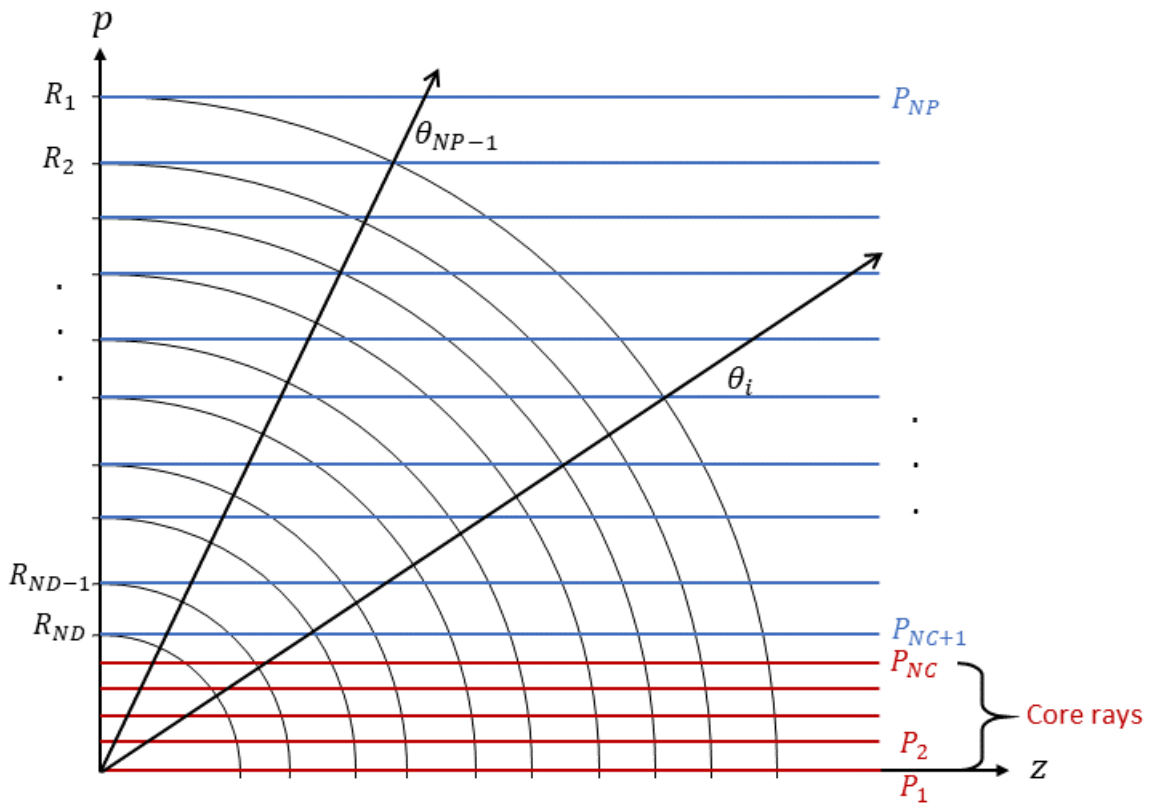

Figure 7 Model grid setup for CMFGEN. The black lines show the radius vectors. To obtain $I(r,\theta)$ we integrate along each impact parameters.

or as

$$\frac{\partial \mathcal{M}_d}{\partial \bar{J}_{1d}}\delta\bar{J}_{1d} + \ldots + \frac{\partial \mathcal{M}_d}{\partial \bar{J}_{NFd}}\delta\bar{J}_{NFd} + \frac{\partial \mathcal{M}_d}{\partial n_{1d}}\delta n_{1d} + \ldots + \frac{\partial \mathcal{M}_d}{\partial n_{Nd}}\delta n_{Nd} + \frac{\partial \mathcal{M}_d}{\partial n_{e,d}}\delta n_{e,d} + \frac{\partial \mathcal{M}_d}{\partial T_d}\delta T_d = -\Delta\mathcal{M}_d. \quad (1.24)$$

We use the linearized transfer equation to eliminate J_{id}. This gives rise to either block diagonal or block tri-diagonal systems of linear equations. Solutions of these equations give the corrections to the populations. This process is iterated until convergence in the radiation field and populations is achieved.

Unlike some other codes, CMFGEN does not assume LTE, an assumption that is untenable for low density plasmas like in SNe ejecta (or winds of hot massive stars) where radiative processes can dominate over collisional processes. In non-LTE, the atomic level or

ionic populations are also coupled to the radiation field, which is not characterized by the local electron temperature. CMFGEN uses large atomic data models with thousands of levels.

One approximation available in CMFGEN is the use of super-levels. The concept of super-levels is an approximation used in non-LTE such that a set of atomic levels (all of which may be out of LTE with respect to levels outside that set) are all in LTE with respect to all others in that set. The levels in a super-level share similar level excitation energies or other properties. The super-level is treated as one level in CMFGEN in the statistical equilibrium equations, and the level populations within the super-level are determined by their LTE value. As CMFGEN iterates to achieve convergence, typical corrections to level populations tend to form a geometric series, and this allows acceleration techniques to assist convergence.

CMFGEN allows for various inner boundary conditions to solve the moment equations. The inner boundary conditions in CMFGEN are the following:

i) Diffusion Approximation – The source function is a power series expansion of the Planck energy distribution, i.e. the flux at the inner boundary is proportional to the temperature gradient.

ii) Zero Flux – At the inner boundary, $I_\nu^+ = I_\nu^-$ for the formal solution, and $H_\nu = 0$ for the moment solution.

iii) Hollow Core – This option is similar to Zero Flux, but it allows for frequency shifts due to velocity shifts across the hollow core.

At early times during the photospheric phase, the diffusion approximation is typically used for SNe, and at later times, either a hollow core or zero flux is used.

To solve the coupled equations, CMFGEN utilizes several different methods to achieve convergence of the atmospheric structure. These methods are a Λ-iteration, full linearization, or an Ng-acceleration. Described below are the different techniques.

i) Λ-iteration – This iteration assumes that all δJ_{id} and δT terms in equation 1.24 are zero. The mean intensity is solved by means of a Lambda operator, assuming the source function is known ($J_\nu = \Lambda[S_\nu]$, where $S_\nu = \eta_\nu/\chi_\nu$ is the source function). This method propagates the radiation field an optical depth at a time, and requires large numbers of

iterations for high scattering opacity. Typical convergence requires τ^2 iterations. Once J_ν is calculated, the corrections to the populations are obtained by solving the linearized rate equations (with δJ_{id} held fixed).

ii) Full Linearization – Full linearization of all terms of equation 1.24 are considered. δJ_{id} is computed in terms of the linearized populations, and then this can be used to to eliminate δJ_{id} from the linearized rate equations, allowing improved population estimates to be computed.

iii) Ng-acceleration – Once iterations have stabilized the changes and the atmospheric structure approaches convergence, an Ng-acceleration can use previous iterations to guess the populations by extrapolating their corrections (Ng, 1974). This option should not be used until at least 15 iterations have been used.

CMFGEN also incorporates additional options such as including X-rays, including micro-clumping (which has been successful at reproducing observables for WR stars), adjusting the turbulent velocity (used for determining line absorption profiles), omitting lines with small oscillator strengths, and many others.

1.8.1 CMFGEN_DEV.EXE vs. CMF_FLUX.EXE

The atmospheric/SN ejecta structure (T, ionization state, level populations, etc.) is calculated using cmfgen_dev.exe. Although cmfgen_dev.exe produces an observer spectrum, it does so by transforming the radiation field at the outer boundary from the CMF to the observer's frame. However, this is subject to frequency transfer effects and will spread line profiles towards the red side of profiles, causing a narrow Gaussian to be spread out in velocity space while preserving the overall flux. cmf_flux.exe uses the level populations and structure from cmfgen_dev.exe and transforms the opacity and emissivity into the observer's frame so that an observer's frame spectrum can be calculated. Another main difference is that, cmf_flux.exe utilizes a finer radial grid by inserting points. The emission line seen from the observer's perspective must come from a resonance zone that is a few Doppler widths wide. Because cmf_flux.exe treats many lines and needs to properly model the emission, the spacing along any ray needs to be on the order of ~ 5 km s^{-1}. Therefore, cmf_flux.exe generates a more accurate observed spectrum.

1.8.2 Model Computation

In order to run a SN ejecta model time sequence using cmfgen_dev.exe, CMFGEN requires a SN hydrodynamic file (SN_HYDRO_DATA). This file is the basis for running a model since it contains information such as the mass fractions (also isotopic mass fractions), density, and time since explosion. Running a model sequence is an initial value problem since there are D/Dt terms in both the rate equations and the moment equations. One simply cannot run each time step independently. To advance each model in time, typically a 10% increase is used until time elapsed surpasses 10 days. Each time-step is coupled to the previous time-step.

To ensure convergence of a model time-step, all of the various iteration types described above should be used. Besides the various types of iterations, other techniques may be necessary such as radial regridding, fixing the temperature, or rewinding the iterations. Each model time-step must be converged to specified a criterion before advancing in time. After a model has converged, the user needs to run cmf_flux.exe for the observer's frame calculation of the radiation field.

CMFGEN contains many diagnostic tools such as dispgen.exe – which allows the user to plot various properties of the ejecta, GEN_COOL – a file that contains the heating and cooling rates for all processes (alongside other procedures to check energy conservation during an iteration and after model convergence), and CORRECTION_SUM and CORRECTION_LINK – files containing information about atomic level convergence at various depths. All of these are designed to aid the user towards converging a model.

See Appendix B for additional information about files and important/useful options for running a SN model.

1.9 OUTLINE OF THIS THESIS

This thesis aims to study the nature of SNe Ia by understanding their spectra. To study the nature of SNe Ia, I utilize the radiative transfer code, CMFGEN, as described in section 1.8.

In chapter 2, I discuss the work to create the non-Monte Carlo radiative transfer code for γ rays. Its aims are to model the flux and energy deposition function in SNe ejecta. This work will be accepted for publication in the Monthly Notices of the Royal Astronomical Society upon minor edits. In chapter 3, I discuss the radiative transfer calculations I performed to uncover possible diagnostics of ejecta mass for SNe Ia of a fixed ^{56}Ni mass. I also compare the computed synthetic spectra to several observed SNe Ia. This work has been published in the Monthly Notices of the Royal Astronomical Society (Wilk et al., 2018). In chapter 4, I focus on investigations of nebular SN Ia spectra. I aim to uncover the important physics behind spectral formation and constrain the amount of clumping that may be present in SN Ia ejecta and deduce how it could influence SN Ia diagnostics. Lastly, in chapter 5, I discuss how the work in this thesis can be extended into future investigations of SN Ia spectra.

2 GAMMA-RAY SCATTERING AND ENERGY DEPOSITION

2.1 INTRODUCTION

Supernovae (SNe) are luminous astrophysical events, and studies of SNe probe stellar evolution of the progenitor and reveal properties of the explosion mechanism. Understanding both spectra and light curves allows us to investigate the physics and retrieve SN ejecta properties. For instance, Type Ia SNe produce large amounts of radioactive material that control the thermal evolution of the ejecta by non-thermal heating.

For decades, the standard paradigm has been that SNe arise through two mechanisms: gravitational core-collapse (CC) and thermonuclear (Type Ia). Historically, SNe have been classified into two spectral types, Type I (no H I lines) and Type II (strong H I lines) (Minkowski, 1941). However, the most successful theory of SNe is that SNe of Type Ib, Ic, and Ibc, and II result from core-collapse – see Colgate & White (1966); Burrows et al. (1995); Janka & Mueller (1996); Mezzacappa et al. (1998). On the other hand, Type Ia SNe are believed to be thermonuclear explosions of carbon-oxygen (CO) white dwarfs (WDs) (Hoyle & Fowler, 1960). These thermonuclear explosions produce large amounts of radioactive material ($\sim$0.6 $M_\odot$) (see, e.g., Scalzo et al., 2014b), mainly ^{56}Ni, which decays into ^{56}Co and then ^{56}Fe. Core-collapse SNe (CCSNe) are thought to produce about an order of magnitude less ^{56}Ni than this ($\sim 10^{-2}$–10^{-3} $M_\odot$), which is what powers the late time light curve (Janka, 2012, see review of CCSNe).

A crucial issue for modeling SNe is the location of radioactive material. If the radioactive material is mixed into the outer ejecta, it will heat it and enhance the ionization. In Type Ia SNe, mixing of ^{56}Ni has been invoked to explain the brightness and color at very early times (Höflich et al., 1998, 2002; Woosley et al., 2007; Hoeflich et al., 2017). It was

also invoked in SN1987A to explain the early detection of X-rays and γ-rays from 1987A (Pinto & Woosley, 1988a,b; Bussard et al., 1989; The et al., 1990; Dessart et al., 2012, and references therein).

The peculiar Type II SN, SN1987A, is the only CCSN for which we have detected the ^{56}Co decay lines at 847 and 1238 keV (Makino & Moore, 1987; Matz et al., 1988a,b,c,d; Sunyaev et al., 1987; Tanaka, 1988; Cook et al., 1988). After SN1987A was observed, models of expected late time (1–2 years post-explosion due to high initial column densities) γ-ray and X-ray fluxes and profile shapes calculated from Monte Carlo radiative transfer soon followed (Pinto & Woosley, 1988a,b; Bussard et al., 1989; The et al., 1990, and references therein). To date, SN 2014J is the only Type Ia SN with γ-ray detections (Churazov et al., 2014, 2015).

Many γ-ray radiative-transfer codes have utilized Monte Carlo techniques to treat the radiative transfer (Pozdnyakov et al., 1983; Hoeflich et al., 1992; Milne et al., 2004; Sim, 2007; Sim & Mazzali, 2008; Hillier & Dessart, 2012; Summa et al., 2013). Another technique, used by Swartz et al. (1995) and Jeffery (1998), utilizes a grey transfer approach to treat γ-ray transport. Swartz et al. (1995) finds that the value of $\kappa_\gamma = 0.06 Y_e$ cm^2 g^{-1}, where Y_e is the total number of electrons per baryon, best describes the interaction of γ-rays in the SN ejecta. In contrast, the work presented here is the first of its kind to formally solve the radiative transfer equation for γ-rays for SN ejecta.

This chapter is organized as follows: In section 2.2 we outline the method used to calculate the opacity (Compton scattering and X-ray photoelectric absorption) and emissivity (prompt emission and scattering) needed to solve the relativistic radiative transfer equation. The implementation of our method into CMFGEN is discussed in section 2.2.5. In section 2.3 we illustrate our results using a SN Ia ejecta resulting from a delayed-detonation in a Chandrasekhar mass (M_{Ch}) WD from Wilk et al. (2018). We also present synthetic γ-ray/X-ray spectra around bolometric maximum and at nebular times, and compare our results with those from a Monte Carlo calculation and those obtained using the grey approximation. Finally, in section 2.4, we summarize our results.

2.2 TECHNIQUE

We developed this code for implementation into CMFGEN (Hillier & Miller, 1998; Hillier & Dessart, 2012; Dessart et al., 2014c), which is a radiative transfer code that solves the spherically symmetric, non-local-thermodynamic-equilibrium (non-LTE), time-dependent, relativistic radiative transfer equation in the co-moving frame (CMF). This work was undertaken as a consistency check of the Monte Carlo (MC) radiative transfer code utilized by CMFGEN (Hillier & Dessart, 2012), and to provide an alternative technique to track photons and subsequent Compton scatterings or photon absorption for computation of the energy deposition in SNe. Since the expansion velocities dominate over thermal motions, this work ignores effects of thermal redistribution.

2.2.1 Radiative Transfer Equation

We implement the code by solving the relativistic radiative transfer equation along rays as outlined in Olson & Kunasz (1987), Hauschildt (1992), and Hillier & Dessart (2012). The relativistic radiative transfer equation is

$$\begin{aligned} &\frac{\gamma(1+\beta\mu)}{c}\frac{\partial I_\nu}{\partial t} + \gamma(\mu+\beta)\frac{\partial I_\nu}{\partial r} \\ &+\gamma(1-\mu^2)\left[\frac{1+\beta\mu}{r} - \Lambda\right]\frac{\partial I_\nu}{\partial \mu} \\ &-\gamma\nu\left[\frac{\beta(1-\mu^2)}{r} + \mu\Lambda\right]\frac{\partial I_\nu}{\partial \nu} \\ &+3\gamma\left[\frac{\beta(1-\mu^2)}{r} + \mu\Lambda\right] I_\nu \;=\; \eta_\nu - \chi_\nu I_\nu, \end{aligned} \tag{2.1}$$

where $\beta = v/c$, $\gamma = 1/\sqrt{1-\beta^2}$, $\mu = \cos\theta$, and

$$\Lambda = \frac{\gamma^2(1+\beta\mu)}{c}\frac{\partial \beta}{\partial t} + \gamma^2(\mu+\beta)\frac{\partial \beta}{\partial r}. \tag{2.2}$$

In Equation 2.1, the specific intensity, emissivity, and opacity (all measured in the CMF) are assumed to be functions of several variables [$I_\nu = I(t, r, \mu, \nu)$, $\eta_\nu = \eta(t, r, \mu, \nu)$, and $\chi_\nu = \chi(t, r, \nu)$]. However, if we ignore all time dependence, we can reduce this equation along characteristic rays reducing the partial differential equation with dependent variables

$(r,\ \nu,\ \mu)$ to a partial differential equation with dependent variables (s, ν) (Mihalas, 1980). Time dependence can be neglected as γ-rays undergo few scatterings before the energy is deposited or the photon escapes to the observer.

From Equation 2.1, our characteristic equations are

$$\frac{dr}{ds} = \gamma(\mu\ +\ \beta) \quad \text{and} \quad \frac{d\mu}{ds} = \gamma(1-\mu^2)\left[\frac{1+\beta\mu}{r}\ -\ \Lambda\right]. \tag{2.3}$$

We can now write the relativistic radiative transfer equation along a characteristic ray as

$$\frac{\partial I_\nu}{\partial s}\ -\ \nu\Pi\frac{\partial I_\nu}{\partial \nu}\ =\ \eta_\nu\ -\ (\chi_\nu\ +\ 3\Pi)I_\nu, \tag{2.4}$$

where

$$\Pi\ =\ \gamma\left[\frac{\beta(1-\mu^2)}{r}\ +\ \mu\Lambda\right] \tag{2.5}$$

In order to solve Equation 2.4, we use a backward differencing in frequency (i.e. $\partial\nu = \nu_{i-1} - \nu_i$ with i denoting the current frequency). We then solve Equation 2.4 by usual means for the formal solution along each ray for each frequency.

2.2.2 Opacities

Most nuclear decay lines in SNe have energies less than 3.5 MeV (see Table 1). For energies less than this, the dominant opacity source is Compton scattering and photoelectric absorption. Below 100 keV, the dominant opacity is photoelectric absorption and above that it is Compton scattering – (see figure 1 in Milne et al., 2004). This work only incorporates both photoelectric absorption and Compton scattering opacity. We neglect the influence of e^-e^+ pair production opacity because the typical decay γ-ray energies are less than 3.5 MeV in SNe.

For comparison with the MC method of Hillier & Dessart (2012) which follows that of Kasen et al. (2006), we use a photoelectric absorption opacity given by

$$\chi_\nu^{\rm abs} = \left(\frac{m_e c^2}{h\nu}\right)^{3.5} \sigma_{\rm T}\alpha^4 8\sqrt{2}\sum_i^{N_{\rm spec.}} N_i Z_i^5, \tag{2.6}$$

where m_e is the electron mass, $\sigma_{\rm T}$ is the Thomson cross section, α is the fine structure constant, N_i is the number density of species i, and Z_i is the atomic number of species i. The Compton scattering opacity as given by eq. 7.113 of Pomraning (1973) is

$$\chi_\nu^{\rm C} = 2\pi r_e^2 N_e \left[\left(\frac{1+x}{x^3} \right) \left\{ \frac{2x(1+x)}{1+2x} - \log(1+2x) \right\} + \frac{\log(1+2x)}{2x} - \frac{1+3x}{(1+2x)^2} \right], \tag{2.7}$$

where N_e is the number density of electrons, r_e is the classical electron radius, and x is $h\nu/m_e c^2$.

2.2.3 Emissivities

The total emissivity in the relativistic radiative transfer equation has two components. The first component is an isotropic prompt emission from nuclear decays, and the second is the scattering emissivity arising from Compton scattering.

2.2.3.1 Prompt Emission The simpler of the two, the isotropic emissivity from the prompt decays is given by

$$\eta_\nu^{\rm iso} = \frac{1}{4\pi} \sum_{i=1}^{N_{\rm isot.}} \sum_{j=1}^{N_{\rm lines}} \frac{N_i}{\tau_i} E_{ij} P_{ij} \frac{e^{-\Gamma}}{\sqrt{2\pi} V_{\rm Dop} \nu_{ij}/c}, \tag{2.8}$$

where $\Gamma = \frac{1}{2}[(\nu - \nu_{ij})/(V_{\rm Dop}\nu_{ij}/c)]^2$, N_i is the number density of the i-th species isotope, $\tau_i = (t_{1/2})_i/\ln(2)$ is the nuclear decay constant for the i-th species isotope (see Table 1 for half-lives – $t_{1/2}$ – of ^{56}Ni and ^{56}Co), $E_{ij}(\nu_{ij})$ is j-th line decay energy (frequency) for the ith species isotope, P_{ij} is j-th line decay probability for the i-th species isotope, and $V_{\rm Dop}$ is the line Doppler velocity width ($\sim$100–200 km s^{-1}).

The isotropic emission is the local source of γ-rays that eventually travel and scatter through the ejecta. Thus, it only needs to be calculated once before the transfer equation is solved.

2.2.3.2 Scattering Emissivity Unlike the prompt emission, the scattering emissivity requires more numerical/computational effort and must be calculated concurrently while solving Equation 2.4. The difficulty in calculating the scattering emissivity (Equation 2.9) is due to the complicated angle and frequency dependence of the anisotropic Klein-Nishina (KN) scattering kernel (Equation 2.11). Since we solve the specific intensity along characteristic rays for all impact parameters p_i, we have a fixed grid of polar angles θ_i (specifically $\mu_i = \cos\theta_i$) for every radius r_i – note azimuthal symmetry is assumed. The scattering emissivity for an outgoing beam of frequency ν' and direction $\mathbf{\Omega}'$ is generally defined as

$$\eta^{\rm s}_{\nu'}(r, \mathbf{\Omega}') = \int_0^\infty \frac{\nu'}{\nu} d\nu \oint d\mathbf{\Omega} \sigma_s(\nu \to \nu', \xi) I_\nu(r, \mathbf{\Omega}), \tag{2.9}$$

where the prime denotes outgoing, and $\sigma_s(\nu \to \nu', \xi)$ is the KN scattering kernel for a photon scattering with angle given as

$$\xi = \mathbf{\Omega} \cdot \mathbf{\Omega}' = \sqrt{1-\mu^2}\sqrt{1-\mu'^2}\cos(\phi - \phi') + \mu\mu'. \tag{2.10}$$

Following eq. 7.108 of Pomraning (1973), the KN scattering kernel for $x = h\nu/m_e c^2$ is given by

$$\begin{aligned} \sigma_s(\nu \to \nu', \xi) &= N_e \frac{r_o^2}{2} \frac{1}{x\nu} \left[\frac{x}{x'} + \frac{x'}{x} + 2\left(\frac{1}{x} - \frac{1}{x'}\right) + \left(\frac{1}{x} - \frac{1}{x'}\right)^2 \right] \times \\ &\quad \delta\left[\xi - \left(1 - \frac{1}{x'} + \frac{1}{x}\right)\right] \qquad (2.11) \\ &\equiv N_e \frac{r_o^2}{2} \sigma(\nu, \nu') \delta\left[\xi - \left(1 - \frac{1}{x'} + \frac{1}{x}\right)\right]. \qquad (2.12) \end{aligned}$$

Given that we assume $I_\nu \neq I_\nu(\phi)$, we need to integrate and remove the ϕ dependence in Equation 2.9. Using the relationship $\delta(f(\phi)) = \sum_i \delta(\phi - \phi_i)/|f'(\phi_i)|$ for an arbitrary function f with the zeros ϕ_i, we can transform our δ-function as

$$\begin{aligned} \delta\left[\xi - \left(1 - \frac{1}{x'} + \frac{1}{x}\right)\right] \quad \to \quad & \frac{\delta\left[\phi - \phi_1\right]}{\left|\sqrt{(1-\mu^2)(1-\mu'^2) - (1 - \frac{1}{x'} + \frac{1}{x} - \mu\mu')^2}\right|} \\ & + \frac{\delta\left[\phi - \phi_2\right]}{\left|\sqrt{(1-\mu^2)(1-\mu'^2) - (1 - \frac{1}{x'} + \frac{1}{x} - \mu\mu')^2}\right|}, \end{aligned} \tag{2.13}$$

where

$$\phi_1 = \cos^{-1}\left(\frac{1-\frac{1}{x'}+\frac{1}{x}-\mu\mu'}{\sqrt{(1-\mu^2)(1-\mu'^2)}}\right)+\phi' \qquad \text{and}$$
$$\phi_2 = 2\pi - \cos^{-1}\left(\frac{1-\frac{1}{x'}+\frac{1}{x}-\mu\mu'}{\sqrt{(1-\mu^2)(1-\mu'^2)}}\right)+\phi'. \tag{2.14}$$

Both ϕ_1 and ϕ_2 exist in $\{0, 2\pi\}$ since $\cos(\phi-\phi') = \cos(2\pi-[\phi-\phi'])$. Each delta contributes an equal value to the integral (see Equation 2.9) with respect to ϕ. Therefore, we have twice the integral of one delta function, giving us a factor of 2.

This transformation changes the μ integration limits to make sure the Compton relationship holds. To find the new μ limits, we extremize ξ with respect to ϕ evaluated at our roots (i.e. $\partial\xi/\partial\phi|_{\phi=\phi_i} = 0$). This gives us the constraint that $\phi_i - \phi' = n\pi$, for an integer n. Using this result, we find our new limits on μ to be

$$\mu_{1,2} = \frac{a_1 \pm \sqrt{a_1^2+4a_2}}{2} \tag{2.15}$$

$$\text{for} \qquad a_1 = 2\mu'\left[1+\frac{1}{x}-\frac{1}{x'}\right] \qquad \text{and}$$

$$a_2 = \left[\frac{2}{xx'}+\frac{2}{x'}-\frac{1}{x^2}-\frac{2}{x}-\frac{1}{x'^2}-\mu'^2\right].$$

We can then rewrite Equation 2.9 after integrating over ϕ as

$$\eta^{\mathrm{s}}_{\nu'}(r,\mu') = N_e r_o^2 \int_0^\infty \frac{\nu'}{\nu} d\nu\, \sigma(\nu,\nu') \int_{\mu_2}^{\mu_1} d\mu F(\nu,\nu',r,\mu,\mu'), \tag{2.16}$$

where

$$F(\nu,\nu',r,\mu,\mu') = \frac{I_\nu(r,\mu)}{\sqrt{(1-\mu^2)(1-\mu'^2)-(1-\frac{1}{x'}+\frac{1}{x}-\mu\mu')^2}}. \tag{2.17}$$

Note that we have cancelled the one half with the factor of 2 from our ϕ integration. If we look at the μ integrand in Equation 2.16 with our new μ integration limits, we run into a singularity at our limits. However, for this integral we can exploit Gauss-Chebyshev quadrature, which is defined as

$$\int_{-1}^{1} \frac{f(x)dx}{\sqrt{1-x^2}} = \sum_{i=1}^{n} \frac{\pi}{n} f(b_i), \tag{2.18}$$

for abscissa $b_i = \cos[(2i-1)\pi/2n]$ and integer n. In order to get it into the form of Gauss-Chebyshev quadrature, we can make a linear transformation of μ, namely, $w = c_1\mu + c_2$, for constants c_1 and c_2. These constants c_1 and c_2 are determined using the integration limits $\mu_{1,2}$ and solving the following linear equation:

$$\begin{pmatrix} \mu_1 & 1 \\ \mu_2 & 1 \end{pmatrix} \begin{pmatrix} c_1 \\ c_2 \end{pmatrix} = \begin{pmatrix} 1 \\ -1 \end{pmatrix}. \tag{2.19}$$

This has the solution

$$\begin{pmatrix} c_1 \\ c_2 \end{pmatrix} = \frac{1}{\mu_1 - \mu_2} \begin{pmatrix} 2 \\ -\mu_1 - \mu_2 \end{pmatrix}. \tag{2.20}$$

From the definition of $\mu_{1,2}$ in Equation 2.15 and our constants $c_{1,2}$ in Equation 2.20, we find that our integrand transforms to

$$\frac{d\mu}{\sqrt{(1-\mu^2)(1-\mu'^2) - (1 - \frac{1}{x'} + \frac{1}{x} - \mu\mu')^2}} \rightarrow \frac{dw}{\sqrt{1-w^2}}. \tag{2.21}$$

Finally, Equation 2.16 becomes

$$\begin{aligned} \eta^s_{\nu'}(r,\mu') &= N_e r_o^2 \int_0^\infty \frac{\nu'}{\nu} d\nu\, \sigma(\nu,\nu') \times \\ &\quad \sum_{i=1}^{n} \frac{\pi}{n} I_\nu(r, (b_i - c_2)/c_1). \end{aligned} \tag{2.22}$$

This final result for the scattering emissivity is computationally favorable. We avoid having to loop through the large multi-dimensional arrays, thus saving time.

This transformation has certain limiting cases, such as when the $\mu' = \pm 1$. In that case, we can look at the problem two ways. First we have that

$$\begin{aligned} \lim_{\mu' \to 1} (b_i - c_2)/c_1 &= 1 - \frac{1}{x'} + \frac{1}{x} \quad \text{and} \\ \lim_{\mu' \to -1} (b_i - c_2)/c_1 &= -\left(1 - \frac{1}{x'} + \frac{1}{x}\right) \end{aligned} \tag{2.23}$$

Thus, in these cases I_ν is a constant, and the sum in Equation 2.22 equals $\pi I_\nu(r, \mu = \pm(1 - 1/x' + 1/x))$ – note there was a factor of 2 from the ϕ integration. The second way

to understand these cases goes back to Equations 2.9 and 2.12. If we look at how the delta function transforms, we have

$$\delta\left[\xi - \left(1 - \frac{1}{x'} + \frac{1}{x}\right)\right] \rightarrow \delta\left[\pm\mu - \left(1 - \frac{1}{x'} + \frac{1}{x}\right)\right] \tag{2.24}$$

In these cases, the ϕ integral is 2π, and the μ integral picks out $\pi I_\nu(r, \mu = \pm(1 - 1/\gamma' + 1/\gamma))$. Both methods produce the same result. Our work assumes that there is no contribution from the current frequency to the scattering emissivity (i.e. all photons are down-scattered). This assumption removes coupling between $I_\nu(r, \mu)$ and $\eta^s_\nu(r, \mu)$ at the current frequency ν, so $I_\nu(r, \mu)$ can be solved exactly at each frequency when formally integrating Equation 2.4.

2.2.4 Energy Deposition

Once we have solved $I_\nu(r, \mu)$ for all depths, we then calculate the energy deposited from scattering at each depth using the following relationship:

$$E_{\rm dep}(r) = E_{\rm lept}(r) + \int_0^\infty d\nu \oint d\Omega \left[\chi^{\rm tot}_\nu(r) I_\nu(r, \mu) - \eta^s_\nu(r, \mu)\right], \tag{2.25}$$

where $E_{\rm lept}$ is the (assumed) local kinetic energy deposition from decay leptons (positrons and electrons). In Equation 2.25, the physics we are capturing is the difference between the macroscopic energy lost from the specific intensity and the energy redistributed after scattering. In practice we would only integrate over the range of our frequency grid, which is chosen to cover the physics of the problem.

2.2.5 Implementation

As previously mentioned, this code is being implemented as part of CMFGEN. The code solves Equation 2.4 along characteristic rays for a given impact parameter (p_i) intersecting our radial grid (r_i). In this set-up we have N_D radial grid points and N_C core grid points, making $N_P = N_C + N_D$ impact parameters.

Since this code treats γ-rays from radioactive decays, we begin by reading in nuclear decay data such as nuclear decay energies and their decay probabilities for each unstable isotope included in an ejecta model. Lines with decay probabilities <1 percent are not included

in this code. However, like Hillier & Dessart (2012), we scale the decay line probabilities and decay lepton kinetic energies to conserve the total energy released during decay. Table 1 lists the following nuclear decay data: half-life, energy per decay, kinetic energies of leptons produced, and line energies and probabilities for the ^{56}Ni$\rightarrow^{56}$Co$\rightarrow^{56}$Fe decay chain, which dominates the decay energy for SNe. The annihilation line has a probability of 38 percent because we assume that each positron produced (with 19 percent intensity) annihilates without forming ortho-positronium after thermalization. We read in all other supernova data such as the mass fractions of all included species and count either the number of decays since the last time-step (an average) or the instantaneous decay.

After reading in all decay line data, we set up a frequency grid that is equally spaced in a log frequency scale for a given regime such as between lines, across the line, and two regimes for the red Compton tail. Each regime's spacing is controlled by input parameters to give a desired spectral resolution. A finer frequency grid will produce "narrower" spectral line profiles by reducing numerical diffusion in frequency space as we propagate the photons spatially while solving Equation 2.4. For a factor of roughly 3 less frequency points, the Gaussian profiles become broader by ∼50 percent with no more than a few percent difference in the energy deposition.

Solving Equation 2.4 for a given frequency, k, introduces difficulty given that the scattering emissivity is an integral over angles at a given depth – see Equations 2.9 and 2.11. No coupling between $\eta^{\rm s}_k$ and I_k alleviates some computational difficulty. Full calculation of $\eta^{\rm s}_{\nu'}(r,\mu')$ requires integration over all angles for a given depth point, but integration of Equation 2.4 along rays restricts us to a subset of angles for a given ray – see section 2.2.1. It is necessary to map our intensity and emissivity arrays from $(z,p) \rightarrow (r,\mu)$ in order to perform all scattering calculations. With our assumption that all scattered photons are downgraded in frequency, we solve Equation 2.4 exactly from blue to red frequencies. To do this, we calculate the scattering emissivity for all downgraded frequencies from I_k and use central differencing quadrature ($[\nu_{k-1} - \nu_{k+1}]/2$) to update $\eta^{\rm s}_j$, where $\nu_j < \nu_k$ – an implicit frequency integration of Equation 2.22.

We interpolate I_k (using monotonic cubic interpolation) onto a finer equally spaced linear μ grid in order to use Gauss-Chebyshev abscissa ($b_i = \cos\left[(2i-1)\pi/2n\right]$). An equally

^{56}Ni $\rightarrow$ ^{56}Co $\rightarrow$ ^{56}Fe			
^{56}Ni $\rightarrow$ ^{56}Co		^{56}Co $\rightarrow$ ^{56}Fe	
$t_{1/2}$ = 6.075 days		$t_{1/2}$ = 77.233 days	
Q_γ = 1.718 MeV		Q_γ = 3.633 MeV	
$Q_{\rm th}$ = 0.000 MeV		$Q_{\rm th}$ = 0.116 MeV	
E_γ (MeV)	Prob.	E_γ (MeV)	Prob.
0.158	98.8	0.511	38.0
0.270	36.5	0.847	100
0.480	36.5	0.977	1.4
0.750	49.5	1.038	14.0
0.812	86.0	1.175	2.3
1.562	14.0	1.238	67.6
		1.360	4.3
		1.771	15.7
		2.015	3.1
		2.035	7.9
		2.598	17.3
		3.010	1.0
		3.202	3.2
		3.253	7.9
		3.273	1.9

Table 1 Example nuclear decay data for the ^{56}Ni$\rightarrow^{56}$Co$\rightarrow^{56}$Fe decay chain. $t_{1/2}$, Q_γ, $Q_{\rm th}$ are the half-life, energy per decay, and thermal energy of the leptons produced. We list the decay line energies E_γ and probabilities for lines with probabilities $\geq$ 1 percent. This data and all other nuclear decay data is taken from http://www.nndc.bnl.gov/chart/.

spaced linear grid allows us to quickly find and select the angle abscissa. After we update $\eta^{\rm s}_{\nu'}$ for all possible down-scattered frequencies from ν_k, we then map our arrays back into (z, p) and solve for I_{k+1} for all p.

In principle, the time required to calculate the scattering emissivity scales as $N_D \times N_\nu^2 \times N_\mu^2$, where N_ν is the number of frequency points and N_μ is the maximum number of angle points equal to $2N_P - 1$. However, we loop over down-scattered frequencies when calculating $\eta^{\rm s}_{\nu'}(r, \mu')$, so calculation time will scale less than $N_D \times N_\nu^2 \times N_\mu^2$. Using Gauss-Chebyshev quadrature replaces one loop of length N_μ for a loop of length $N_{\rm Cheb}$. Interpolation onto a monotonic μ grid circumvents looping to find the abscissa in our arrays and makes its calculation time tractable.

Once we have calculated $I_\nu(z, p)$ for all frequencies and impact rays, we map it back into the (r, μ) space and from Equation 2.25 calculate the energy deposited from γ-rays. This decay energy deposition will then be used and read in by CMFGEN as a non-thermal heating source when solving the rate equations coupled to the relativistic radiative transfer equation for lower energy frequencies. We calculate an observer's frame flux according to Hillier & Dessart (2012), which can be compared to observed γ-ray spectra of SNe.

2.3 RESULTS

For this work, we recomputed model CHAN, a Chandrasekhar mass ($M_{\rm Ch}$) WD with 0.62 $M_\odot$ of ^{56}Ni initially, from Wilk et al. (2018) at two epochs, 17.4 days after explosion (roughly bolometric maximum) and 207 days after explosion (nebular time – optically thin to γ-rays). The initial ^{56}Ni mass fraction at 0.75 d is shown in Figure 8 for model CHAN. We performed the calculations described in this work and compared the results to two other methods CMFGEN can use to calculate the energy deposition: (1) MC transport for γ-rays (Hillier & Dessart, 2012) using 8 000 000 decays and (2) a grey absorption approximation (Swartz et al., 1995) using $\kappa_\gamma = 0.06 Y_e$ cm^2 g^{-1}.

2.3.1 Runtime

Our code's runtime depends on the number of frequency points as explained in section 2.2.5. We have made this code parallelizable and have tested it running with 8 CPUs. All calculations were performed with $N_D = 109$, $N_C = 15$, $N_P = 124$. For a low spectral resolution (∼5 500 frequency grid points) calculation, our code's runtime is approximately 40 minutes. However, a much higher frequency grid resolution (∼26 600 frequency grid points) calculation has a runtime of ∼16.9 hours (roughly equal to the number of frequency points squared). Despite a factor of almost 5 less in frequency points, our low resolution calculations differ by at most 5 percent throughout the ejecta for the calculated energy deposition.

The runtime on the same machine for a MC calculation with 8 000 000 decays per species (necessary for low statistical noise) is significantly longer than our low spectral resolution calculation. In this case, the MC runtime is roughly 5 hours. Using a factor of 10 less decays per species, the MC calculation runtime is roughly 1 hour. For lower resolution calculations, the runtimes of both codes are somewhat comparable.

2.3.2 Energy Deposition

Figure 9 compares the ratio of the energy deposition at 17.4 days calculated using our new radiative transfer code to that computed with the MC code, and to that obtained using the grey absorption approximation, as a function of velocity for a M_{Ch} WD. Figure 9 shows that our work is in agreement with the MC method within 3 percent at <20 000 km s^{-1}. Below 3000 km s^{-1}, the MC method is subject to statistical noise and has discrepancies with this work due to a "^{56}Ni hole" where little radioactive material is mixed in. Beyond 20 000 km s^{-1}, MC statistical noise is the source of the discrepancy between the two codes.

Table 2 lists the total integrated energy deposition over the whole ejecta at this epoch and shows that the two methods agree within ∼2.5 percent. Figure 9 also shows the ratio of the non-thermal energy deposited to that of local energy released from nuclear decays. We see that beyond 12 000 km s^{-1}, the energy deposition comes from the inner ejecta as the γ-ray photons scatter. In the region between 12 000–20 000 km s^{-1} where many optical and diagnostic lines are formed, this work is consistent within 2.5–3 percent to that

of Hillier & Dessart (2012). In the same region, the energy deposition computed using the grey approximation diverges from the other methods.

Figure 10 is the same as Figure 9, except now at 207 days and without the ratio of the energy deposition to the local energy emitted being plotted. Despite the fundamental differences in the approach each code uses to calculate the energy deposition, the MC code and our work agree to within 1 percent (highlighted in Table 2). At late times and for ejecta velocities less than 10 000 $\mathrm{km\,s^{-1}}$, the grey approximation is inconsistent with the two other methods by more than ∼5 percent. At this epoch, important strong cooling lines form at velocities ≤10 000 $\mathrm{km\,s^{-1}}$, so wrongly estimating the energy deposited may affect the ionization structure and/or flux in strong cooling lines.

2.3.3 Synthetic Spectra

From the CMF at the outer boundary, we can transform the specific intensity into the observer's frame to produce a synthetic γ-ray spectrum – see section 11 of Hillier & Dessart (2012). Figure 11 shows our resulting synthetic spectra calculated at two epochs, 17.4 and 207 days post-explosion. At 17.4 days, the dominant decay luminosity begins to switch from ^{56}Ni to ^{56}Co, and the spectrum shows strong lines from both ^{56}Ni and ^{56}Co – see Table 1. However, at 207 days, all the ^{56}Ni has decayed and the synthetic spectra is dominated by ^{56}Co decay lines. At both epochs, synthetic spectra from our work and the MC method are in good agreement. The total integrated flux listed in Table 2 shows that the two methods are within ∼9 percent at 17.4 days and ∼4 percent at 207 days.

Both the MC method and our radiative transfer code produce synthetic spectra with predicted asymmetric profiles with absorption on the red side of the emission line. These asymmetric profiles are not uncommon. They are predicted and seen in X-ray line profiles for massive stars (Macfarlane et al., 1991; Owocki & Cohen, 2001; Cohen et al., 2010, 2014). They are also a product of dust scattering (Romanik & Leung, 1981), and have been modelled for dust in the ejecta of SN1987A (Bevan & Barlow, 2016). Electron scattering opacity also produces blue shifted asymmetric profiles for some optical lines in Type II SNe (Dessart & Hillier, 2005b). Many previous theoretical studies have predicted the anticipated asymmetric

γ-ray line profiles, notably Burrows & The (1990); Mueller et al. (1991); Hoeflich et al. (1992, 1993, 1994); Maeda (2006). Since Compton scattering is a continuum opacity, the optical depth of the red side of the line is higher because the path length is larger to the far side of the ejecta. We expect our profiles to exhibit the same effect. In Figure 12 we highlight two ^{56}Co decay lines at 1038 and 1238 keV. Figure 12 shows that at 17.4 days our profiles are asymmetric as the optical depth to γ-rays is large, causing most of the emission to be in the blue side of the line profile; whereas, at 207 days its optical depth is low, and the profile is symmetric.

As can be seen from Figures 11 and 12, the profiles produced by the MC calculation are somewhat narrower than those produced by our γ-ray transfer approach. This arises from numerical diffusion as we propagate photons from the inner regions to the outer boundary of the model (as the calculation is done in the CMF, the photons are propagated in both frequency and space). Numerical diffusion can be reduced by increasing the grid resolution, or by reducing the extent of the outer boundary (especially relevant at 207 days). The best approach would be to utilize the computed scattering emissivities in an observer's frame calculation, but given the lack of high quality observed data we have not implemented such a procedure.

2.3.4 Comparison to SN2014J

To compare our work to the observations from SN 2014J, we computed γ-ray synthetic spectra using our ejecta model at 75 days. Figure 13 shows the 847 and 1238 keV line profiles as a function of velocity, comparing synthetic spectra computed from this work and the MC code at 75 days. The 847 keV line centroid velocities are -1836 and -2158 km s^{-1} for this work and the MC method respectively. Similarly, the 1238 keV line centroid velocities are -960 and -1348 km s^{-1}. These 847 keV line results are consistent with the values measured for the γ-ray spectrum obtained for SN2014J. Churazov et al. (2014, in fig. 4 and table 1) shows that the 847 keV cobalt line is slightly blueshifted with a velocity of -1900 ± 1600 km s^{-1}. However, our work disagrees with the 1238 keV cobalt line. Table 1 of Churazov et al. (2014) shows this line to have a peak velocity shift of -4300 ± 1600 km s^{-1}.

This line should have a smaller blueshifted velocity relative to the 847 keV line since the optical depth is lower due to the smaller cross section at 1238 keV. Given the very large errors on the mean shifts, the disagreement may simply be statistical. The fiducial model plotted in fig 4 of Churazov et al. (2014) shows a less blueshifted 1238 keV line profile.

Not only do our profiles agree with those measured by Churazov et al. (2014), but our flux levels also agree. Adjusting our flux at 75 d in Figure 13 for a distance of 3.5 Mpc to M82, our flux levels are roughly $\sim 9 \times 10^{-6}$ photons cm^{-2} s^{-1} keV^{-1} for our 847 keV line, consistent with the flux levels shown in figure 1 of Churazov et al. (2014).

2.3.5 Grey Transfer

Since SN radiative transfer calculations are already time-intensive, it is beneficial to use a simple and fast prescription to calculate the energy deposited by γ-rays in the ejecta. The grey absorption method of Swartz et al. (1995) (hereafter S95) is one such fast procedure to calculate the energy deposition. Comparing the results of both the MC radiative transfer and this work from Figures 9 and 10, we see that the grey approximation of S95 would require a time varying grey opacity factor as well as one that varies spatially. Simply using the mass absorption coefficient, $\kappa_\gamma = 0.06 Y_e$ cm^2 g^{-1}, does not reproduce the energy deposition the other methods produce.

Figure 14 shows the ratio of the calculated energy deposition of this work to that calculated using the grey transfer from S95. However, we show the energy deposition ratio for varying coefficients for κ_γ at 17.4 and 207 days in the grey approximation. At 17.4 days, we see that $\kappa_\gamma = 0.07 Y_e$ cm^2 g^{-1} matches to our work below 10 000 km s^{-1}, while $\kappa_\gamma = 0.09 Y_e$ cm^2 g^{-1} more accurately reproduces the energy deposition beyond 10 000 km s^{-1}. For low values of the grey absorption (i.e. $0.05 Y_e$ cm^2 g^{-1}) too little energy is deposited in the inner ejecta, which is instead deposited in the outer region. However, increasing the constant in the grey absorption coefficient still produces too much absorption in the outer ejecta.

At nebular times, we see that a lower value of $\kappa_\gamma = 0.05 Y_e$ cm^2 g^{-1} reproduces the energy deposition of the other methods when the ejecta is optically thin to γ-rays. However, Figure 14 shows too much energy being deposited into the outer ejecta beyond 12 000 km s^{-1}

at nebular times. More sophisticated approaches like that of Jeffery (1998) may be needed to model different parts of the ejecta as a function of time.

These values of κ_γ required to reproduce the energy deposition are roughly aligned with those of Maeda (2006). Maeda (2006) argue that $\kappa_\gamma = 0.027$ cm^2 g^{-1} best reproduces a light curve of their spherically symmetric F model. With $Y_e \approx 0.5$, the result of Maeda (2006) is consistent with the value $\kappa_\gamma = 0.05 Y_e$ cm^2 g^{-1} that we claim agrees with our nebular energy deposition. However, our work demonstrates that values of κ_γ much higher are required to reproduce the energy deposition at early times (see Figure 14). Woosley et al. (1986) claim a higher value (because of the centrally located distribution of ^{56}Ni and sensitivity to angle averaging effects along density gradients) of $\kappa_\gamma = 0.07$ cm^2 g^{-1} reproduces the energy deposition function.

2.4 CONCLUSION

We have presented a new code that solves the relativistic radiative transfer equation for γ-rays, taking into account opacity, prompt radioactive decay emissivity, and scattering emissivity. In computing the scattering emissivity, we assume that all photons are downgraded in energy and ignore any thermal redistribution effects since the expansion velocities dominate the transfer. From the specific intensity, we are able to produce an observer's frame spectrum as well as the energy deposition consistent with that of the MC code of Hillier & Dessart (2012).

For a low spectral resolution ($\sim$5 500 frequency grid points) calculation, our new code has the advantage of running in approximately 40 minutes using parallel processing with 8 CPUs. Low resolution calculations result in at most 5 percent differences in calculated energy deposition within the ejecta compared to the higher spectral resolution. In comparison to the MC code, with 8 000 000 decays per species needed to achieve low statistical noise, the code runs in approximately 5 hours on the same machine. In terms of the integrated energy deposition, the two codes agree within 3 percent at early times and within 1 percent at late times.

We have shown that this code produces the expected line profiles. When the optical depth to γ-rays is large, the red side of the line has a higher optical depth than the blue side, and thus most of the emission comes out in the blue side of the line profile – see Figures 11, 12, 13, and Churazov et al. (2014, fig. 4 and table 1).

This code will be publicly available and serves (along with all other MC γ-ray radiative transfer codes) to improve the astrophysics community's constraints on nucleosynthetic yields as well as the stratification of nuclear material in SN ejecta. We are currently limited by observations of γ-rays from SNe, so future observations of γ-rays will uncover a previously untapped opportunity to understand more about the nature of SNe and their progenitors.

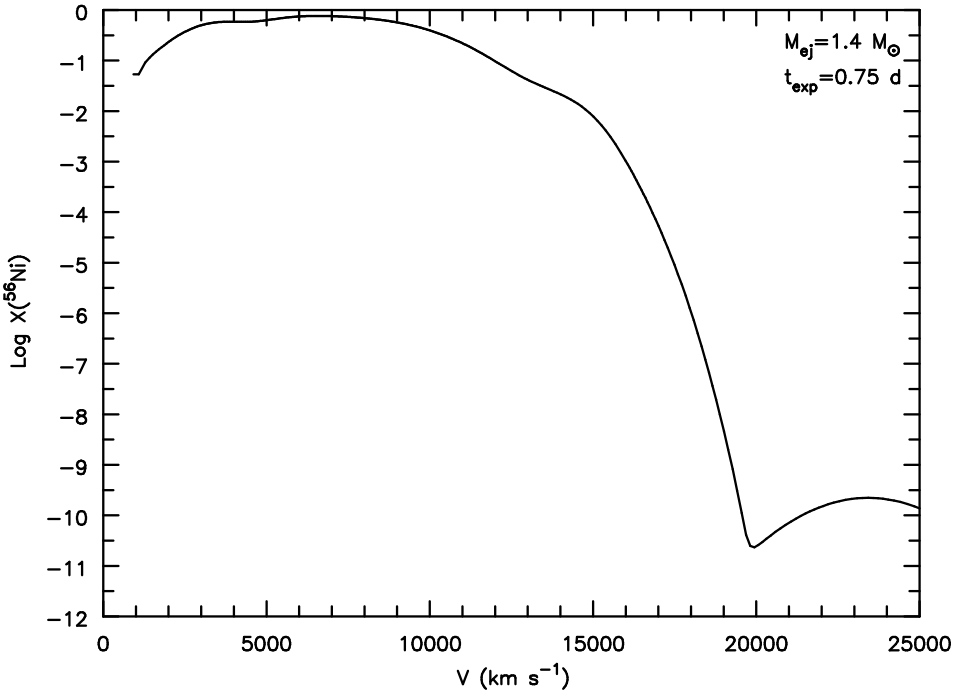

Figure 8 ^{56}Ni mass fraction at 0.75 days after the explosion for the M_{Ch} ejecta (CHAN) model of Wilk et al. (2018).

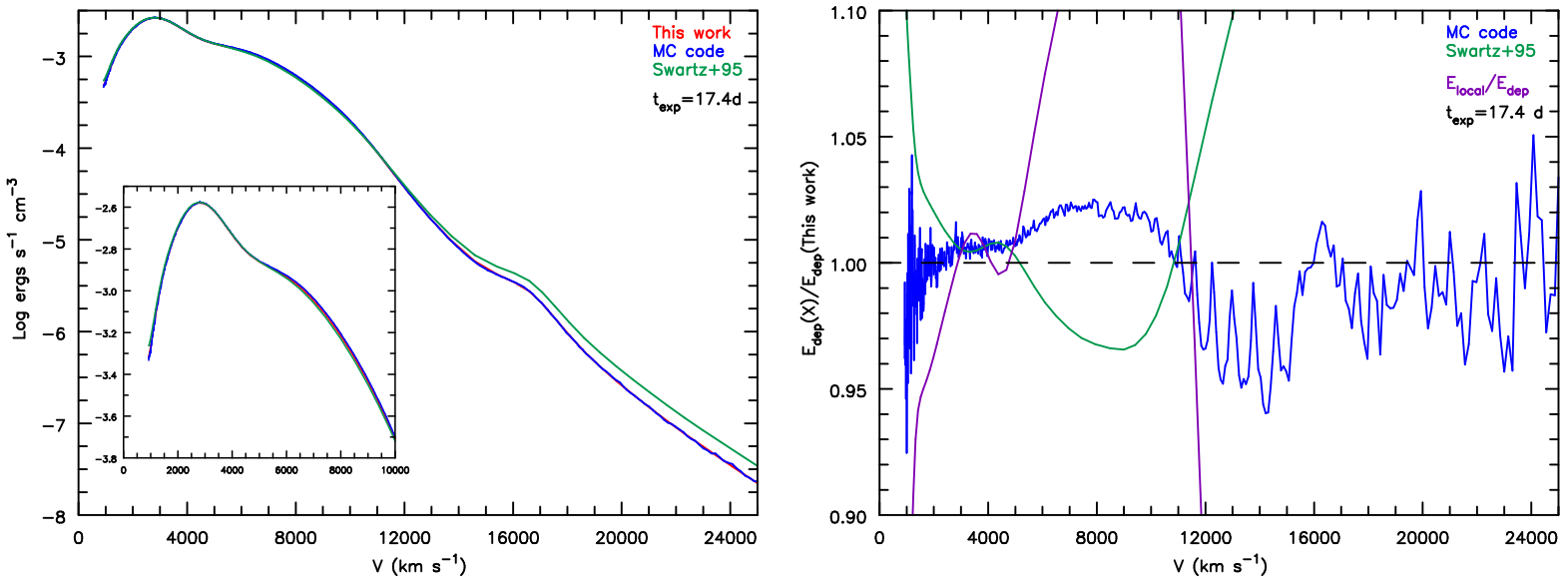

Figure 9 Comparison between this work, the MC method by Hillier & Dessart (2012), and Swartz et al. (1995) of the energy deposited by both leptons and γ-rays from nuclear decays at 17.4 days post-explosion in a Chandrasekhar mass WD with 0.62 $M_\odot$ of initial ^{56}Ni. The MC method and the method described in this work agree within 3 percent despite fundamental differences in their approach. Discrepancies in the inner region result from MC statistical effects from little mass in the inner region. Shown in purple in the right plot is the ratio of the local energy emitted to the energy deposited.

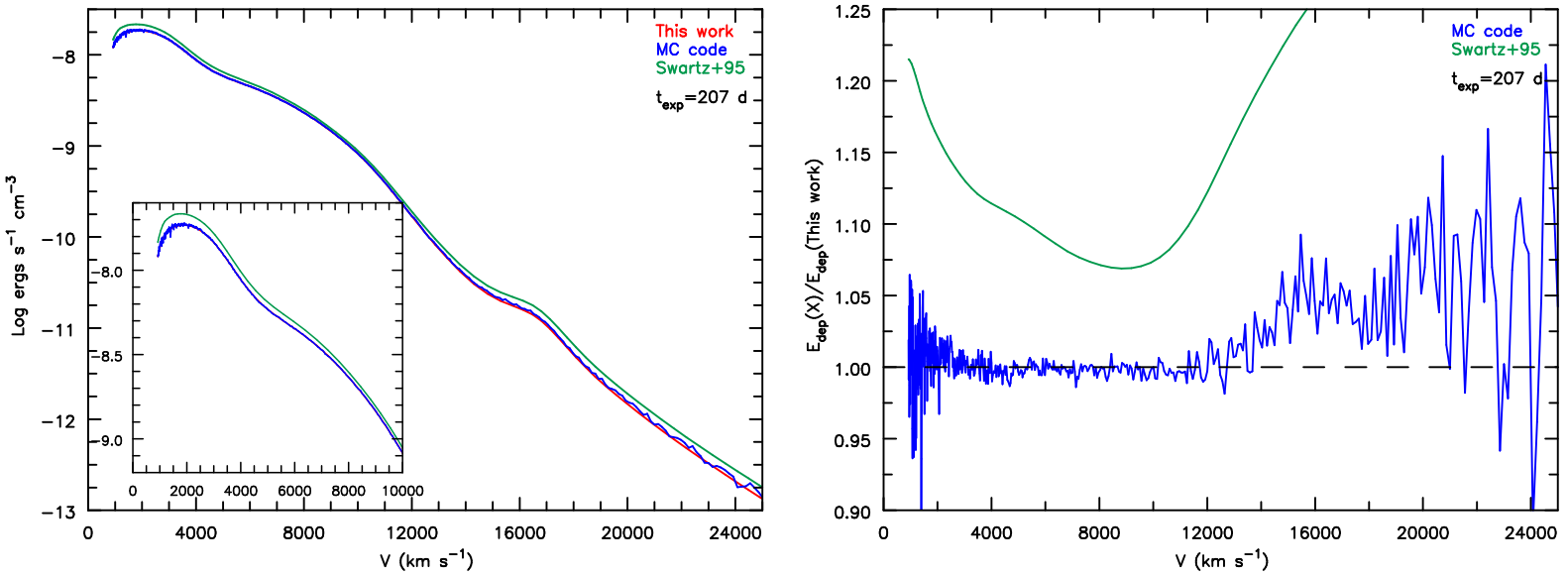

Figure 10 Comparison between this work, the MC method by Hillier & Dessart (2012), and Swartz et al. (1995) of the energy deposited by both leptons and γ-rays from nuclear decays at 207 days post-explosion in a Chandrasekhar mass WD with 0.62 $M_\odot$ of initial ^{56}Ni. The MC method and the method described in this work agree within $\sim$1 percent despite fundamental differences in their approach. Discrepancies in the inner region result from MC statistical effects from little mass in the inner region.

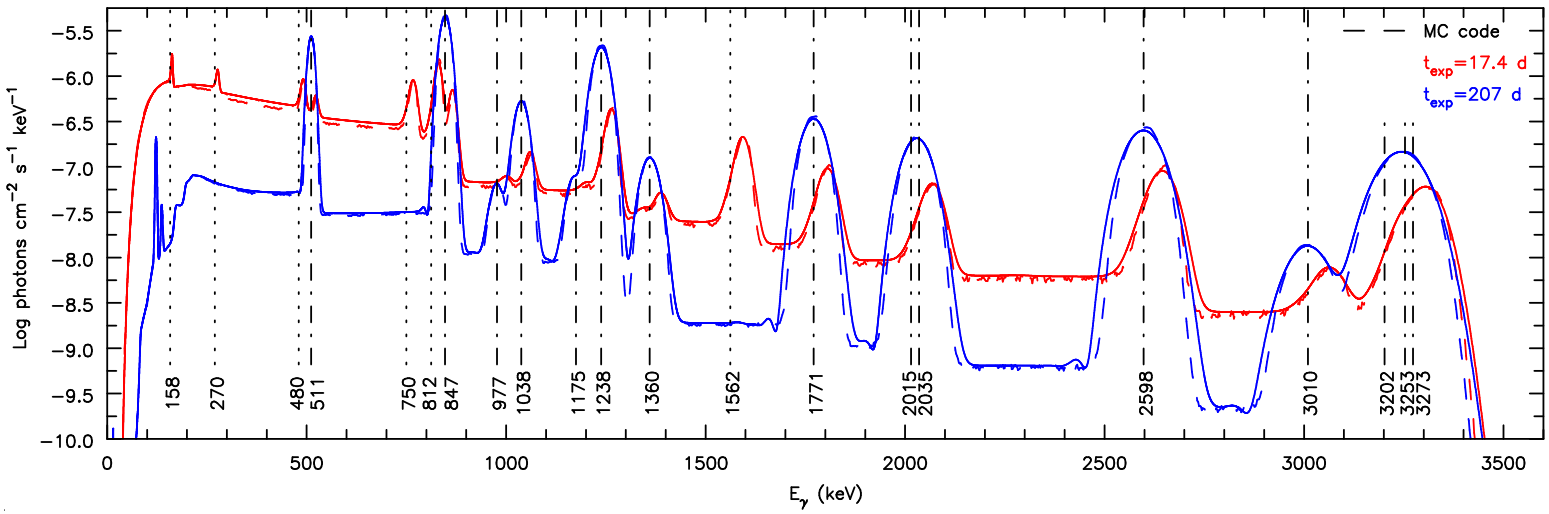

Figure 11 Synthetic γ-ray spectra at two different epochs–17.4 and 207 days post-explosion in a Chandrasekhar mass WD with 0.62 $M_\odot$ of initial ^{56}Ni. Flux counts are relative to a distance of 3.5 Mpc in comparison to SN 2014J in M82 (Karachentsev & Kashibadze, 2006). Dotted lines correspond to the flux calculated by the MC code from the appendix of Hillier & Dessart (2012).

	$t_{\rm exp}$ = 17.4 days			$t_{\rm exp}$ = 207.0 days		
	$E_{\rm dep}$ (ergs s^{-1})	$L_{\rm escape}$ (ergs s^{-1})	$L_{\rm flux}$ (ergs s^{-1})	$E_{\rm dep}$ (ergs s^{-1})	$L_{\rm escape}$ (ergs s^{-1})	$L_{\rm flux}$ (ergs s^{-1})
This work	1.260(43)	9.669(41)	8.466(41)	9.273(40)	1.343(42)	1.359(42)
Hillier & Dessart (2012)	1.279(43)	7.892(41)	7.762(41)	9.291(40)	1.343(42)	1.305(42)

Table 2 Listed is the total energy deposition integrated over the whole ejecta ($E_{\rm dep}$) and the integrated flux from the synthetic spectrum ($L_{\rm flux}$).

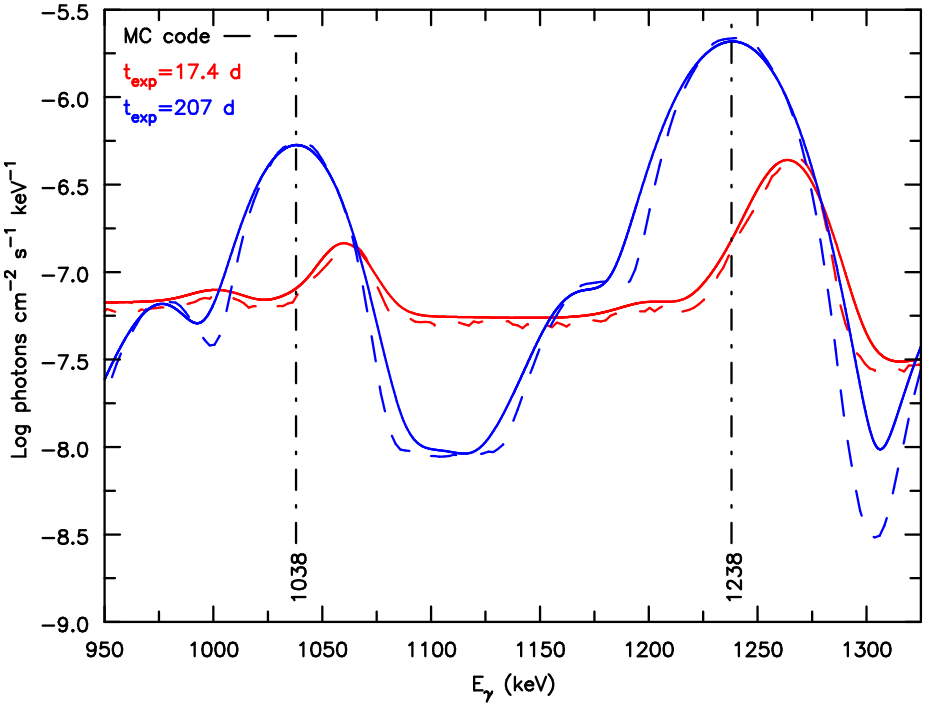

Figure 12 Synthetic flux same as Figure 11, but we have added vertical lines at line center energy ^{56}Co 1038 and 1238 keV. Since the red side of the line has a larger optical depth compared to the blue, we see stronger emission on the blue side of the line profile when the optical depth is high at early times.

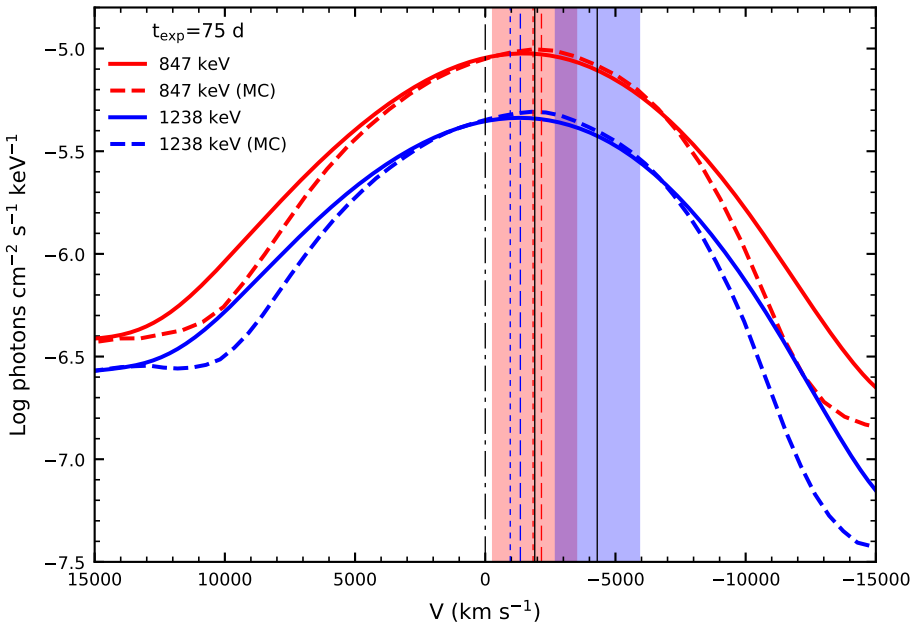

Figure 13 Synthetic flux line velocities for 847 keV and 1238 keV computed from our ejecta model at 75 days post-explosion. The 847 keV line centroid velocities are -1836 and -2158 $\mathrm{km\,s^{-1}}$ for this work and the MC code respectively. Also, the 1238 keV line centroid velocities are -960 and -1348 $\mathrm{km\,s^{-1}}$ respectively. We have added vertical lines at 0 $\mathrm{km\,s^{-1}}$ (dot-dashed), -1836 $\mathrm{km\,s^{-1}}$ (red dotted), -2158 $\mathrm{km\,s^{-1}}$ (red dashed), -960 $\mathrm{km\,s^{-1}}$ (blue dotted), -1348 $\mathrm{km\,s^{-1}}$ (blue dashed), -1900 $\mathrm{km\,s^{-1}}$ (solid black), and -4300 $\mathrm{km\,s^{-1}}$ (solid black). The red shaded region represents the 1σ 1600 $\mathrm{km\,s^{-1}}$ uncertainty from -1900 $\mathrm{km\,s^{-1}}$. The blue shaded region represents the 1σ 1600 $\mathrm{km\,s^{-1}}$ uncertainty from -4300 $\mathrm{km\,s^{-1}}$.

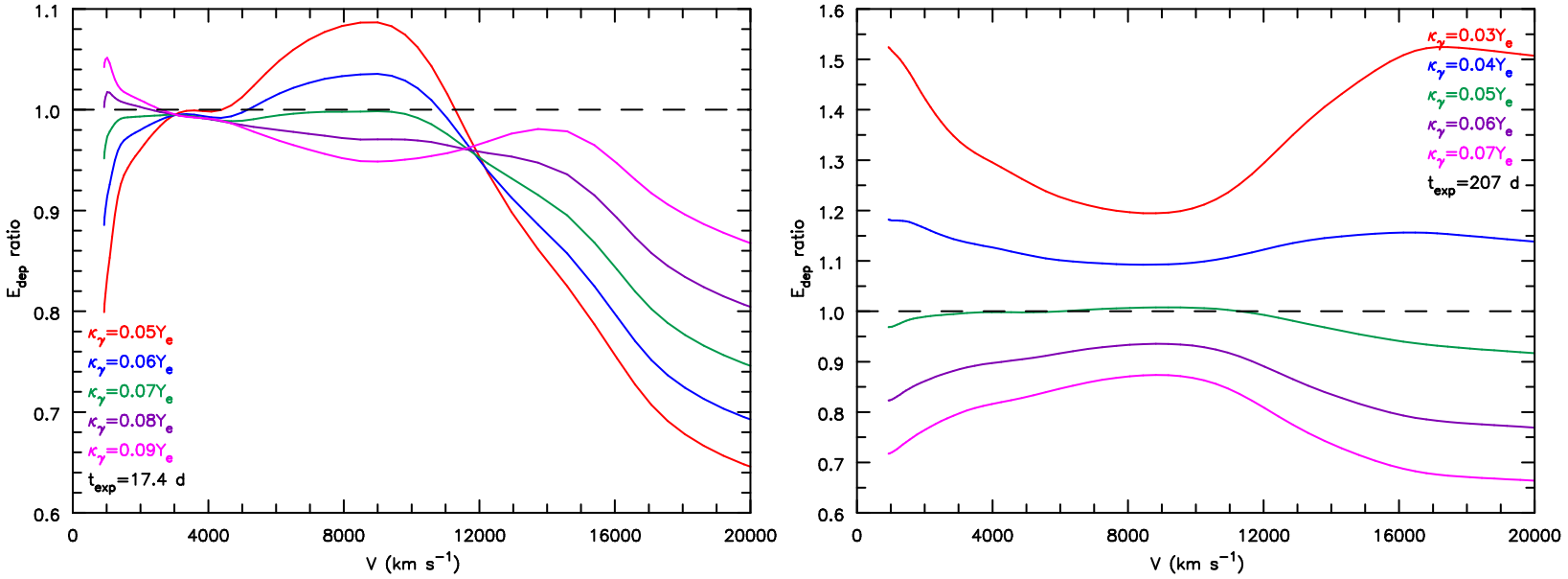

Figure 14 Energy deposition ratio comparison of grey radiative transfer calculations of Swartz et al. (1995) using $\kappa_\gamma = \alpha Y_e$ cm^2 g^{-1} (α = 0.03, 0.04, 0.05, 0.06, 0.07, 0.08, 0.09). This ratio corresponds to $E_{\rm dep}$(this work)/$E_{\rm dep}$(grey).

3 EJECTA MASS DIAGNOSTICS OF TYPE IA SUPERNOVAE

3.1 INTRODUCTION

Type Ia supernovae (SNe Ia) are thought to be thermonuclear runaway explosions of carbon-oxygen (C/O) white dwarfs (WDs) (Hoyle & Fowler, 1960), but the formation channel of the progenitor remains uncertain. Determining the progenitor channel(s) of SNe Ia, and their diversity, is of crucial importance since it will improve their use as probes of cosmological parameters (Riess et al., 1998; Perlmutter et al., 1999). Further, understanding the progenitor channel allows us to probe stellar evolution of binary systems prior to the SN occurring, and hence place constraints on both binary synthesis models and binary evolution.

There are two main progenitor channels invoked to explain the origin of SNe Ia – the single degenerate (SD) channel and double degenerate channel. In the "classic" SD channel, the WD accretes matter (usually hydrogen and/or helium) from a non-degenerate star due to binary interaction via Roche lobe overflow. However, mass transfer in the SD channel is not limited to Roche lobe overflow – it can also be mediated by wind mass loss as, for example, in symbiotic systems (see Maoz et al., 2014, for a review). In the SD channel matter accumulates on the white dwarf, where stable burning can occur, until the star approaches the Chandrasekhar mass ($M_{Ch} \approx 1.4\ M_{\odot}$) and explodes leading to a SN Ia (Whelan & Iben, 1973; Nomoto, 1982).

How the WD explodes has long been a matter of study within the astrophysics community. The different explosion mechanisms include pure detonation (Arnett, 1969; Sim et al., 2010), pure deflagration (Nomoto et al., 1976), delayed detonation and pulsating delayed detonation (Khokhlov, 1991a,b; Gamezo et al., 2005; Livne et al., 2005; Röpke & Niemeyer, 2007; Jackson et al., 2010; Seitenzahl et al., 2013), and gravitationally-confined

detonation (GCD) (Plewa et al., 2004). More recent research on the GCD, including 3D full star simulations, was presented by Seitenzahl et al. (2016). For sub-M_{Ch} WD masses, a double detonation scenario has been explored (Woosley & Weaver, 1994; Livne & Arnett, 1995; Fink et al., 2007, 2010).

One of the most successful theories at reproducing the properties of standard SNe Ia is the delayed-detonation transition (DDT) model where the WD first undergoes a subsonic deflagration phase. The resulting expansion of the WD creates lower density fuel, which is necessary for the production of intermediate mass elements (IMEs). At a particular density, the burning switches from subsonic to supersonic (Khokhlov, 1991a,b). This scenario is required to recreate the observed chemical stratification. Pure detonation models produce too many iron group elements (IGEs) such as iron and nickel but not enough IMEs at high velocities to reproduce SN Ia spectra. On the other hand, deflagration models produce abundant amounts of IMEs but not enough ^{56}Ni to power the SN luminosity. This mechanism is a possible channel for under-luminous SNe Ia (Travaglio et al., 2004; Phillips et al., 2007; Jordan et al., 2012; Kromer et al., 2013). One dimensional (1D) DDT models have been very successful in reproducing the observed properties of SNe Ia. However, these models describe the turbulent flame propagation only in a parametrized way. Three dimensional (3D) models better capture the fluid instabilities and mixing. This lead to different ejecta structures that do not reproduce observables as well as 1D models (see e.g. Seitenzahl et al., 2013; Sim et al., 2013b).

The double degenerate scenario corresponds to the merger of two WDs through loss of angular momentum by gravitational wave emission. It is not understood how the merger triggers the explosion, although it is thought that during the merger the smaller mass WD donates matter to the more massive WD. Recently, modeling by Sato et al. (2015) has shown that, depending on the masses of the two WDs, explosions can occur either during the merger phase, provided both WDs are within a mass range between 0.9–1.1 $M_{\odot}$, or within the merger remnant phase when the more massive object reaches M_{Ch}. From their models, the authors estimate that 9 percent of galactic SNe Ia can be attributed to mergers. One problem in this scenario is that rapid mass accretion of carbon and oxygen leads to an off-center carbon ignition and subsequently an O/Ne/Mg WD (Saio & Nomoto, 1985). Accretion induced

collapse creates additional problems for high accretion rates, leading to the formation of a neutron star instead of a SN Ia. For an extensive review about progenitors of SNe Ia, see Maoz et al. (2014).

When almost the entire C/O WD has burnt, releasing $\sim 10^{51}$ ergs (more energy than the gravitational binding energy of a M_{Ch} WD), the energy liberated unbinds the WD, producing an ejecta with no remnant. Ejecta velocities of the order of $\sim 10\,000\,\mathrm{km\,s^{-1}}$ are produced, and within minutes, the ejecta reaches a homologous coasting phase (radiation pressure from ^{56}Ni decay produces second order effects). At early times the ejecta is radiation dominated and heated by the decay of ^{56}Ni (^{56}Co for post-maximum evolution). It is because of this main decay chain of $^{56}\mathrm{Ni}\rightarrow{}^{56}\mathrm{Co}\rightarrow{}^{56}\mathrm{Fe}$, with roughly 1.7 MeV of energy release per decay for ^{56}Ni and 3.7 MeV per decay for ^{56}Co, that these objects are so luminous. However, Dessart et al. (2014b) show the importance of heating the outer ($\geq 20\,000$ $\mathrm{km\,s^{-1}}$) ejecta from other decay channels.

Early work by Stritzinger et al. (2006) suggested sub-M_{Ch} WDs as progenitors for some SNe Ia based on comparisons of $UVOIR$ light curves of 16 SNe with analytical models of nuclear decay luminosities and energy deposition. Scalzo et al. (2014a,b), Sim et al. (2010, 2013a), and Blondin et al. (2017) have shown that there is both observational and theoretical evidence for sub-M_{Ch} explosions. From photometric model fitting, Scalzo et al. (2014a,b) shows that the mass distribution for SNe Ia includes both sub-M_{Ch} and super-M_{Ch} events. Scalzo et al. (2014b) argue that 25–50 percent of SN Ia events deviate from M_{Ch} events, with most of these occurring as sub-M_{Ch} explosions. Therefore, for given measured ^{56}Ni masses, one can compare SNe Ia to better understand how ejecta mass affects light curves and spectral evolution.

Sim et al. (2010, 2013a) found good agreement with photometric observations at maximum and reproduced IME features in synthetic spectra at maximum with 1D pure detonations of sub-M_{Ch} explosions. However, these models decline too rapidly post maximum. This idealized approach ignores the influence of any accreted helium layer. Previous works (Woosley & Weaver, 1994; Livne & Arnett, 1995; Hoeflich & Khokhlov, 1996; Hoeflich et al., 1996b; Nugent et al., 1997; Kromer et al., 2010) found difficulties reproducing the observed light curves, colors and spectral evolution after treating the burnt helium layer,

which synthesizes a significant amount of ^{56}Ni.

Woosley et al. (2007) explored a grid of SN Ia models coming from 1.38 $M_\odot$ WDs with varying amounts of mixing and ^{56}Ni, finding models of similar ^{56}Ni to have large variations of decline rates ($\Delta M_{15}(B)$ – which is the change in B-band magnitude 15 days after B-band maximum (Phillips, 1993)) and anti width-luminosity relationships. Woosley & Kasen (2011) computed hydrodynamic and radiative transfer simulations of sub-M_{Ch} mass models for helium-accreting WDs, but the authors only found reasonable agreement with spectra and light curves of common SNe Ia for the most massive white dwarfs with the smallest helium layers they considered. Blondin et al. (2017) looks at broadening our understanding of the width-luminosity relation (WLR) using pure detonations of sub-M_{Ch} WDs. Their work shows promising agreement with observations of faint SNe Ia, confirming the need for two WD populations to explain the full behavior of the WLR seen at high and low SN Ia brightnesses.

Observations have shown high-velocity features (HVFs) in early-time spectra of SNe Ia. These features have been used to constrain the explosion scenario (Mazzali et al., 2005a,b; Tanaka et al., 2006; Blondin et al., 2013; Childress et al., 2013, 2014; Silverman et al., 2015; Zhao et al., 2015; Pan et al., 2015). Studying the formation of these features as well as their correlation with galaxy environment can improve our understanding of Type Ia progenitors. We can gain insights, for example, into the density and temperature structure of the outer layers. The latter will reveal itself through changes in ionization and hence the strength of spectral features.

In this chapter we study two sub-M_{Ch} models ($\sim$1 $M_\odot$), a M_{Ch} model ($\sim$1.4 $M_\odot$), and a super-M_{Ch} model ($\sim$1.7 $M_\odot$), all with the same ^{56}Ni mass by design, to determine the effects of ejecta mass. One model is a standard DDT model, two models are standard DDT models whose density has been scaled to give the desired ejecta mass, while the final model arises from a pure detonation in a sub-M_{Ch} model. The original DDT models are also somewhat artificial. For example, the onset of detonation in a DDT model is a free parameter. Further, it is impossible in current models to resolve and adequately model the thermonuclear flame (see Ciaraldi-Schoolmann et al. (2013) and references therein). We consider evolution over more than two hundred days in time – from $\sim$1 day after the

explosion until approximately 220 days after the explosion, and look for diagnostics of ejecta mass ($M_{\rm ej}$) for our ^{56}Ni mass that can be used to distinguish between the different models. Since the precise explosion mechanism is uncertain, the two sub-$M_{\rm Ch}$ models were exploded using different assumptions. Spectra and light curves were computed using non-LTE and time-dependent radiative transfer. Looking for SN Ia diagnostics, we wanted to remove sensitivity of ^{56}Ni while focusing on ejecta mass to uncover insights in SN Ia evolution, both spectroscopically and photometrically.

The chapter is organized as follows. In section 3.2, we discuss the techniques used and initial ejecta properties. We compare the bolometric light curves as well as synthetic photometric light curves in section 3.3. We discuss the spectral evolution, highlighting the strong spectral differences, in section 3.4. In section 3.5, we further highlight the distinctions between our two sub-$M_{\rm Ch}$ models. In section 3.6.1 we comment on the lack of high velocity features. section 3.6.2 shows spectral comparison to a few SNe Ia that are close in measured $M_{\rm ej}$ and ^{56}Ni mass. In section 3.6.3 we discuss shortcomings of our models in reproducing spectral characteristics of SNe Ia beyond 20 days post-maximum. section 3.7 summarizes our results and conclusions.

3.2 TECHNIQUE

To determine spectral and light curve diagnostics we utilize hydrodynamical models that have been evolved from explosion until 0.75 days. Homologous expansion of the ejecta is well established at 100 seconds, and it is assumed to strictly hold at all times thereafter. We allow for non-local thermodynamic equilibrium (non-LTE) and solve the spherically symmetric, time-dependent, relativistic radiative transfer equation in order to produce emergent synthetic spectra from which synthetic light curves (LCs) can be produced.

3.2.1 Ejecta and Radiative Transfer Modeling

Our models correspond to scaled ejecta of model DDC0 (density scaled by 0.73, model SUB2) and DDC15 (density scaled by 1.22, model SUP), complemented with models DDC10 (no scaling applied, model CHAN) – see Blondin et al. (2013) – and SCH5p5 (density scaled by 0.98, model SUB1) – see Blondin et al. (2017). This density scaling is applied to produce ejecta with the same ^{56}Ni mass initially (0.62 $M_\odot$), but differing in ejecta mass so that they lie below, at, and above the M_{Ch}. This scaling, applied exclusively to the density at 10 seconds after explosion, is obviously artificial. An advantage of this scaling method is that, while the mass varies, the chemical stratification does not. This ensures the models retain their fundamental characteristic of all SN Ia ejecta. We do not compute the combustion nor make any claim that a flame would behave in the way adopted for the corresponding WD mass (i.e., deflagration followed by detonation in the DDC models; pure detonation in the SCH model). Even in the original (unscaled) model, the treatment of combustion is largely imposed rather than computed from first principles. The purpose of the study is to investigate the signatures sensitive to variations in ejecta mass, keeping the ^{56}Ni mass the same between all models in order to retain only one variable quantity. Model masses, kinetic energies, and important species masses are summarized in Table 3.

The use of scaled DDT models for SUB2 and SUP is problematical since the explosion properties will depend on the mass of the WD. For example, differences in the initial central densities before the explosion will likely lead to different abundance profiles within the ejecta. In particular, sub-M_{Ch} WDs, unlike their M_{Ch} counterpart with stable IGEs in their inner ejecta, do not exhibit a '^{56}Ni hole' which is a low ^{56}Ni abundance inside an expansion velocity of 2500 km s^{-1}. However, a comparison of SUB2 with SUB1 will allow us to test the sensitivity of the results to the adopted explosion model. The explosion mechanism for ejecta with super-Chandrasekhar masses is extremely uncertain, and any adopted model will have limitations.

The radiative transfer models have been computed using CMFGEN (Hillier & Miller, 1998; Hillier & Dessart, 2012; Dessart et al., 2014b,c), which solves the spherically symmetric, non-local thermodynamic equilibrium (non-LTE), time-dependent, relativistic radiative

transfer equation in the co-moving frame. To advance in time, we used a 10 percent time step for each model starting from 0.75 days until ∼100 days, after which we used a time step of 10 days. At early times ($\lesssim$7 days) during the time sequence, we assumed that γ-ray photons created from radioactive decays are locally deposited. Otherwise, we approximate the γ-ray deposition as grey, adopting the procedure from Swartz et al. (1995) and a $\kappa_\gamma = 0.06 Y_e$ cm^2 g^{-1}. The kinetic energy of decay positrons is locally deposited at all epochs. CMFGEN currently treats both one- and two-step decay chains for calculating non-thermal heating.

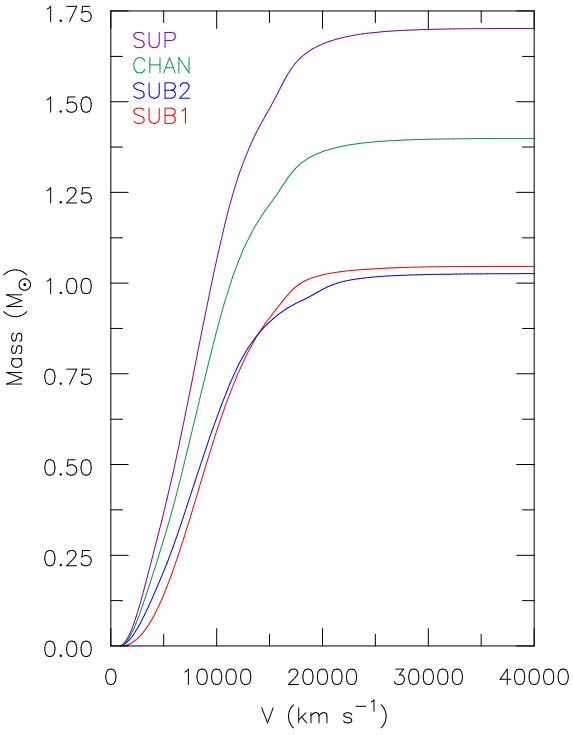

Figure 15 Illustration of the outward cumulative mass as a function of velocity. The cumulative mass begins to flatten off around 25 000 km s^{-1} for all models, the velocity at which the density begins to decrease rapidly. Less than 1 percent of the total mass is exterior to this velocity.

3.2.2 Ejecta Conditions for Radiative Transfer

Table 3 shows the yields for the most abundant species in our ejecta models at 0.75 days. Since the ^{56}Ni mass is fixed, there are substantial variations in the mass of the IMEs. In

Model	Mass ($M_\odot$)	$E_{\rm Kin}$ (10^{51} ergs)	$v_{\rm rms}$ (km s^{-1})	C ($M_\odot$)	O ($M_\odot$)	Na ($M_\odot$)	Mg ($M_\odot$)	Si ($M_\odot$)	S ($M_\odot$)	Ar ($M_\odot$)
SUB1	1.04	1.22	10821	3.295(−3)	5.196(−2)	1.306(−5)	2.441(−3)	1.553(−1)	1.022(−1)	2.248(−2)
SUB2	1.02	1.17	10695	8.803(−4)	3.906(−2)	4.466(-6)	2.615(−3)	1.185(−1)	7.488(−2)	1.654(−2)
CHAN	1.40	1.51	10415	2.419(−3)	9.595(−2)	1.244(−5)	9.557(−3)	2.551(−1)	1.661(−1)	3.693(−2)
SUP	1.70	1.81	10351	3.333(−3)	1.293(−1)	2.044(−5)	1.387(−2)	3.805(−1)	2.443(−1)	5.223(−2)
Model	Ca ($M_\odot$)	Ti ($M_\odot$)	Cr ($M_\odot$)	Fe ($M_\odot$)	Co ($M_\odot$)	^{58}Ni + ^{60}Ni ($M_\odot$)	^{56}Ni ($M_\odot$)			
SUB1	2.361(−2)	2.665(−5)	1.030(−2)	2.226(−2)	5.526(−2)	1.1(−2)	5.684(−1)			
SUB2	1.822(−2)	1.083(−4)	1.516(−2)	6.654(−2)	5.680(−2)	2.6(−2)	5.710(−1)			
CHAN	4.120(−2)	1.486(−4)	2.689(−2)	1.020(−1)	5.713(−2)	2.5(−2)	5.708(−1)			
SUP	5.562(−2)	1.828(−4)	2.977(−2)	1.224(−1)	5.777(−2)	3.0(−2)	5.707(−1)			

Table 3 Model summary. Listed are the masses in $M_\odot$, ejecta kinetic energies in 10^{51} ergs, and the root mean square of the velocity in km s^{-1}. Also listed is model mass information in $M_\odot$ at 0.75 days post explosion. The parentheses (#) correspond to $\times 10^{\#}$.

particular, the mass of individual IMEs in model SUP is a factor of 3 to 5 larger than in model SUB2; model SUB1 has ∼1.3 to 1.4 times the mass of IMEs and ∼1/3 times the iron mass of SUB2. The initial iron abundance in SUB1 is almost a factor of 6 lower than in SUP. The mass of stable nickel (^{58}Ni and ^{60}Ni) is 0.011, 0.026, 0.025, and 0.030 $M_\odot$ for SUB1, SUB2, CHAN, and SUP. The presence of stable nickel features in nebular spectra, and the ability to measure the nickel abundance, is discussed in sections 3.4 and 3.6.3.

In Figure 15 we show the outward cumulative mass as a function of velocity. Less than 1 percent of the mass lies beyond 25 000 km s^{-1} for all models, and hence we restrict future model ejecta comparisons to velocities less than 30 000 km s^{-1}. Higher velocity material makes very minor contributions to synthetic spectra.

Figure 16 compares the initial mass fraction at 0.75 days for all models. All but model SUB1 exhibit an '^{56}Ni hole' at velocities less than ∼2500 km s^{-1}. As noted earlier, the hole in SUB2 is artificial, and arises since the model was scaled from a model based on the explosion of a M_{Ch} WD which has a higher central density.

3.3 LIGHT CURVES

The light curves and color evolution of Type Ia models depends on the progenitor system, and potentially offer a means to distinguish between progenitor systems. Due to differences in ejecta mass, the diffusion time varies between models, giving rise to morphological separations in both the width of each bolometric light curve and the peak luminosity. However, from work by Pinto & Eastman (2000a,b), we expect this effect to be small.

Figure 17 shows the bolometric light curves of all models relative to the time of explosion. Decreasing ejecta mass (shorter diffusion time) corresponds to a faster evolving supernova. In days since explosion, the bolometric luminosity maximum occurs at 14.4 (3.80×10^9 $L_\odot$), 14.4 (3.96×10^9 $L_\odot$), 15.84 (3.63×10^9 $L_\odot$), and 17.42 (3.47×10^9 $L_\odot$) for models SUB1, SUB2, CHAN, and SUP respectively. To characterize the bolometric light curves, we list t_{max} (time of bolometric maximum), $t_{-1/2}$ and $t_{+1/2}$ (the times to rise from half bolometric maximum luminosity to maximum and to decline from bolometric maximum

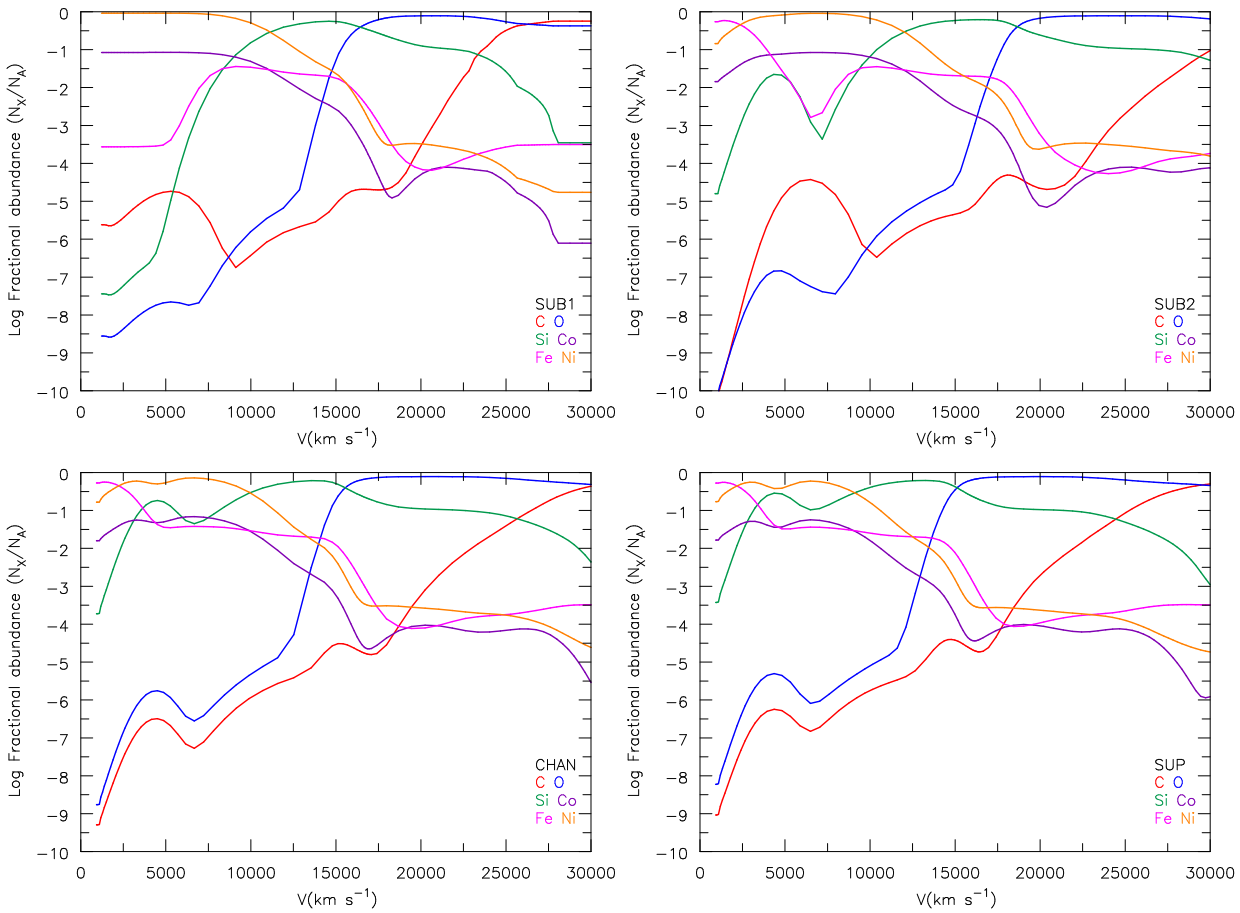

Figure 16 The initial abundance as a function of velocity for carbon, oxygen, silicon, iron, cobalt, and nickel for model SUB1 (top left), SUB2 (top right), CHAN (bottom left), and SUP (bottom right). Notice the absence of the '^{56}Ni hole' in model SUB1 (i.e. presence of ^{56}Ni), a result of having lower densities during the initial explosion. Also apparent is the overlap of the nickel distribution with IMEs around 8000 to 12 000 km s^{-1} in all models.

back to half of maximum – see Contardo et al. (2000)) in Table 4. Between ∼1–1.7 M$_\odot$, we have roughly a 1 day difference in half light rise times ($t_{-1/2}$), with SUB ejecta models rising faster. After bolometric maximum, the SUP ejecta model takes roughly ∼ 3.5 days longer than the SUB ejecta models to decline to half light ($t_{+1/2}$). With precise measurement determinations of the rise time in $L_{\rm bol}$, we can put stronger constraints on the ejecta mass for a given ^{56}Ni mass.

As the ^{56}Ni mass is the same for all models, differences in the bolometric light curve

evolution are primarily due to ejecta mass. However, despite differences in ejecta mass of ∼70 percent, the differences are relatively small, though measurable. This effect of ejecta mass should be clearly visible from a statistical sample of deep high cadence observations of SNe Ia.

Figure 18 shows synthetic light curves plotted in days since B-band maximum. The light curves for the two sub-M_{Ch} ejecta models tend to be more luminous at maximum (with the exception of the NIR bands) but have fainter nebular luminosities. The former arises because at bolometric maximum $L_{bol} \approx L_{decay}$ and since the peak is earlier, the decay rate is greater. The latter arises because of the less efficient trapping of γ-rays. Table 4 also lists the peak LC absolute magnitudes for different Johnson bands ($M_U \rightarrow M_K$), rise times (in days since explosion), and decline parameter $\Delta M_{15}(X)$ for a given band X. All bands show a faster rise time for lower-mass ejecta models, just as they do for L_{bol}.

Observational evidence suggests that H-band photometry for SNe Ia can provide higher accuracy than the B-band calibration galactic distances (Krisciunas et al., 2004, 2007; Wood-Vasey et al., 2008). However, our models have a spread of almost one magnitude in the H-band at the time of B-band maximum light. Following the temperature separation between models (higher mass → cooler ejecta), the higher mass ejecta also show larger flux in the H-band at all epochs. Our light curves still show two peaks in the H-band as normal SNe Ia do, a consequence of the ionization shift in iron (and other IGEs) going from ionization states 2+→1+ (Kasen, 2006). The second peak is of the same brightness for our SUB models compared to higher ejecta mass models. Past the second H-band peak, we see roughly a constant decline in all models until close to 150 days past maximum light.

Figure 19 shows the $U-B$, $B-V$, and $B-R$ color evolution relative to B-band maximum. It shows that the lower mass models are bluer at most epochs. There is over a magnitude difference in $B-R$ from sub-M_{Ch} to super-M_{Ch} around 25 days after B_{max}. SUB models are bluest in color post B-band maximum compared to higher mass models. Post maximum, model SUP remains the most red of all the models, while SUB1 remains bluer than other models after +40 days, a result of higher temperatures and ionization due to larger $M(^{56}\mathrm{Ni})/M_{ej}$. This is explored in Figures 20 and 21 and then in section 3.4 where we discuss the spectral evolution.

Figure 20 shows the temperature evolution of our models, with SUB1 and SUB2 maintaining higher temperatures at all epochs. Figure 21 shows the average ionization for a few IGEs such as iron, cobalt, and nickel. SUB models show a higher ionization compared to higher mass models, producing ejecta with bluer colors. The monotonic temperature distribution of SUB1 below 5000 $\mathrm{km\,s^{-1}}$ is due to the lack of a '^{56}Ni hole'. Figure 22 shows the fraction of the energy deposition from positrons to the total energy deposition at about 216 days post explosion. At late times SUB1 maintains a higher ionization in the innermost ejecta due to more assumed local positron energy deposition. Generally speaking, SUB1 and SUB2 have higher temperatures at comparable epochs than those of CHAN and SUP. We further discuss the implications of higher temperatures in section 3.4.

3.4 SPECTRAL DIAGNOSTICS

Spectra provide important constraints for distinguishing progenitor and explosion models. However, despite a 70 percent difference in mass, model optical spectra (Figures 23, 24, 25, 26, and 27) at most phases are similar, consistent with work by Blondin et al. (2013) who concluded that SNe Ia are mainly distinguished by their ^{56}Ni mass. This similarity is observed for classical SNe Ia where differences in optical spectra are generally rather subtle (Filippenko, 1997), which presumably occurs because of similarities in composition. Interestingly, optical spectra of models SUB1 and SUB2 are remarkably similar for most phases of evolution, despite the different methods to produce these ejecta models. However, there are differences between models, particularly in the infrared, and these do give rise to useful diagnostics. We investigate these diagnostics by comparing model spectra at time steps of approximately −10, −5, 0, +5, +10, +20, +50, +100, and +200 days from bolometric maximum (Figures 23, 24, 25, 26, and 27). Thus, when comparing observational spectra of SNe Ia from comparable ^{56}Ni mass, these diagnostics will separate events by ejecta mass. Note that model spectra are plotted for vacuum wavelengths; however, wavelengths ≥2000 Å listed are quoted in air.

Figure 23 shows the early spectral evolution (−10, −5, and 0 days relative to bolo-

metric maximum) plotted in λF_λ (arbitrary units). We label the contributions of important species at bolometric maximum. Figures 24 and 25 show the post maximum photospheric phase (+5, +10, +20, +50) plotted in λF_λ (arbitrary units). Figures 26 and 27 show nebular spectra at +100 and +200 days post bolometric maximum plotted in F_λ (arbitrary units). Contributions from important species are labeled. Notice the transition towards predominantly forbidden lines in nebular spectra. These figures are used to highlight important diagnostics.

3.4.1 [Ni II] 1.939 Microns

In SNe Ia, the nickel abundance is sensitive to the progenitor mass and/or explosion scenario. In 1D explosion modeling, higher central densities have higher neutronization that leads to more stable ^{58}Ni being produced during nuclear burning (Nomoto, 1984; Khokhlov, 1991a,b). This 1D modeling implies that sub-M_{Ch} SNe Ia will show a lower abundance of ^{58}Ni compared to M_{Ch} SNe Ia (for the same ^{56}Ni mass). However, 3D DDT modeling suggests that the '^{56}Ni' hole predicted in 1D M_{Ch} WD DDT models may be absent, and both ^{56}Ni and ^{58}Ni extend from the lowest velocities to about 10 000 km s^{-1}(Kasen et al., 2009; Seitenzahl et al., 2013). ^{22}Ne settling in sub-M_{Ch} has also been proposed as a way to enhance the neutronization; however, the time-scale for gravitational settling can be $\sim 10^9 - 10^{10}$ yrs (Bildsten & Hall, 2001). Therefore, nickel diagnostics, particularly at nebular times, may constrain the progenitor scenario, nucleosynthesis, and explosion mechanism (Woosley, 1997; Iwamoto et al., 1999; Stehle et al., 2005; Mazzali & Podsiadlowski, 2006; Gerardy et al., 2007; Maeda et al., 2010a; Mazzali et al., 2011; Mazzali & Hachinger, 2012; Mazzali et al., 2015). At nebular times most of the ^{56}Ni will have decayed, and any nickel emission features are due to stable nickel, and in particular ^{58}Ni and ^{60}Ni, which are expected to be underabundant in (1D) sub-M_{Ch} DDT models compared with M_{Ch} models. The width of any observed nebular nickel feature will constrain the hydrodynamic width of the emitting region, thus testing model predictions about the presence of a '^{56}Ni hole.' Therefore, nickel features may offer the best diagnostic for ejecta masses below M_{Ch} if ejecta do or do not have ^{56}Ni holes as predicted by 1D modeling.

In the optical nebular spectra at +100 and +200 days (Figures 26 and 27), the [Ni II] $\lambda\lambda$7378, 7412 lines are blended, and hence not very useful for abundance determinations. However, in the NIR there is a forbidden [Ni II] transition ($3d8(^3F)4s^2\,F_{7/2} - 3d8(^3F)4s^4\,F_{9/2}$) at 1.939 μm which in our synthetic spectra is relatively blend-free. It overlaps with telluric lines in low-redshift SNe, but higher redshift ($z > 0.08$) SNe avoid telluric absorption. While observations of this line appear to be rare, Friesen et al. (2014) find evidence for this line in spectra of SN2011fe, SN2014J, and SN2003du.

In our models, SUB1 shows no evidence of [Ni II] 1.939 μm. On the other hand, SUB2, CHAN, and SUP show the line, with a strength that correlates with ejecta mass. The absence of [Ni II] 1.939 μm in SUB1 arises from two effects — SUB1 has a smaller amount of stable nickel (see Table 3) and a higher ionization than the other models. The presence of ^{56}Co under $\sim$3000 km s^{-1} in SUB1 means that there is a great amount of heating from positrons, which deposit their energy locally (Figure 22). This, combined with the lower densities, leads to both a higher temperature, and a higher ionization (Figures 20 and 21). Surprisingly, and despite their similar ionization potentials, Fe II cannot be used as an ionization tracer for Ni II. In SUB1 Ni III/Ni II is significantly larger than Fe III/Fe II. This arises because the photoionization of Ni II is dominated by large resonances in its photoionization cross-section. Therefore, the absence of [Ni II] 1.939 μm in SN Ia spectra at 100–200 days indicates that the mass of the progenitor is below M_{Ch}. However, we re-emphasize that SUB2 is a scaled M_{Ch} model, so it is not a true sub-M_{Ch} model. SUB2 has a stable nickel core and shows [Ni II] 1.939 μm.

3.4.2 Ionization

Once the ^{56}Ni mass is determined via "Arnett's rule", which states that the luminosity at bolometric maximum is equal to the ^{56}Ni decay chain luminosity, or using LC fitting like that of Scalzo et al. (2014a,b), one can separate different SNe Ia based on ejecta mass using differences in ionization/temperature (see Figure 20). This result follows from the heating per gram available to the gas. The greater the ejecta mass is, the lower the heating rate per gram is. Consequently, ejecta with a larger $M(^{56}\mathrm{Ni})/M_{\mathrm{ej}}$ are hotter – see Blondin et al.

(2017) for $\dot{e}_{\rm decay} \equiv L_{\rm decay}/M_{\rm tot}$. Indeed our models indicate that low mass WD models, for a given ^{56}Ni mass, maintain higher ionizations throughout their spectral evolution.

3.4.2.1 UV Blanketing Previous studies focused on the UV variability and used the UV spectral region for understanding SNe Ia. These studies looked at the role of metallicity on UV blanketing (Lentz et al., 2000; Walker et al., 2012; Wang et al., 2012; Foley & Kirshner, 2013) finding that lower metallicities shift the blanketing blueward. Foley et al. (2016) looked at a sample of SNe Ia and found the UV diversity linearly correlates with the optical LC shape. In particular, the strength of UV line flux measurements (∼2030 & 2535 Å) increases with increasing $\Delta m_{15}(B)$. Other studies of UV variation hope to use it as a cosmological utility (Ellis et al., 2008; Sullivan et al., 2009) to improve standardizability. Therefore, understanding how $M_{\rm ej}$ for a given ^{56}Ni mass influences the UV spectrum is important to the astronomical community.

Until the ejecta begins entering its nebular phase (∼100 days), we see larger UV blanketing shortward of 4000 Å for larger mass ejecta. This effect is attributed to a temperature difference between models. We see in Figures 20 and 21 that below 25 000 km s^{-1} models with higher temperatures have higher ionizations, seen as a shift in the line blanketing to higher frequencies. Pre-maximum spectra show the Ca II feature (H & K lines near λ3500) is affected by UV blanketing, making it difficult to distinguish in SUP and CHAN (Figure 23). Ti II contributes to much of the blanketing more than 5 days before maximum, while Ti II, Fe II, and Fe III shape the UV spectra just prior to maximum. Around maximum, Co II contributes much of the UV blanketing (below 3500 Å) with the strongest blanketing occurring in model SUP. Looking inwards of 25 000 km s^{-1}, SUB1 and SUB2 show a higher ionization of cobalt than that of models SUP and CHAN. For Co II there is about a half dex difference in ionization between SUB1 and SUP. These Co II differences show up as absorption affecting the slope of the feature at ∼ 3500 Å. Post-maximum (Figures 24 and 25), there is less variation in UV blanketing between the models.

If we compare the peak fluxes at bolometric maximum (Figure 23) of three UV features (namely the features near ∼2850 Å, ∼3150 Å, and ∼3550 Å), we can characterize the level of blanketing by comparing the flux at peak in each feature. For all ejecta models,

the flux ratio $F(3150)/F(2850)$ is close to unity (0.93, 1.07, 1.03, and 1.11 for SUB1, SUB2, CHAN, and SUP). However, comparing these lines to the feature just short of the Ca II H&K lines and Si II ∼3660 Å absorption profile, we see that the flux ratio $F(3550)/F(2850)$ is strongly dependent on ejecta mass. This flux ratio $F(3550)/F(2850)$ is 0.99, 1.01, 1.20, and 1.75 for SUB1, SUB2, CHAN, and SUP. These UV features reflect the temperature and ionization of the ejecta and offer a diagnostic of ejecta mass for a given ^{56}Ni mass.

3.4.2.2 Optical and IR Besides variations in UV blanketing, other ionization diagnostics are seen in optical and infrared spectra. For instance, leading up to maximum (Figure 23), each model shows a different strength of the Si III triplet ($\lambda\lambda$4553, 4568, 4575) absorption, which is strongest in the models SUB1 and SUB2. SNe Ia typically classified as normal, such as SN2011fe, show the Si III feature around 4400 Å (Pereira et al., 2013) as our model CHAN does. SNe Ia such as SN2003hv, thought to be a sub-M_{Ch} event (Mazzali et al., 2011), show this absorption feature much more strongly (Leloudas et al., 2009), as in our SUB models.

Post maximum (Figure 25), the near-infrared part of the spectrum begins to show prominent permitted Fe II (9997.58, 10501.50, 10862.64, 16787.18, and 16873.20 Å) and Co II features (11829.72, 15758.43, 16064.48, 16360.46, 16687.30, 21344.70, 21503.28, 22202.92, 22475.63, and 23612.53 Å), as well as forbidden [Fe III] (22178.21, 22420.43, and 23478.80 Å) and [Co III] (12724.19, 15483.56, 17408.66, 19575.24, 20022.57, and 20973.15 Å) lines. Many of the Co II and Fe II features are absent in SUB1, a result of the higher ionization.

Optical nebular spectra typically exhibit emission lines of Fe III and Co III (Figures 26 and 27). In the NIR S^{2+} and Ar^{2+} show up in our model spectra as [S III] $\lambda\lambda$9068, 9530, and [Ar III] $\lambda\lambda$7135, 7751, with the strength of these features relative to [Fe III] λ4658 correlating with higher ejecta mass. As will be discussed in section 3.6.3, our model spectra tend to exhibit too high an ionization, especially after 40 days. In particular, they lack strong [Fe II] (e.g., [Fe II] ∼4350 Å). However [Fe II] and [Co II] features are readily identified in the IR, except for model SUB1. Since SUB1 comes from the explosion of a sub-M_{Ch} WD, its inner density is lower throughout its evolution compared to SUB2, and this hinders recombination. Further, SUB1 lacks the '^{56}Ni hole' seen in the later models, and hence the

temperature in the inner region is higher than in the other models (see Figures 20, 21, and 22).

3.4.3 C/O and IMEs

As the mass of C/O and IMEs is strongly correlated (by design from the density scalings) with the ejecta mass for a given ^{56}Ni mass (see Table 3), one should expect that lines from C/O and IMEs will provide a useful diagnostic tool for ejecta mass. As to be expected, our models show stronger absorption features for oxygen and IMEs for increasing ejecta mass. For example, the strength of absorption due to the O I $\lambda\lambda$7772, 7774, 7775 triplet absorption correlates with ejecta mass in pre-maximum spectrum (Figure 23). The feature fades by a few weeks post bolometric maximum. Mg II $\lambda\lambda$9218, 9244 is another feature whose strength correlates with high ejecta mass – see Table 5 which lists the pseudo-equivalent widths (pEWs) measured by a straight line across the maxima of the absorption profile; it also fades within a few weeks post bolometric maximum.

Si II $\lambda\lambda$5958, 5979, observed roughly around $\sim\lambda$5750, is a spectroscopic classification diagnostic for SNe Ia ($\mathcal{R}$(Si) $\equiv$ pEW(Si II λ5750)/pEW(Si II λ6100)) and, like other IME features, its strength correlates with ejecta mass. Table 5 highlights the correlation of pEWs of various features with ejecta mass of our models. Post maximum (Figures 24 and 25), we see the strength of the emission increase, giving a large morphological separation between models. Calcium (as Ca II) also shows the same behavior as Si II. The absorption and emission strength of the Ca II NIR triplet distinguishes models throughout the spectral evolution. We find that the strength of this feature correlates with ejecta mass. We further discuss the Ca II NIR triplet and the Si II $\lambda\lambda$6347, 6371 doublet in section 3.6.1.

3.5 EXPLOSION SCENARIO: SUB1 VS. SUB2

Since the explosion process and progenitor system are unknown, we highlight and summarize useful diagnostics for distinguishing our models of the same $M_{\rm ej}$. As mentioned earlier, SUB1

comes from a detonation model of a sub-M_{Ch} WD, while SUB2 comes from the DDT of a M_{Ch} WD, which was scaled in density to have the same mass as SUB1 and the same ^{56}Ni mass. Since SUB1 was detonated as a sub-M_{Ch} WD, it had lower densities when exploded compared to SUB2 and lacks the '^{56}Ni hole'. Without the '^{56}Ni hole', SUB1 has a larger (assumed) local deposition fraction from decay positrons compared to the total decay energy deposition (Figure 22) for velocities less than 5000 km s^{-1}. This keeps the inner region of SUB1 hotter than SUB2, which shows stronger features of higher ionization states of IGEs as the ejecta evolves past the photospheric phase and exposes the inner iron-rich material. At nebular times, the strength of [Ni II] 1.939 μm gives a clear distinction between SUB1 and SUB2, as the lower density ejecta model SUB1 does not show this feature.

Up to maximum light, SUB1 and SUB2 possess very similar spectra (Figure 23), especially in the optical. However, as the photosphere begins to recede inwards differences are seen in the NIR – Fe II and Co II features are absent in SUB1 but present in SUB2 (Figures 24 and 25). Below 5000 km s^{-1}, the densities in SUB1 are roughly a factor of 3 lower than in SUB2. Further, SUB1 has a larger fraction of local radioactive heating from positrons. These factors inhibit recombination and a higher ionization persists in SUB1 compared to SUB2. The NIR region is potentially the best diagnostic for the ionization state of the ejecta in SNe Ia (shown in Figures 26 and 27).

This higher ionization, seen in post-maximum spectra (Figures 24 and 25), yields lower fluxes in the NIR. We see roughly half a magnitude difference in the post maximum I, J, and H bands. However, the magnitude difference between J and H grows to $\sim$2 mag difference by 200 days post maximum.

3.6 ADDITIONAL INVESTIGATIONS

In this section we present additional investigations of our ejecta models focusing on high velocity features and comparisons to observational data. We also explore shortcomings with our ejecta models.

3.6.1 High Velocity Features – Si II & Ca II

High velocity features (HVFs) are absorption features, seen in the strongest lines, that show a distinct difference in velocity (often early and prior to maximum), by more than a few thousand $\mathrm{km\,s^{-1}}$ from the lower velocity, photospheric component (Gerardy et al., 2004; Mazzali et al., 2005a,b). Note the two strongest components of the Ca II NIR triplet (λ8542 & λ8662) are separated by $\sim$4000 $\mathrm{km\,s^{-1}}$. Thus, any single Ca II NIR profile may show an absorption feature with two components separated by a few thousand $\mathrm{km\,s^{-1}}$ which is different from a HVF. In many SNe Ia, HVFs have even been observed at maximum for the Ca II NIR triplet but not for Si II $\lambda\lambda$6347, 6371 (Childress et al., 2014). There is no clear indication when HVFs start to disappear in all observed cases. Silverman et al. (2015) state that the HVF Ca II triplet begins to disappear around -1 days prior to maximum for $\Delta M_{15}(B) = 1.4$ to 1.6 mag, however discoveries of HVFs are potentially biased towards those that persist closer to maximum light.

Shown in Figures 28 and 29 is the evolution of the Si II doublet and the Ca II NIR triplet, with a vertical line at $-15\,000\,\mathrm{km\,s^{-1}}$ as a reference. In all models, Ca II HVFs are seen before bolometric maximum ($\lesssim -11$ days). However, no HVF for Si II $\lambda\lambda$6347, 6371 is seen. Notice the striking difference in the pre-maximum Ca II triplet profile ($\lesssim -11$ days) and the profile at later dates. The lack of a Si II doublet HVF could just be a byproduct of atomic physics. Although both the Ca II NIR triplet and the Si II doublet are not resonance transitions, the lower level of the Ca II triplet is metastable. The lower level of the Si II λ6355 doublet is the 4s state which is coupled to the ground state by a permitted transition. Therefore, when compared to the Si II λ6355 doublet, the Ca II NIR triplet persists longer because the metastable lower level population persists longer.

By defining a straight line between the maxima on either side of the absorption profiles of these Si II features, we are able to compute our models' pEWs (listed in Table 5). Comparing our work to figure 8 of Blondin et al. (2012), we find our spectra are clustered around those labeled broad-lined Ia as seen in Figure 30. Branch et al. (2006) looked at the pEWs of Si II features near λ6100 and λ5750 in these spectra at maximum in order to group these spectra in different classifications: "core-normal", "broad-line", "shallow-silicon", and

"cool". The most massive model, SUP, might fall under the "cool" classification from Branch et al. (2006), but it lacks the strong Ti II absorption.

3.6.2 Comparison to Data

Here we present both light curve and spectral comparisons to data for a span of spectral epochs. We focus on SNe Ia that have claimed ^{56}Ni masses similar to that of our models (0.6 $M_\odot$) or similar $\Delta m_{15}(B)$ and those tagged as sub-M_{Ch} (SN2005el), M_{Ch} (SN1995D), and similar Branch types (SN2001ay). We used the supernova identification program SNID (Blondin & Tonry, 2007) on models at bolometric maximum to find additional SNe Ia to compare (SN1994ae). The spectra are taken from the CfA Supernova Archive (Blondin et al., 2012). Archived light curve photometry is taken from Open Supernova Catalog (Guillochon et al., 2017). When comparing models to observations, the spectra are normalized between λ_{min}=4000 Å and λ_{max}=7000 Å, such that

$$\frac{1}{\lambda_{max} - \lambda_{min}} \int_{\lambda_{min}}^{\lambda_{max}} F_\lambda d\lambda = 1 \text{ erg cm}^{-2} \text{ s}^{-1} \text{ Å}^{-1} \tag{3.1}$$

Normalizing spectra allows us to better compare spectral features, removes uncertainties in distance, and compensates for small differences in ^{56}Ni mass. To compare LCs, we correct for extinction using the CCM reddening law (Cardelli et al., 1989) and literature $E(B-V)$ and R_V values. We normalize the LCs by adding a constant offset (model and object dependent), such that $B_{max} = 0$ mag at $t(B_{max})$. We also shift the LCs so that time of B-band maxima agree. Thus, uncertainties in distance and explosion time are reduced. A constant value of 0.05 mag is included with the photometric error bars for uncertainty in reddening. K-corrections, expected to be small, have not been applied. Photometric band magnitudes and bolometric luminosities of the models at maximum are provided in Table 4.

3.6.2.1 SN1994ae SN1994ae exploded in NGC 3370 ($z = 0.0043$ – Riess et al., 1999; Jha et al., 2007) and was first discovered on 14 November 1994 by van Dyk et al. (1994). It reached B-band maximum ($m_B = 13.21$ mag) on MJD 49685.5 with $\Delta m_{15}(B)$=0.96 mag (Riess et al., 1999; Jha et al., 2007). For comparison, we reddened our models using

$E(B-V) = 0.0226$ mag and $R_V = 3.1$ (Jha et al., 2007). Figure 31 shows the spectral comparison of SN1994ae at +0.0, +10.0, and +152.7 days after B-band maximum and normalized LCs relative to band maximum are shown in Figure 32.

At +0 days, our model spectra do not reproduce the velocity of the Si II λ6355 doublet and UV Si II triplet. Results by Dessart et al. (2014b) suggest SNe Ia resulting from pulsational-delayed detonations (PDD) retain more unburnt carbon and have little mass at high velocity ($\gtrsim$15 000 km s^{-1}) due to pulsations. Therefore, spectral features of SN1994ae might be best explained by PDD modeling, and would resemble similar radiative properties of DDT models. The spectra also show evidence of the Si III triplet ($\lambda\lambda$4553, 4568, 4575) absorption as in our SUB models (an indication of high ionization). Later spectra show cooler ejecta and model SUP is closest to reproducing the features. However, at nebular times (+152.7 d) our model optical [Fe III] lines appear too strong and [S III] $\lambda\lambda$9068, 9530 are absent in the observational data.

For the light curve comparison, we shifted the LCs to give the same time of $B_{\rm max}$ and reddened the models with $A_B = 0.091$, $A_V = 0.070$, $A_R = 0.057$, and $A_I = 0.041$ mag, obtained using $E(B-V) = 0.0226$ mag and $R_V = 3.1$ from Jha et al. (2007). We normalized the light curves to 0 mag at $B_{\rm max}$ and shifted the observational data by 12.98 mag. We see in Figure 32 that our B-band LC is consistent until 20 days post maximum, where our LCs begin showing roughly half a magnitude more flux. Model CHAN matches well the V/R-band observations. However, our models fail to reproduce the second peak in the I-band, and the disagreement is greater in lower mass models.

3.6.2.2 SN1995D SN1995D exploded in NGC 2962 and was discovered on 10 February 1995 (Nakano et al., 1995). Its redshift is $z = 0.0067$, and it reached B-band maximum (m_B=13.44 mag) on MJD 49768.7 (Riess et al., 1999; Jha et al., 2007). SN1995D has been argued as having a ^{56}Ni mass of about 0.58 M$_\odot$ and an ejecta mass around 1.45 M$_\odot$ (Childress et al., 2015). For comparison, we reddened our models using $E(B-V) = 0.026$ mag and $R_V = 3.1$ (Jha et al., 2007).

Figure 33 shows the spectral comparison of SN1995D at +3.6, +42.5, and +93.5 days after B-band maximum. The early epochs (+3.6 days) show good qualitative agreement with

SUB1 except our model shows a larger blueshifted Si II doublet. This may be best explained by a PDD model (Dessart et al., 2014b). SUB1 also matches the UV spectrum shortward of 4000 Å. At later epochs like +42.5 and +93.5 days, we see a better agreement to model SUP and to CHAN, due to lower temperatures and ionization. Roughly all features at +93.5 days are matched by SUP. Despite the calculated ^{56}Ni and ejecta mass being closest to CHAN, SN1995D shows only moderate qualitative agreement at later epochs. SN1995D transitions from looking like our SUB1 into that of SUP from early to late epochs.

To compare light curves, we shifted the LCs to give the same time of $B_{\rm max}$ and reddened the models with $A_B = 0.106$, $A_V = 0.081$, $A_R = 0.066$, and $A_I = 0.048$ mag, obtained using $E(B-V) = 0.026$ mag and $R_V = 3.1$ (Jha et al., 2007). We normalized the light curves to 0 mag at $B_{\rm max}$ and shift the observational data by 13.35 mag.

In Figure 34, we see that our B-band LC is consistent with all models until ∼12 days post maximum, where our LCs then begin showing roughly half a magnitude more flux. Model CHAN matches well the V/R-band observations. Our models fail to reproduce the second peak in the I-band (it occurs 10 to 20 days too early) although the SUP model matches the data at late times. Model SUP also seems consistent with the peak flux ratios in SN1995D.

3.6.2.3 SN2001ay SN2001ay exploded outside IC 4423 and was discovered on 18 April 2001 by Swift et al. (2001). Krisciunas et al. (2011) and references therein cite its redshift as $z = 0.0302$ and indicate that it reached B-band maximum ($M_B = -19.19$ mag) on 23 April 2001. For spectral comparison, we reddened our model spectra using $E(B-V)_{MW} = 0.026$ mag, $E(B-V)_{\rm host} = 0.072$ mag, and $R_V = 3.1$ (Krisciunas et al., 2011). Krisciunas et al. (2011) states a $M(^{56}\mathrm{Ni})$ of $(0.58\pm0.15)/\alpha$ $\mathrm{M}_\odot$, for an $\alpha = L_{\rm max}/E_{\rm Ni}$, typically between 1–1.2. Given the close proximity between the estimated ^{56}Ni mass for SN2001ay and that of our model set, we explore the spectral similarities.

Figure 35 shows the spectral comparison for epochs −1.5, +9.3, and +56.3 days relative to B-band maximum. All models provide a good qualitative fit to the optical spectrum at −1.5 days, with SUP exhibiting the worst fit. While all models fit the Si II $\lambda\lambda$6347, 6371 doublet in absorption strength and velocity, our models show stronger absorption in the

Si II $\lambda\lambda$5041, 5056, 5056.3 triplet around 4800 Å. Blended with this feature is absorption arising from Fe II λ5018, and this is also somewhat too strong in the models. The biggest discrepancy between model and observation for the blend occurs for model SUP. SUB1 lacks absorption at ∼4000 Å, which is clearly present in the observations, and all of the other models. No model reproduces the shape of the UV absorption near 3700 Å, which could be due to a discrepancy with the Ca II H&K lines.

Later, model SUP qualitatively agrees best with the SN2001ay spectra at +9.3 and +56.3 days. At +9.3 days, SUP shows agreement despite its stronger Fe II absorption lines around 4800 Å. At +56.3 days, the spectra is dominated by Fe II features, which SUP matches well given its cooler temperatures and lower ionization. Models SUB1, SUB2, and CHAN are too highly ionized, and exhibit too much emission from higher ionization states such as Fe III. Despite matching much of the optical spectrum, SUP does not match well the absorption features associated with the Ca II NIR triplet and the Ca II H&K lines. Given the discrepancy with calcium at −1.5 days, this may indicate that the calcium abundance is too high, or that the distribution in velocity space is incorrect.

For the light curve comparison, we reddened the models with $A_B = 0.397$, $A_V = 0.307$, $A_R = 0.148$, and $A_I = 0.178$ mag, by combining host and MW values as $E(B-V)$=0.098 mag and R_V=3.1 (Krisciunas et al., 2011). We normalize the light curves to 0 mag at $B_{\rm max}$ and shift the observed data by 16.35 mag. Figure 36 shows our models fail to reproduce the post maximum decline except for U/B-bands. Our models show too little $V/R/I$ flux in the decline post maximum, but SUP agrees in peak flux ratios between bands with SN2001ay.

3.6.2.4 SN2005el SN2005el exploded in NGC 1819 and was discovered on 19 September 2005 (Madison et al., 2005) at a redshift of $z = 0.0148$ (Hicken et al., 2009). It reached B-band maximum ($m_B = 14.84$ mag) on MJD 53646.4 (Hicken et al., 2009). Scalzo et al. (2014a) classified SN2005el as having 0.9 $M_\odot$ of ejecta as well as 0.54 $M_\odot$ of ^{56}Ni, which, considering the errors in the determinations, are close to our models SUB1 and SUB2. For comparison, we applied reddening to our models using $E(B-V) = 0.136$ mag and $R_V = 3.1$ (an $E(B-V)$ value that is higher than that stated in Scalzo et al. (2014a)).

Figure 37 shows our spectral comparison to SN2005el. The early epochs of −5.9 and +2.1 days show some qualitative agreement, mostly with SUB1 and SUB2. At this epoch, our models do not reproduce the Si II $\lambda\lambda$6347, 6371 doublet. Our models indicate a Si II $\lambda\lambda$6347, 6371 doublet formed at higher velocities. Therefore, spectral features of SN2005el may be best explained by a PDD model. Unlike the Si II doublet, models CHAN and SUP do reproduce the S II 'w' feature. Since our models show a higher blue-shifted Si II doublet, it is not surprising that our UV does not match, given other Si II and Ca II H&K features in this region. If the Ca II H&K lines and Si II $\lambda\lambda$3854, 3856, 3862 triplet are separated by thousands of km s^{-1}, then it is likely to result in the spike seen at the bottom of the 3700 Å absorption feature, whereas our models show one broad absorption feature around 3700 Å – seen in SN2008ec, for example. Given the strong absorption profile around 4400 Å, we suggest this is the Si III $\lambda\lambda$4553, 4568, 4575 triplet, indicating a high ionization at this epoch.

At +24.9 days, we see that model SUP agrees qualitatively in almost all features. Other models are too blue compared to the cooler SUP model. This is surprising given the claim that SN2005el is a sub-M_{Ch} SN with an ejecta mass of only 0.9 $M_{\odot}$. The discrepancy around 5300 Å could be the result of differences in the Fe II or Cr II absorption.

One should expect SUB1 or SUB2 to resemble the spectral evolution of SN2005el; however, we only see that SUB1 matches prior to maximum and does not match SN2005el at late epochs, where SUP shows best agreement. There are several possible explanations for the inconsistencies. First, the ^{56}Ni mass may be lower than 0.54 $M_{\odot}$. Second, the poor agreement in the extent of the Si II $\lambda\lambda$6347, 6371 doublet could indicate a different explosion scenario (such as PDD mentioned earlier – little mass at high velocity).

To compare light curves, we shifted the LCs relative to the time of $B_{\max}$ and reddened the models with $A_B = 0.543$, $A_V = 0.414$, $A_R = 0.339$, $A_I = 0.245$, $A_J = 0.122$, and $A_H = 0.077$ mag, obtained using $E(B-V) = 0.136$ mag and $R_V = 3.1$ (slightly higher than Scalzo et al. (2014a)). The light curves were normalized to 0 mag at $B_{\max}$ and we adjust the observational data by 14.76 mag. In Figure 38, we see the optical bands are reproduced well with our SUB models (except B beyond 20 days). Although the late time behavior in the H-band is reproduced, the NIR LCs do not generally agree with the SUB models. The double peak structure in the J-band observations is well produced by the models, although

in the H-band it is less evident.

3.6.3 Model Setbacks and Theoretical Problems

When compared to observation data, our models do show a higher ionization, especially in the nebular phase. The strength of the [Fe III] λ4658 feature is too strong compared to other optical/NIR features. Further, optical spectra lack emission such as [Fe II] $\sim\lambda$4350 emission, seen in nebular spectra of SNe Ia of Taubenberger et al. (2013b) and Black et al. (2016), for example. Other researchers have also had difficulty modeling the Fe II feature near 4350 Å (Spyromillo 2016, private communication; Sim 2016, private communication; Mazzali et al., 2015; Friesen et al., 2017). It is not surprising that these models struggle to get the ionization correct – there are no free parameters and the density structure and element distribution is set by the adopted initial model.

At late times the super-M_{Ch} model was generally in better agreement with observation – a result of the model being cooler with lower ionization. Since we know that most of the observed SNe we discussed are not super-M_{Ch}, there is a fundamental problem with the models. This problem might arise from the adopted explosion models, be related to assumptions about mixing and clumping, and/or be a problem in the ionization calculations. Since nebular spectra show strong [Fe II] and [Fe III], the Fe^{+}/Fe^{2+} ratio must be of order unity, and consequently it is sensitive to the Fe atomic models (and the density structure).

The disconnect between early and late time modeling is not unexpected. Early time spectra are dependent on the outer ejecta whereas late time spectra are primarily dependent on the inner ejecta. Further, the processes determining the observed spectra in the photospheric and nebular phases are distinct, and subject to different uncertainties in the atomic data.

Another problem is the strong nebular [S III] $\lambda\lambda$9068, 9530 and [Ar III] $\lambda\lambda$7135, 7751 lines. The [S III] $\lambda\lambda$9068, 9530 does not seem to appear in nebular spectra. However, it is not clear if [Ar III] λ7135 is present. There are three additional transitions contributing to that overall feature between 7000-7500 Å. There are two [Fe II] $\lambda\lambda$7155, 7172 lines that overlap [Ar III] λ7135 and, depending on the ionization structure of the ejecta, it becomes

difficult to determine the source of the feature in observations. However, atomic physics of the [Ar III] $\lambda\lambda$7135, 7751 lines requires that the line ratio, $I(7135)/I(7751)$, should be a factor of 4.2, so if spectral detections of [Ar III] λ7751 are possible, then one can determine the strength of the blended [Ar III] λ7135 line. However, observed SN Ia nebular spectra appear absent of IME lines. This could be due to an absence of ^{56}Ni in the IME zone. In our models, the presence of some ^{56}Ni in the IME zone means that positrons are available as a heating source after the ejecta has become optically thin to γ-ray photons. One would expect some level of mixing to occur through Rayleigh-Taylor instabilities between these layers – see Hicks (2015) and references therein. To address the problem of too high an ionization, clumping, arising from radiation hydrodynamic instabilities, should be considered in future studies. Our preliminary work shows that, as expected, clumping lowers the ionization, and we will address this issue in chapter 4.

Another possible explanation concerns the validity of the explosion models. We have considered only four models, and only two of the explosion models were obtained from "first principles", and even these were derived from 1D explosions. Alternative explosion mechanisms might give rise to different density and abundance profiles, and in particular, the spatial distribution of ^{56}Ni. The later will influence the amount of UV line blanketing, potentially introducing degeneracies with the ejecta mass. However, other diagnostics (e.g. the NIR nickel line) provide additional information, and can break the degeneracies. Further, despite the deficiencies, the models have highlighted important diagnostics and questions that can help facilitate future progress towards understanding Type Ia SNe.

3.7 CONCLUSION

We have presented four 1D SN Ia models – three delayed detonation models with masses of 1.02, 1.40, and 1.70 $M_\odot$ and one detonation sub-M_{Ch} model with a mass of 1.04 $M_\odot$. By design, the models have the same ^{56}Ni mass of $\sim$0.62 $M_\odot$ which allows us to investigate the dependence of light curves and spectra on ejecta mass. Despite the smallness of the model grid they serve to highlight important diagnostics that can help facilitate future progress

towards understanding Type Ia SNe.

Our results show that despite large differences in ejecta mass, the optical flux during the photospheric phase shows less than 0.3 mag difference in peak brightness in the LCs, as well as nearly identical spectral features. We have seen that the peak bolometric luminosity of each model is similar to within about 15 percent, and the difference in rise time is less than ∼20 percent. Due to differences in diffusion time, however, the two sub-M_{Ch} mass models do evolve faster (pre-maximum) by a day as seen from the bolometric luminosity and synthetic B-band LCs. There is only a slight difference (∼5 percent) in the decline parameter, $\Delta M_{15}(B)$, between sub-M_{Ch} and super-M_{Ch} models. Our sub-M_{Ch} models have much bluer colors at all epochs compared with SUP ($B-R$ difference of $\approx$ 0.3 mag at maximum and a difference in $B-R \gtrsim 1$ mag roughly 20 days post maximum). Our models show larger differences in NIR light curves, particularly with the H-band's ∼1 mag difference at maximum light between sub-M_{Ch} and super-M_{Ch}.

Spectroscopically, at most photospheric phases, the optical spectra show the same gross features. However, the strength of UV blanketing between 2000-4000 Å is found to correlate with ejecta mass. Lower mass models have higher temperature and ionization (as more heating per gram), and hence lower UV blanketing between 2000-4000 Å. $M(^{56}\mathrm{Ni})/M_{\mathrm{ej}}$ is the leading parameter controlling this study. Higher mass models produce stronger IME features, such as the Ca II NIR triplet and the Si II λ6347,6371 doublet prior to the nebular phase, and stronger [S II] $\lambda\lambda$9530, 9068, [Ca II] $\lambda\lambda$7291, 7324, and [Ar III] λ7135 in the nebular phase. Lower mass models have higher ionization, as indicated by the presence of the Si III $\lambda\lambda$4553, 4568, 4575 triplet near maximum and the lack of strong Fe II and Co II lines in the optical post-photospheric/nebular phase. Model SUB1, unlike SUB2, is dominated by strong [Fe III] and [Co III] lines, such as [Fe III] λ4658, [Fe III] λ5270, [Co III] λ5888, and [Co III] 1.5484 μm.

In the nebular phase, the [Ni II] 1.939 μm line is absent in our sub-M_{Ch} detonation model, but readily visible in the three other models. Potentially, the [Ni II] 1.939 μm line provides us with a diagnostic of the amount of stable nickel (^{58}Ni & ^{60}Ni), unlike the blended optical [Ni II] $\lambda\lambda$7378, 7412 lines. Its absence in NIR spectra would provide strong evidence for a lack of a '^{56}Ni hole' and potentially sub-Chandrasekhar mass ejecta (given 1D modeling).

However, complex ionization issues can influence the strength of all [Ni II] lines, making absolute determinations of the abundance model-dependent. Overall the NIR provides the best diagnostics for distinguishing between our different SN Ia progenitor models.

In comparing our spectra to observation at times greater than 20 days post maximum, we consistently find better qualitative fits with our cooler, high mass super-M_{Ch} model. Given that there is a ∼20-70 percent difference in claimed ejecta mass between our compared observational objects and our super-M_{Ch} model, we suggest clumping as a way to lower the high ionization and high temperatures observed in our models. While it is difficult to reproduce all observational features due to the diversity of SNe Ia, we are able to match some features shown in our comparison to observations. Prior to maximum, the best choice of model varies. Agreement depends on the velocity structure of the ejecta. For instance, the photospheric features Si II $\lambda\lambda$6347, 6371 and the Ca II NIR triplet expose the difficulty of reproducing the velocity structure of SNe Ia (Figures 35 and 37, for example). Future efforts to reproduce the diversity of these features requires a better understanding of the outer ejecta and explosion mechanism.

Parallel work has been undertaken by Blondin et al. (2018) who studied SN 1999by using a low mass model ($0.9\,M_{\odot}$) and a model with a Chandrasekhar mass (both with $0.12\,M_{\odot}$ of ^{56}Ni). They find that the lower mass model provides a better match to the light curve, and exhibits a faster rise and a brighter maximum. As in our study, the lower mass model does not show the [Ni II] 1.939 μm line, which is seen in their Chandrasekhar model.

To determine more accurate diagnostic signatures of SN Ia progenitors we need to understand clumping and inhomogeneities in Ia ejecta. Some insights can be obtained from multi-dimensional explosion modeling, while additional insight might be obtained from studies of young SN remnants that are not interacting with the surrounding ISM. During the photospheric phase, more UV spectral data will help to constrain the ionization and temperature of the gas. More NIR spectral data will help to test our diagnostics, such as the NIR Ca II triplet (or nebular [Ca II] $\lambda\lambda$7291, 7324), the nebular features between 9000 Å-1 μm (such as [S III] $\lambda\lambda$9068, 9530), and the [Ni II] 1.939 μm line (requiring SNe Ia at a high enough redshift to avoid the telluric absorption). These nebular features can provide leverage on the progenitor channel by constraining initial densities ([Ni II]), the overlap between IMEs

and IGEs ([Ca II]), and the ionization structure.

As many more SN spectra become available it will be possible to do systematic statistical comparisons between SNe which have a similar initial ^{56}Ni mass. As discussed above, our studies show that Type Ia SNe will exhibit systematic differences in spectra and multi-band LCs as a function of ejecta mass, thus providing fundamental constraints on the nature of the progenitors.

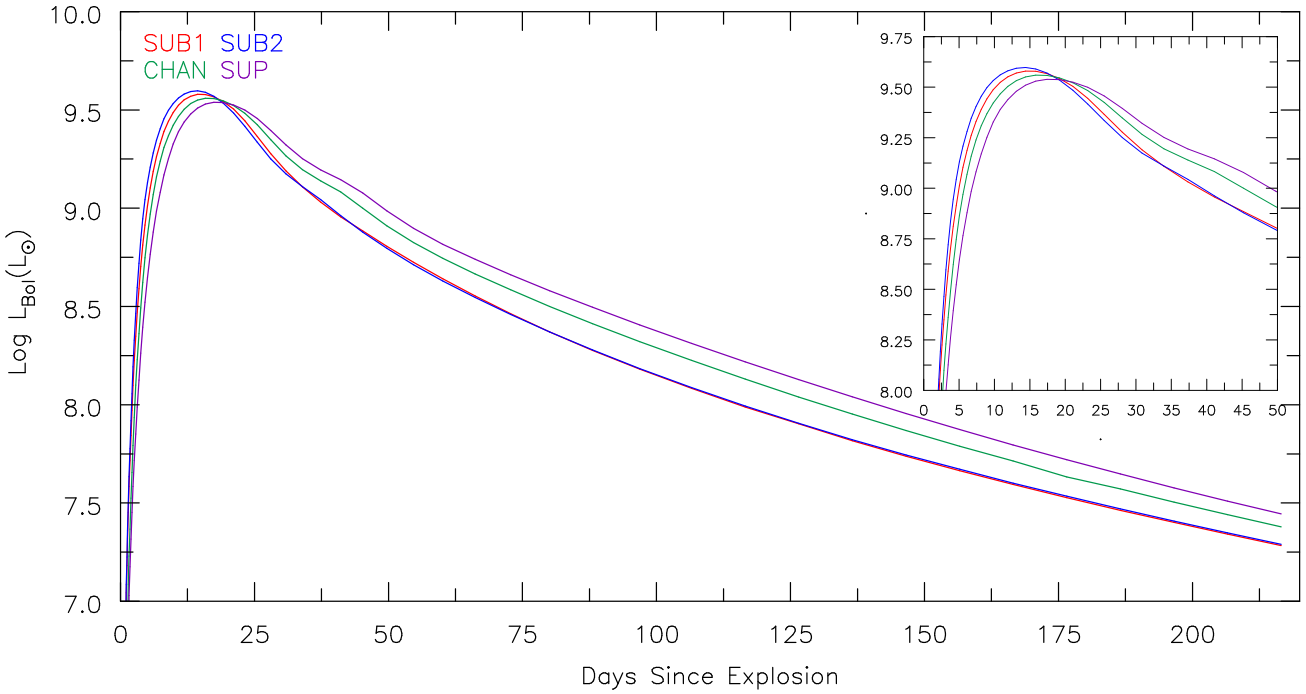

Figure 17 The bolometric luminosities for all models as a function of age since explosion. Lower mass models evolve faster in their bolometric light curves compared with higher mass models – the lower the ejecta mass, the earlier the time of bolometric maximum (Table 4).

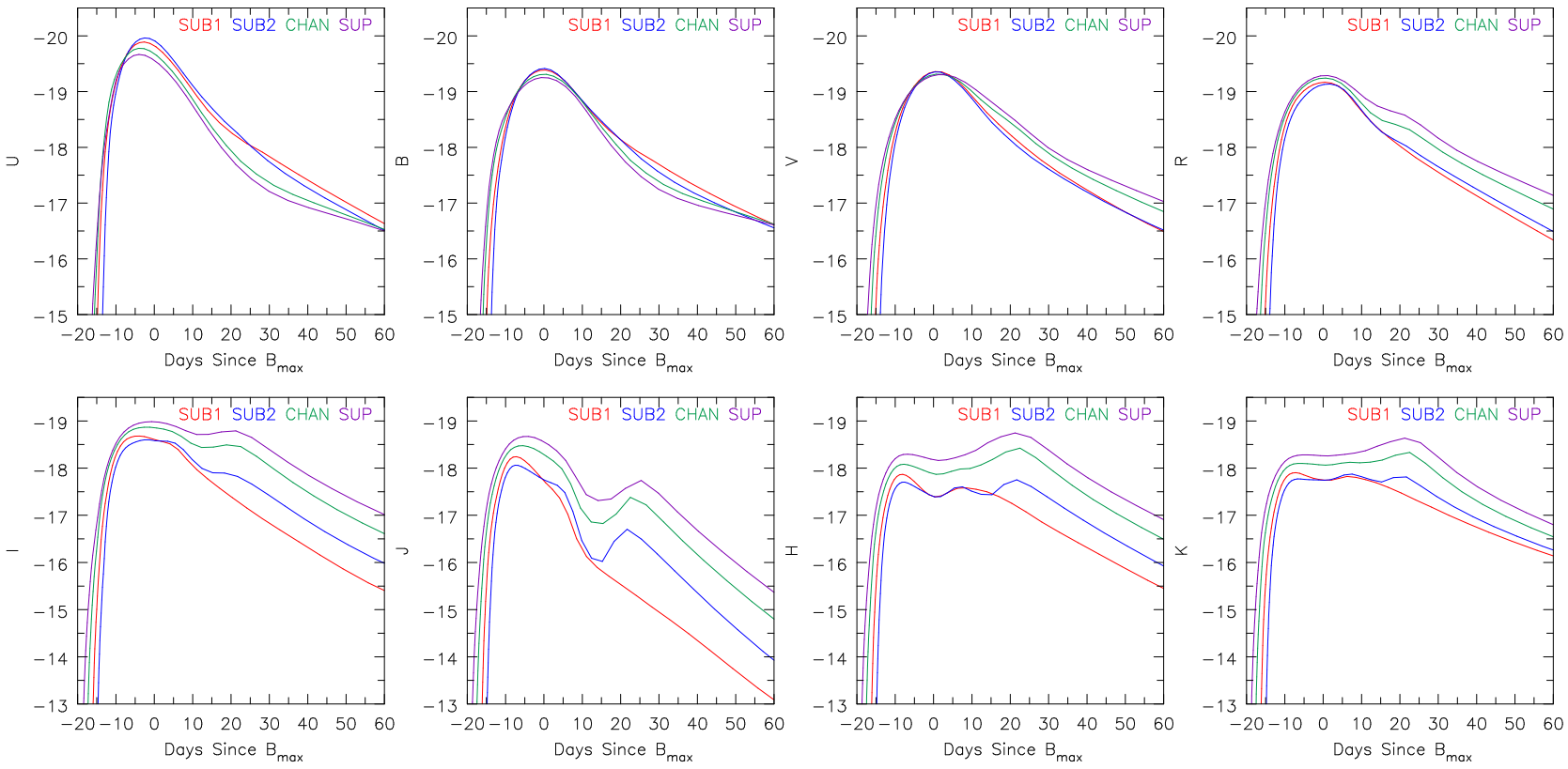

Figure 18 The plots show all LCs as a function of age since B-band maximum. Unlike the bolometric luminosity (Figure 17), the B-band LCs for SUB1 and SUB2 are different – SUB1 is roughly 0.2 magnitudes brighter than SUB2 between ∼25-60 days post B-band maximum. This difference in evolution arises because SUB1 lacks the '^{56}Ni hole' (Figure 16), and hence is hotter, and has higher ionization, at lower velocities than SUB2. The H-band shows a triple peak for model SUB2 as the ionization shifts downwards, enhancing charge 2+ and then 1+ ion abundances of IGEs like cobalt and iron.

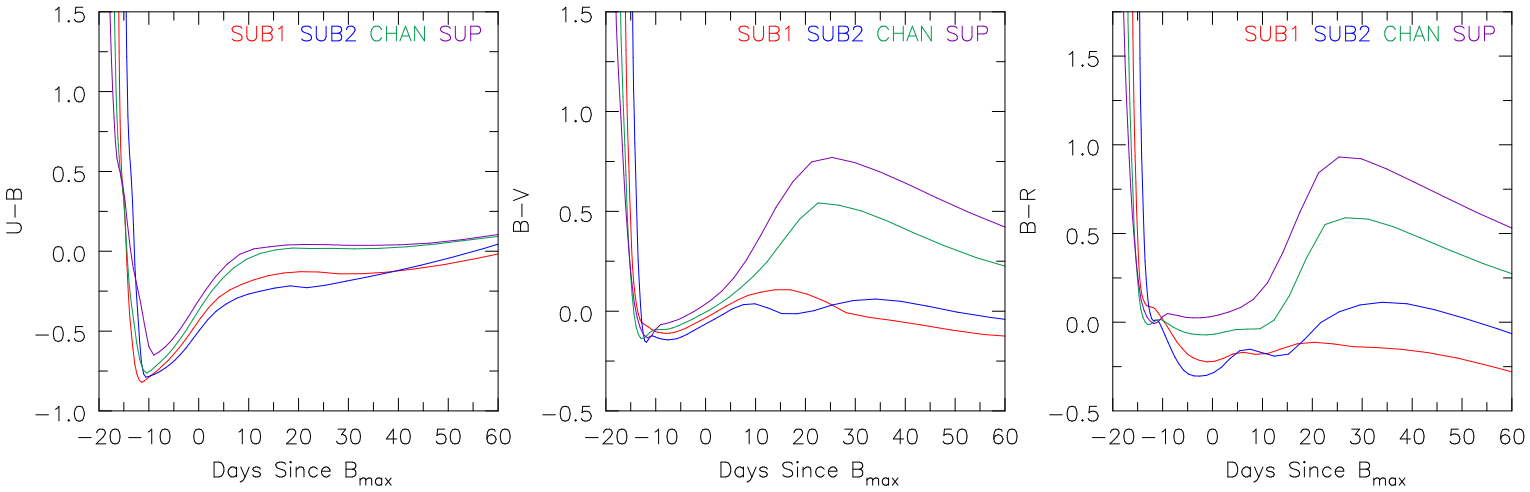

Figure 19 The $U-B$, $B-V$, and $B-R$ colors relative to B-band maximum. Models SUB1 and SUB2 show bluer colors for all epochs. Ten days before B-band maximum all models have similar colors. As the ejecta ages, differences in the $B-R$ color become much larger – at B-band maximum, the $B-R$ color differs by $\sim$0.3 mag between SUB2 and SUP, while at later epochs the color difference between SUB1 and SUP can be in excess of 1 magnitude.

Model	M_U (mag)	$t(U_{\max})$ (days)	$\Delta M_{15}(U)$ (mag)	M_B (mag)	$t(B_{\max})$ (days)	$\Delta M_{15}(B)$ (mag)	M_V (mag)	$t(V_{\max})$ (days)	$\Delta M_{15}(V)$ (mag)	M_R (mag)	$t(R_{\max})$ (days)	$\Delta M_{15}(R)$ (mag)
SUB1	−19.89	14.13	1.07	−19.39	16.97	0.95	−19.36	17.99	0.88	−19.17	17.40	0.89
SUB2	−19.96	13.35	1.08	−19.41	15.64	0.94	−19.36	16.48	0.96	−19.14	17.01	0.91
CHAN	−19.78	14.90	1.06	−19.31	18.54	0.94	−19.31	19.91	0.68	−19.24	18.92	0.76
SUP	−19.67	15.92	1.03	−19.25	19.86	0.99	−19.31	21.89	0.60	−19.29	20.48	0.59
	M_I (mag)	$t(I_{\max})$ (days)	$\Delta M_{15}(I)$ (mag)	M_J (mag)	$t(J_{\max})$ (days)	$\Delta M_{15}(J)$ (mag)	M_H (mag)	$t(H_{\max})$ (days)	$\Delta M_{15}(H)$ (mag)	M_K (mag)	$t(K_{\max})$ (days)	$\Delta M_{15}(K)$ (mag)
SUB1	−18.68	12.86	0.70	−18.24	9.60	1.54	−17.87	8.76	0.29	−17.90	9.62	0.08
SUB2	−18.60	13.76	0.64	−18.06	8.39	1.03	−17.70	7.81	0.09	−17.77	9.27	−0.08
CHAN	−18.87	16.41	0.44	−18.48	12.73	1.26	−18.08	10.73	0.10	−18.10	12.40	−0.02
SUP	−18.99	19.01	0.27	−18.67	15.29	1.17	−18.30	12.91	0.02	−18.28	15.25	−0.07
	$t_{-1/2}$ (mag)	$t_{+1/2}$ (days)	$t_{\max}$ (mag)	$L_{\rm bol}$ ($10^9 L_\odot$)								
SUB1	8.18	13.0	14.4	3.80								
SUB2	8.02	12.44	14.4	3.96								
CHAN	8.83	14.75	15.84	3.63								
SUP	9.27	16.57	17.42	3.47								

Table 4 Light curve parameters such as absolute magnitude maximum (M_X), time of maximum ($t(X_{\max})$), and decline parameter ($\Delta M_{15}(X)$) for band X. Also included are half light rise and decline times for $L_{\rm bol}$ ($t_{-1/2}$ and $t_{+1/2}$), time of bolometric maximum ($t_{\max}$), and maximum bolometric light ($L_{\rm bol}$).

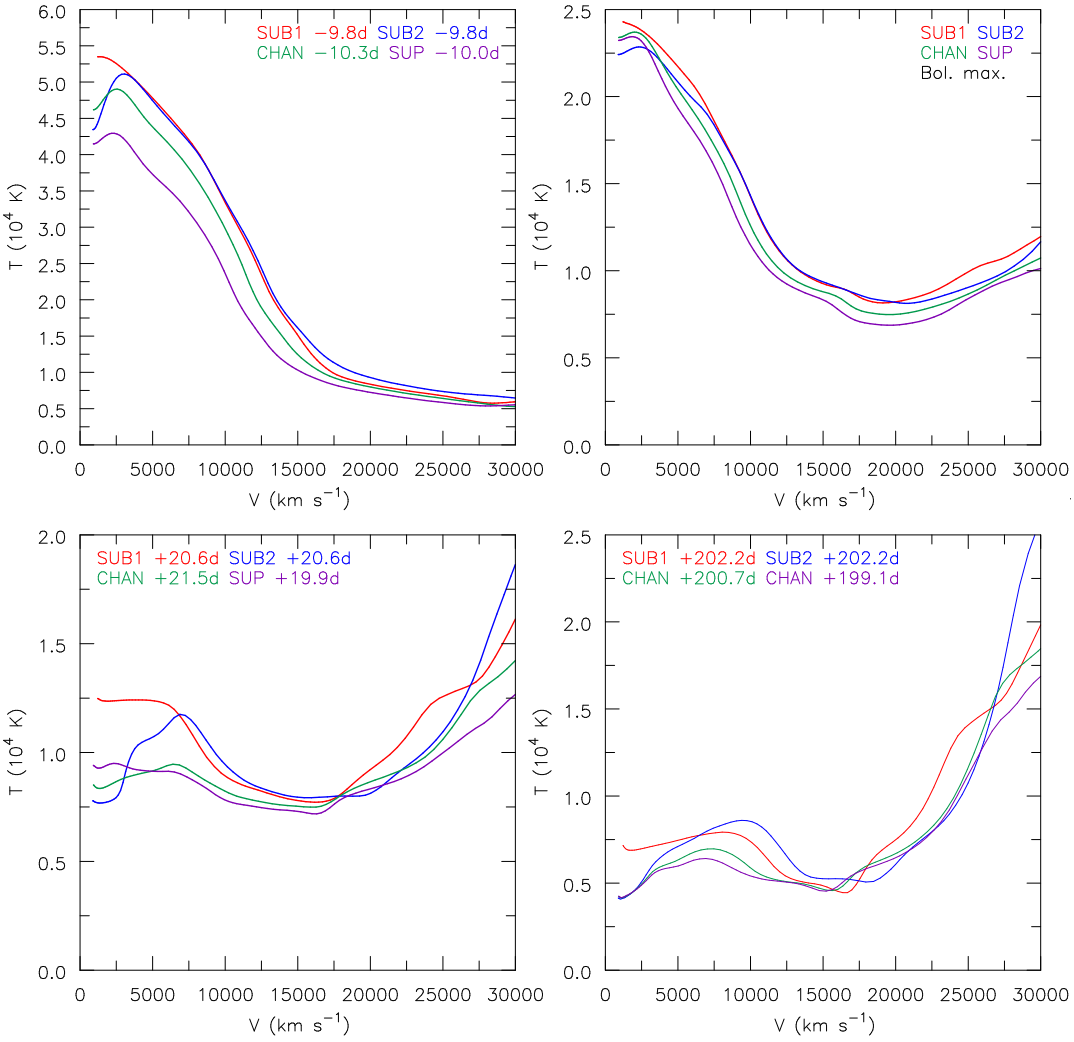

Figure 20 Temperature evolution as a function of velocity for models SUB1, SUB2, CHAN, and SUP at epochs −10, +0, +20, and +200 days relative to bolometric maximum. SUB1 exhibits higher temperatures at low velocities compared to SUB2, CHAN and SUP – the higher temperature arises because of the much higher ^{56}Ni abundance in the innermost ejecta of SUB1 (Figure 16).

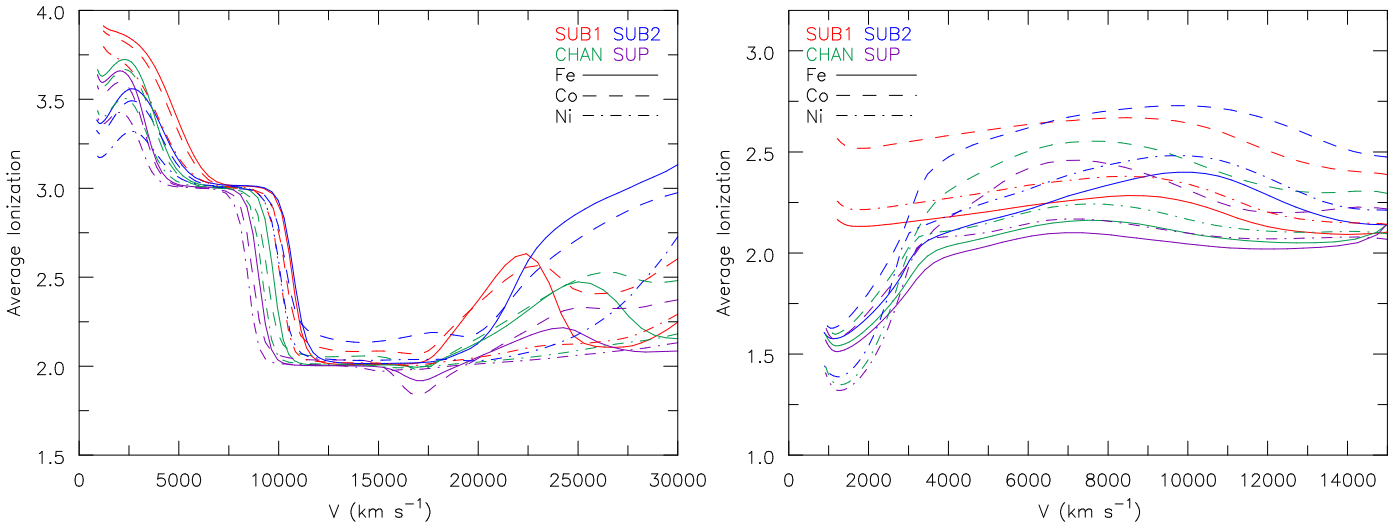

Figure 21 Average ionization state for bolometric maximum (left) and 216 days post-explosion (right) for IGEs. The average ionization is defined as the total number of free electrons from each species divided by the total species population. At bolometric maximum, the average ionization rises beyond 20 000 km s^{-1} due to the low densities inhibiting recombination. The average ionization state is higher for sub-M_{Ch} models, a result of more heating per unit mass. At nebular times, SUB1 remains at a higher average ionization in the inner region due to a larger deposition of energy by positrons arising from the higher ^{56}Co mass fraction in the inner region (see Figure 22).

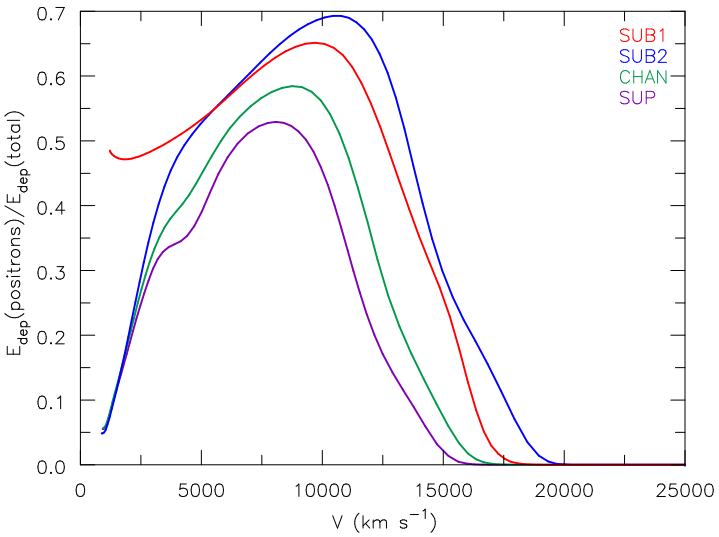

Figure 22 Ratio of the locally deposited energy from positrons (mainly from ^{56}Co) to the energy deposited by nuclear decays in the ejecta at about 216 days post-explosion. SUB1 shows a much higher ratio shortward of 5000 km s^{-1} due to the lack of a '^{56}Ni hole' and higher ^{56}Ni production in the core. This leads to higher ionization and a higher temperature in the inner region (in combination with lower densities) compared to other models.

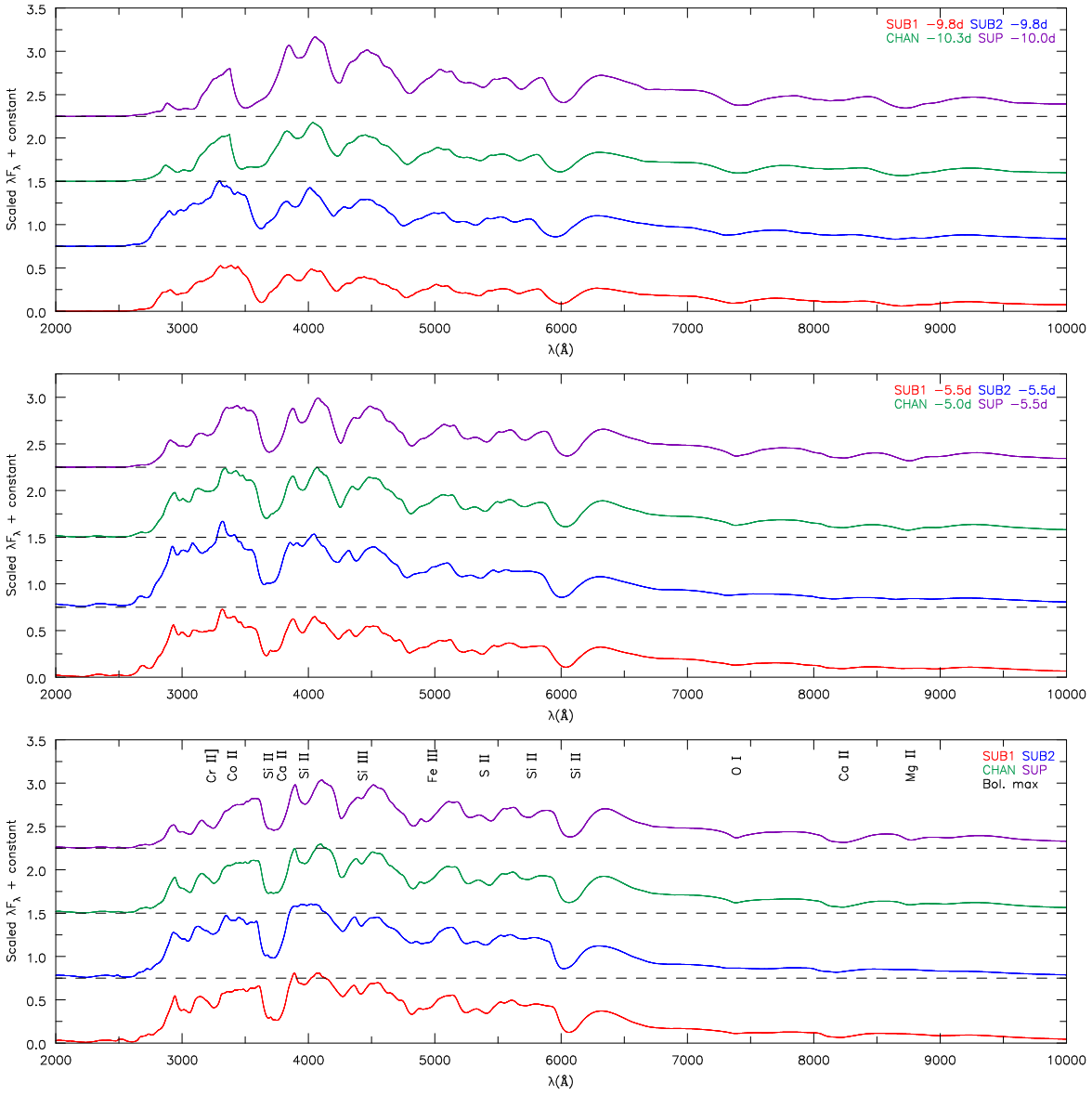

Figure 23 Spectral comparisons between models in the pre-maximum (−10 and −5 days relative to bolometric maximum) and bolometric maximum plotted in λF_λ vs. λ in order to contrast the NIR tail of the spectrum. All models have been scaled by the same factor, and we have added an offset to allow spectra to be more easily distinguished. See section 3.4 for details.

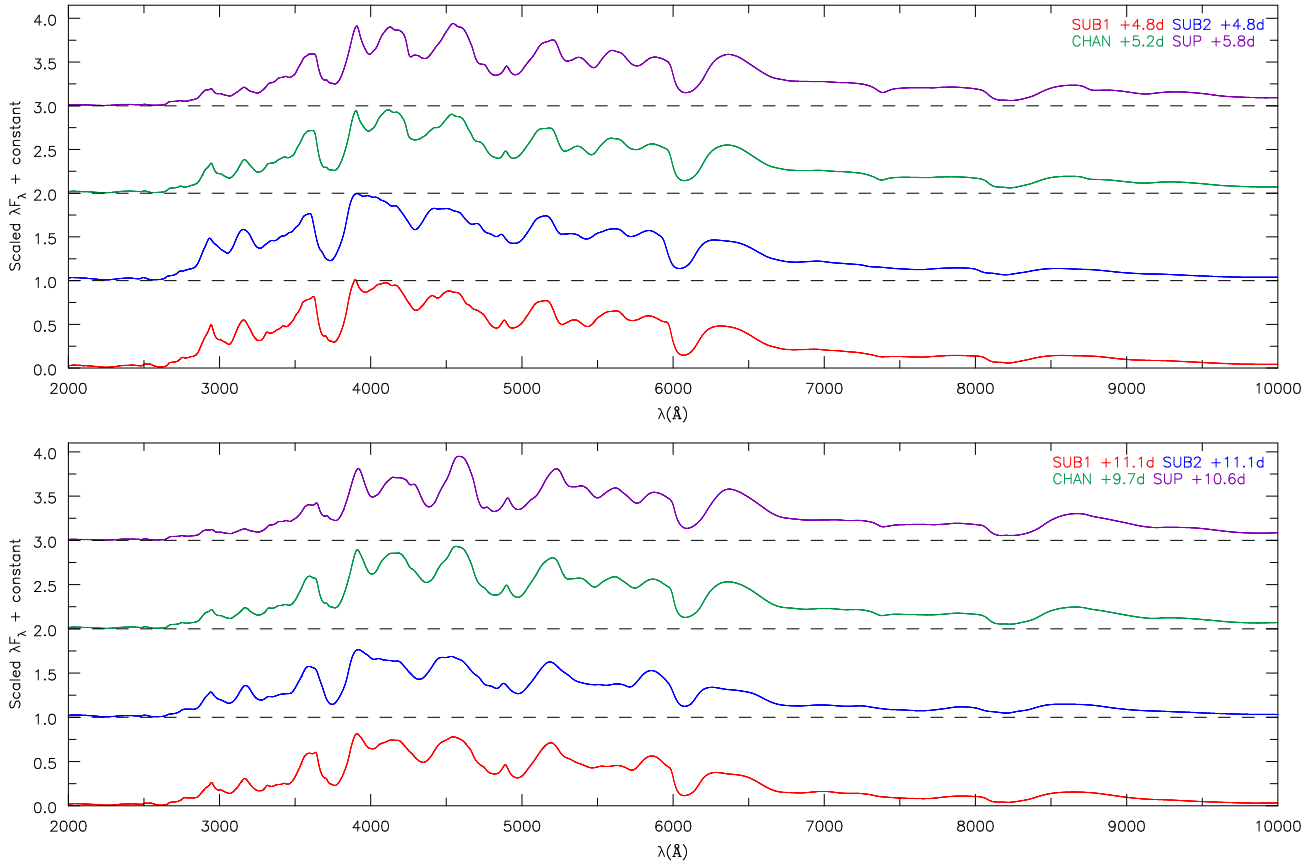

Figure 24 Spectral comparisons between models in the post-maximum phases (+5 and +10 days) relative to bolometric maximum plotted in λF_λ vs. λ space in order to contrast the NIR tail of the spectrum. In each plot, all models have been scaled by the same value, and we have added a multiple of the offset to more easily distinguish the models. The optical spectra is again similar showing still the strong Si II doublet at ∼6100 Å. The UV spectrum shows stronger blanketing in higher mass models. The strength of the Ca II NIR triplet deviates between the models, showing stronger absorption/emission in the cooler (higher mass) models.

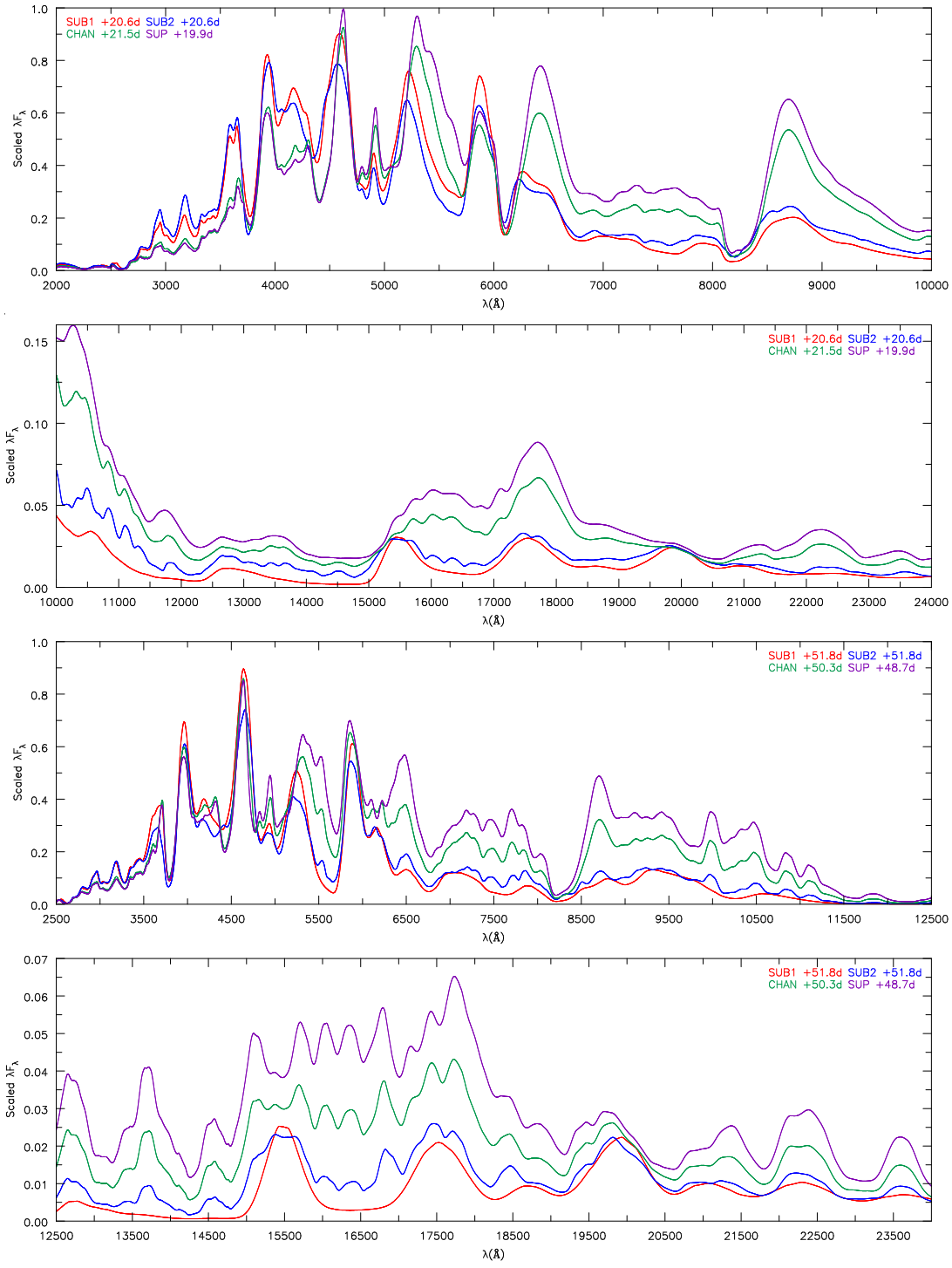

Figure 25 Spectral comparisons between models in the post-maximum phases at roughly +20 and +50 days relative to bolometric maximum. Each separate plot shows spectra scaled by the same value. See section 3.4.2.2 for details.

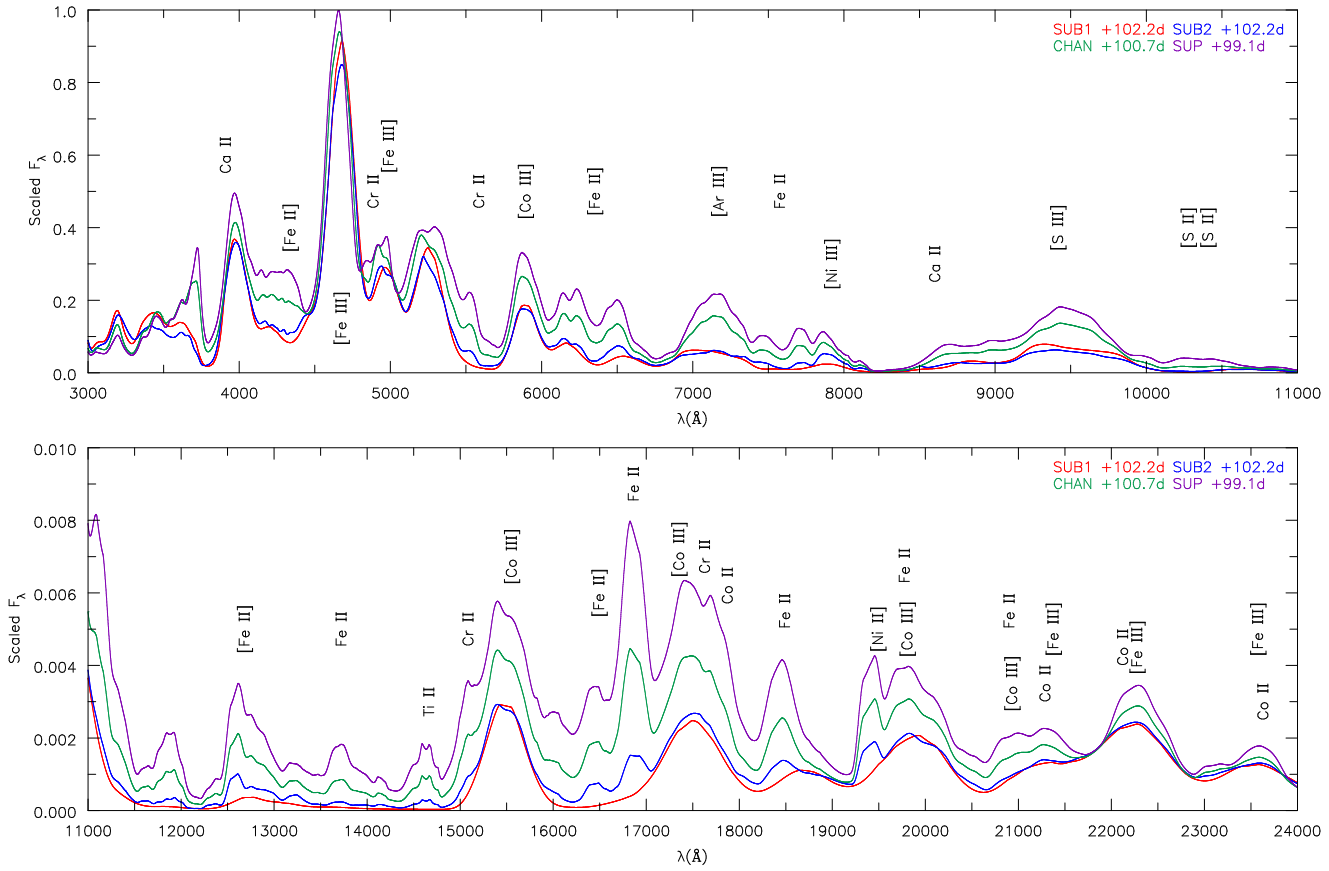

Figure 26 Spectral comparison between models in the nebular phase at roughly +100 days after bolometric maximum. We have scaled all models by the same value, and plot F_λ vs. λ. All models exhibit roughly the same amount of emission in the [Fe III] λ4658 line, but show substantial flux differences in the NIR. Unlike the other models, SUB1 lacks NIR Fe II and Co II features. Emission lines of [S III] $\lambda\lambda$9068, 9530, and [Ar III] $\lambda\lambda$7135, 7751 are present, and increase in strength relative to [Fe III] λ4658 as the ejecta mass, and equivalently, as the mass of IMEs, increases.

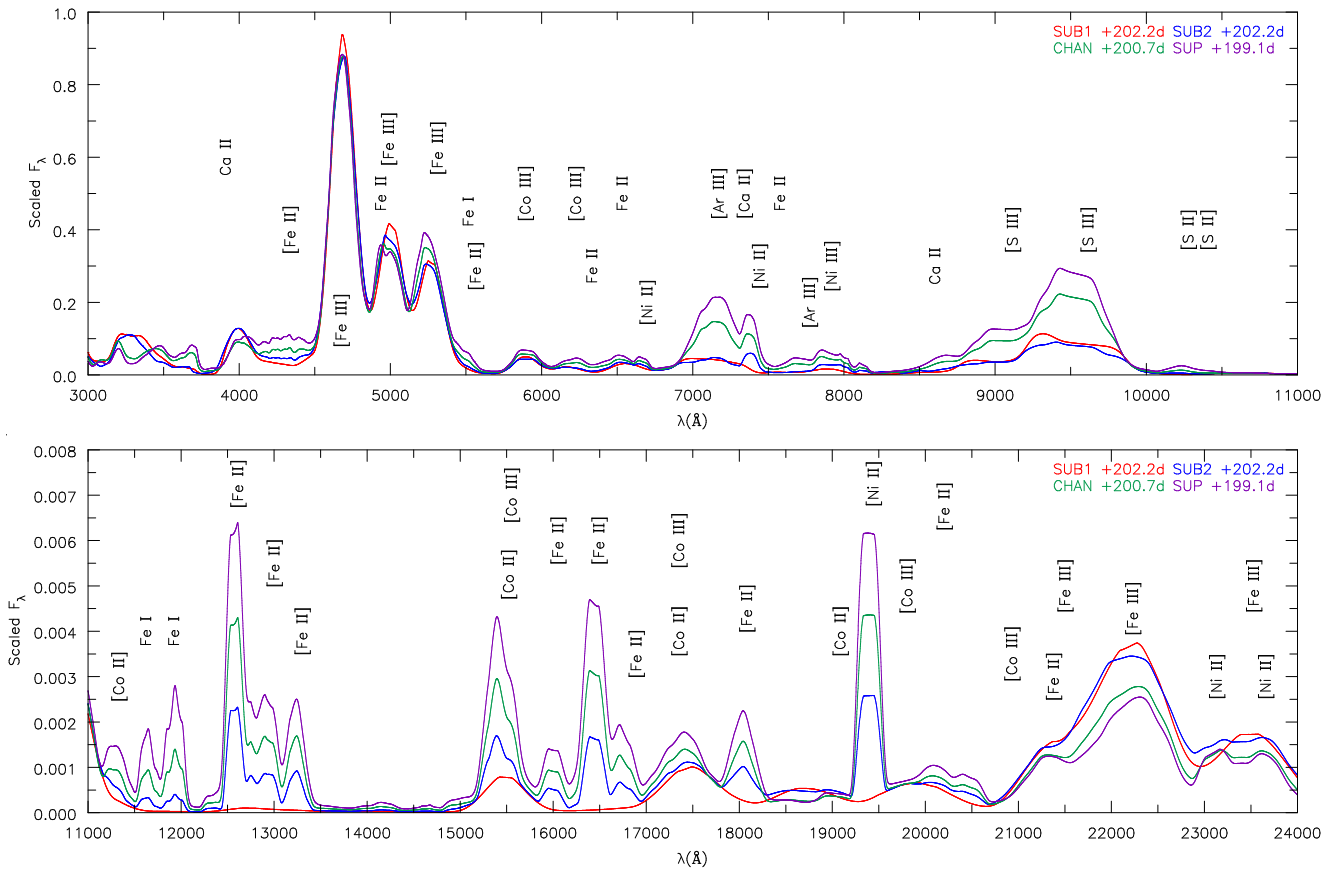

Figure 27 Spectral comparison between models in the nebular phase at roughly +200 days after bolometric maximum. We have scaled all models by the same value, and plot F_λ vs. λ. As at 100 days, SUB1 shows no prominent [Fe II] or [Co II] lines. Further, spectra of SUB1 in the J and H bands are now substantially different from those of SUB2. The [S III] $\lambda\lambda$9068, 9530 and the [Ar III] $\lambda\lambda$7135, 7751 features have increased in strength relative to [Fe III] λ4658. The broad emission feature covering 7000 through 7500 Å is a blend of [Ar III] λ7135, [Ni II] λ7378, and [Ca II] $\lambda\lambda$7291, 7324.

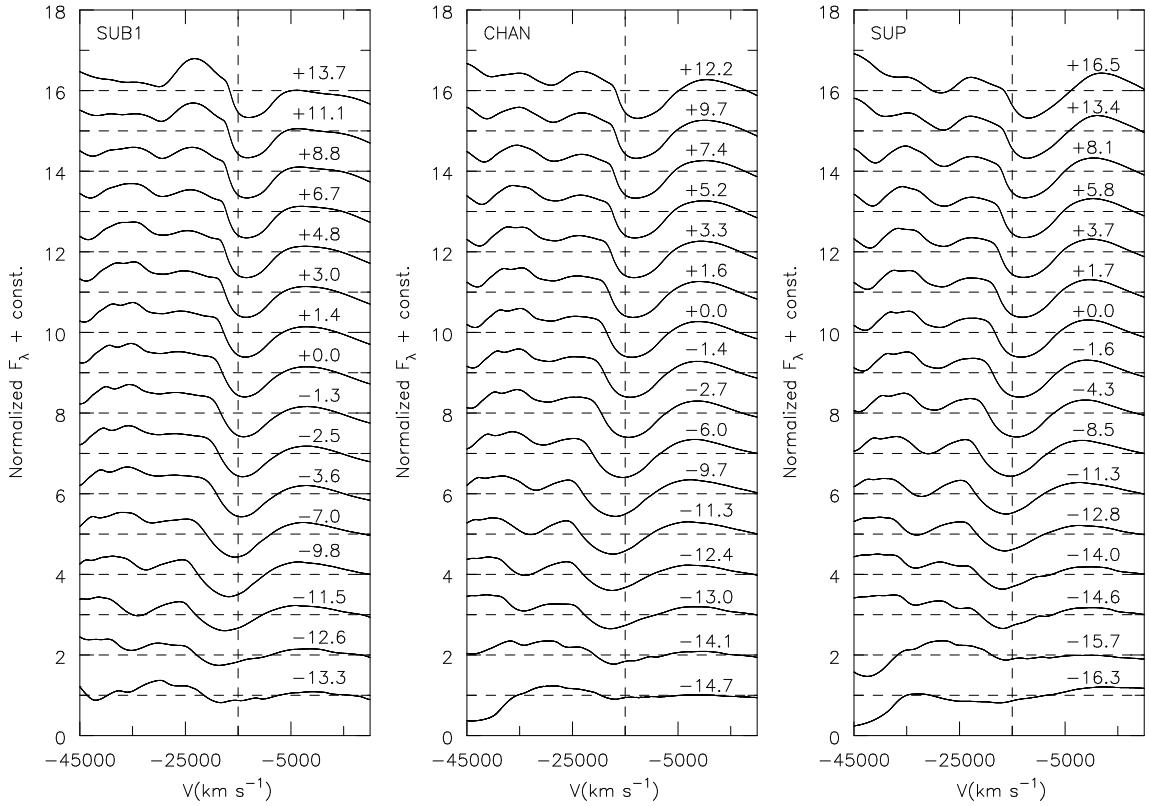

Figure 28 Normalized flux (according to Eqn. 3.1 between 5800-6500 Å) of the Si II λ6347, 6371 doublet relative to bolometric maximum plotted in velocity space shifted relative to λ6355. Note the lack of Si II HVFs. A vertical line at $-15\,000$ km s^{-1} is included as a reference.

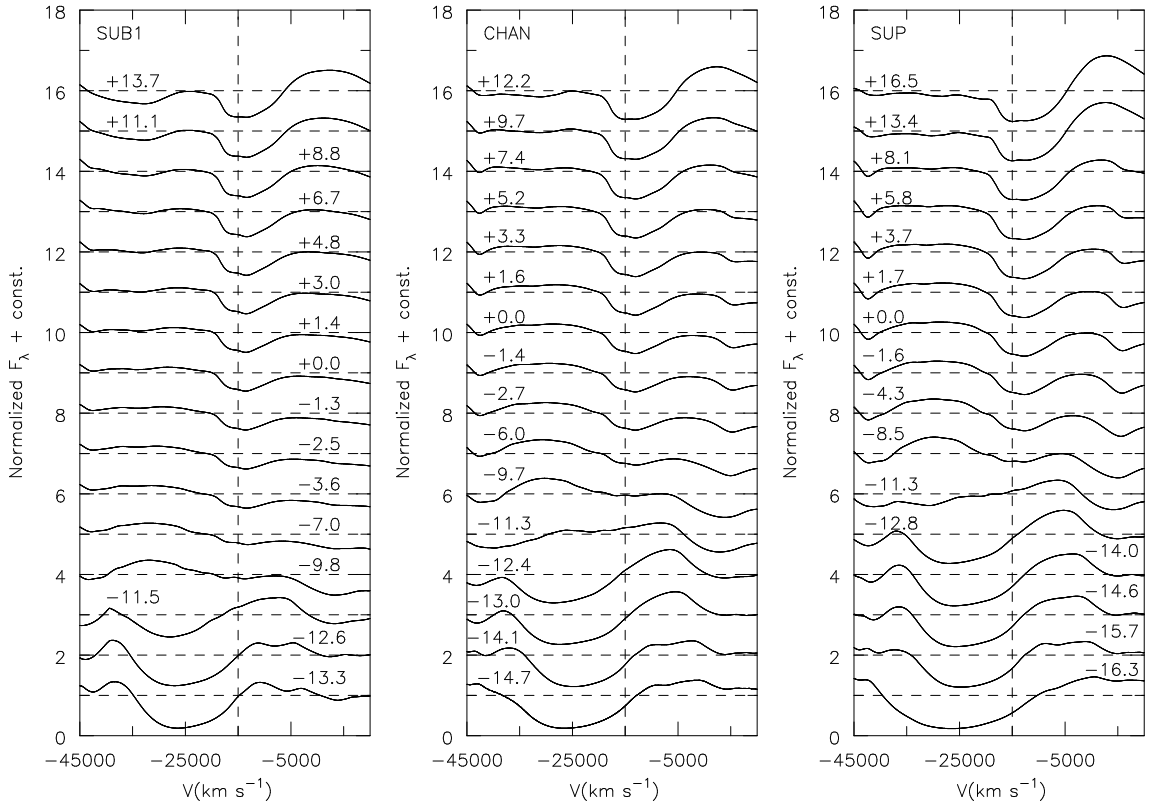

Figure 29 Normalized flux (according to Eqn. 3.1 between 7000-9000 Å) of the Ca II triplet relative to bolometric maximum plotted in velocity space shifted relative to λ8662. Note prior to $\lesssim -11$ days, HVFs are present without a photospheric component. After the HVF disappears, the photospheric component becomes visible. A vertical line at $-15\,000$ km s^{-1} is included as a reference.

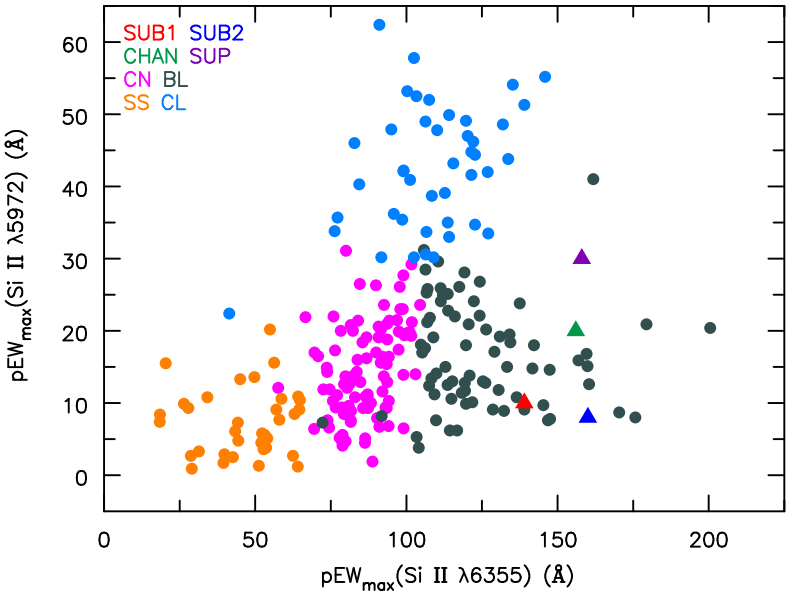

Figure 30 Plot of the pEWs of the Si II λ6355 and λ5972 features along with the data from Blondin et al. (2012). CN, BL, SS, and CL correspond to "core normal", "broad line", "shallow silicon", and "cool" classifications defined by Branch et al. (2006). Our models lie clustered near the BL classification.

Model	Si II λ5750	Si II λ6100	O I λ7400	Mg II λ8700
SUB1	10	139	17	$\lesssim 1$
SUB2	8	160	9	~ 1
CHAN	20	156	32	32
SUP	30	158	50	53

Table 5 Approximate pEW (Å) based on a straight line across the profile of the absorption feature.

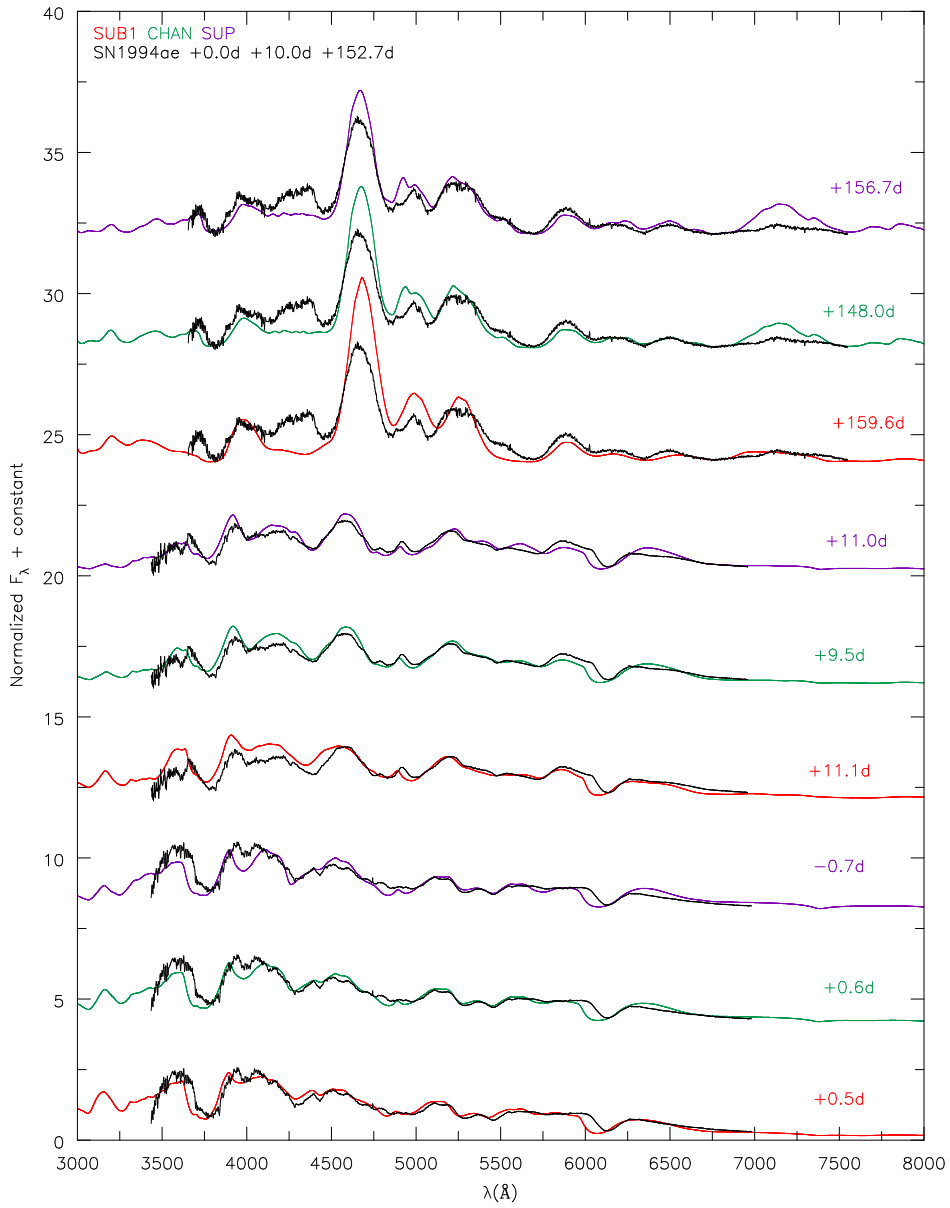

Figure 31 SN1994ae compared to our models at epochs +0.0, +10.0, and +152.7 days relative to B-band maximum, which occurred on MJD 49685.5. For comparison, we reddened our models using $E(B-V) = 0.0226$ mag and $R_V = 3.1$ (Jha et al., 2007). All fluxes have been normalized between 4000-7000 Å according to Eqn. 3.1. The observational data was taken from public CfA data https://www.CfA.harvard.edu/supernova/SNarchive.html. See section 3.6.2.1 for details.

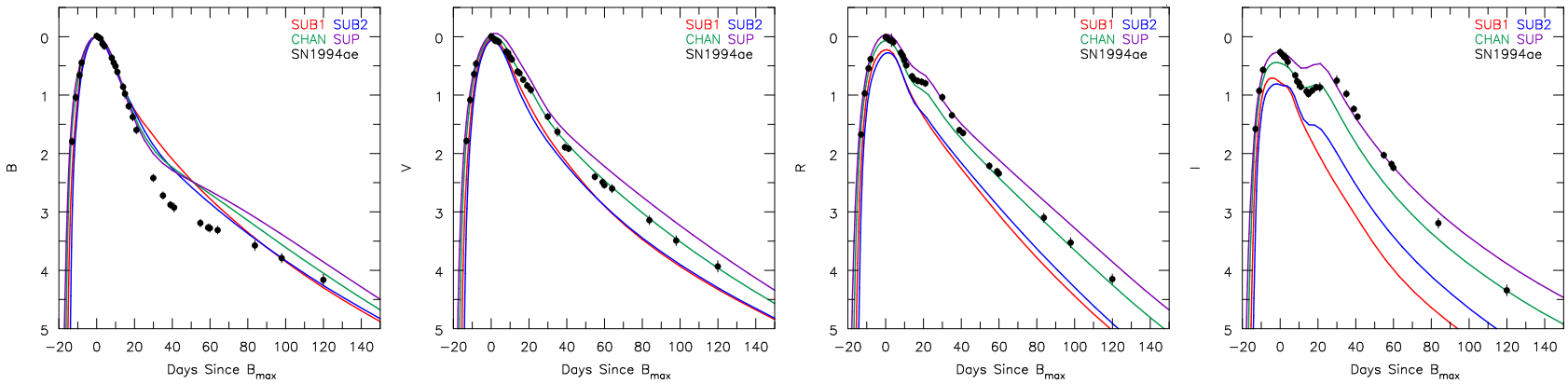

Figure 32 SN1994ae multi-band LCs normalized to $B_{\max}$ and corrected for reddening (see section 3.6.2.1). Our B-band LC agrees until 20 days post maximum. Afterwards, our LCs show roughly half a magnitude more flux. The V/R-band LC agrees with our model CHAN. Our models disagree with observations in the location of the I-band's second peak and more so for models with lower ejecta mass. Archived light curve photometry is taken from Open Supernova Catalog (Guillochon et al., 2017), with references from the CfA Supernova Archive (https://www.CfA.harvard.edu/supernova/SNarchive.html) and Riess et al. (2005).

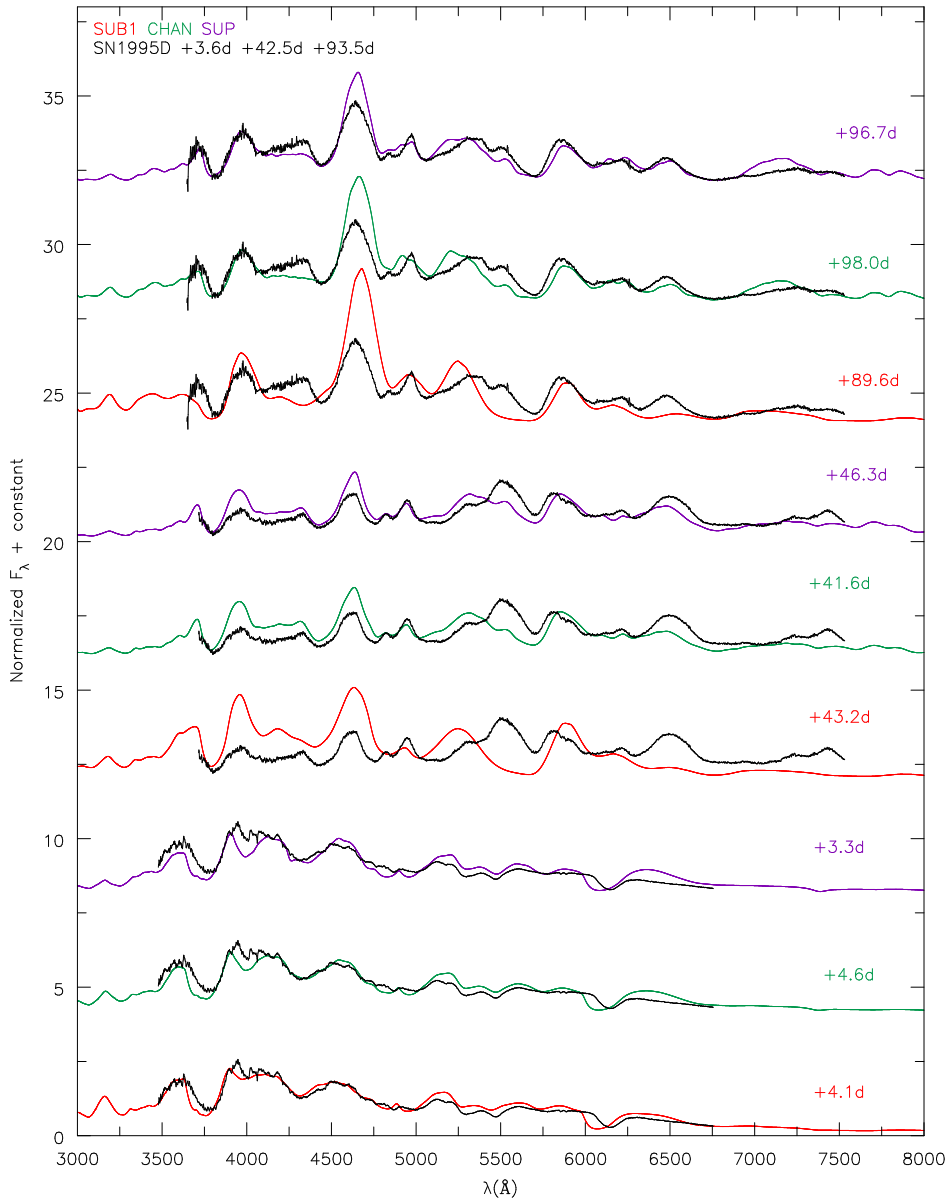

Figure 33 SN1995D compared to models at times +3.6, +42.5 and +93.5 days relative to B-band maximum which occurred on MJD 49768.7. We have corrected for redshift with a value of 0.0067. We reddened the models with $E(B-V)$=0.026 mag and R_V=3.1. All fluxes have been normalized between 4000-7000 Å according to Eqn. 3.1. The observational data was taken from public CfA data https://www.CfA.harvard.edu/supernova/SNarchive.html. See section 3.6.2.2 for details.

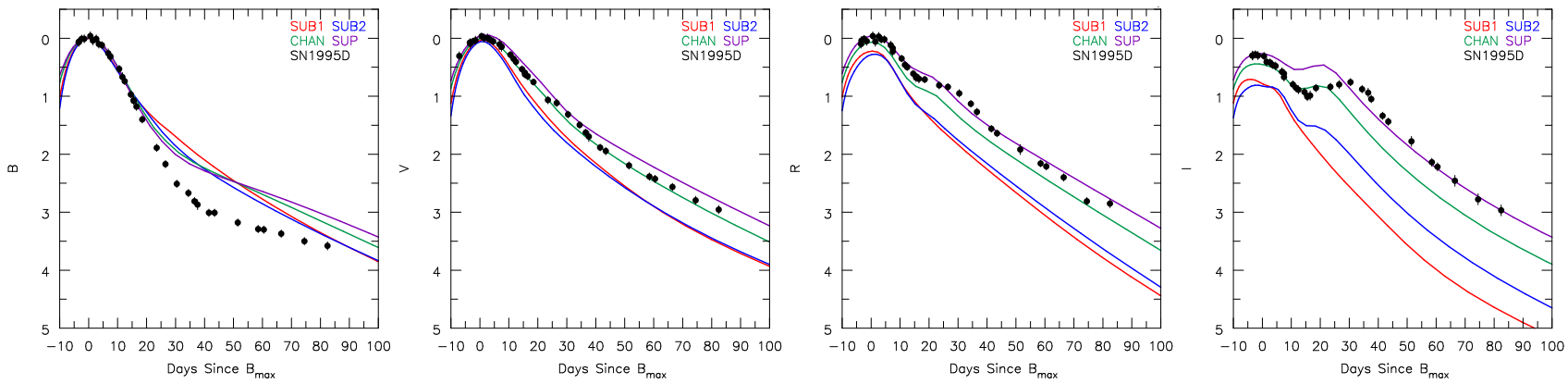

Figure 34 SN1995D multi-band LCs normalized to $B_{\max}$ and corrected for reddening (see section 3.6.2.2). B-band LC agrees until ∼12 days post maximum. Afterwards, our LCs show roughly half a magnitude more flux. The V/R-band LCs qualitatively agree with our CHAN model although our models fail to reproduce the second peak in the I-band. However, model SUP agrees with the observational data at late times. Archived light curve photometry is taken from Open Supernova Catalog (Guillochon et al., 2017), with references from CfA Supernova Archive https://www.CfA.harvard.edu/supernova/SNarchive.html and Riess et al. (1999).

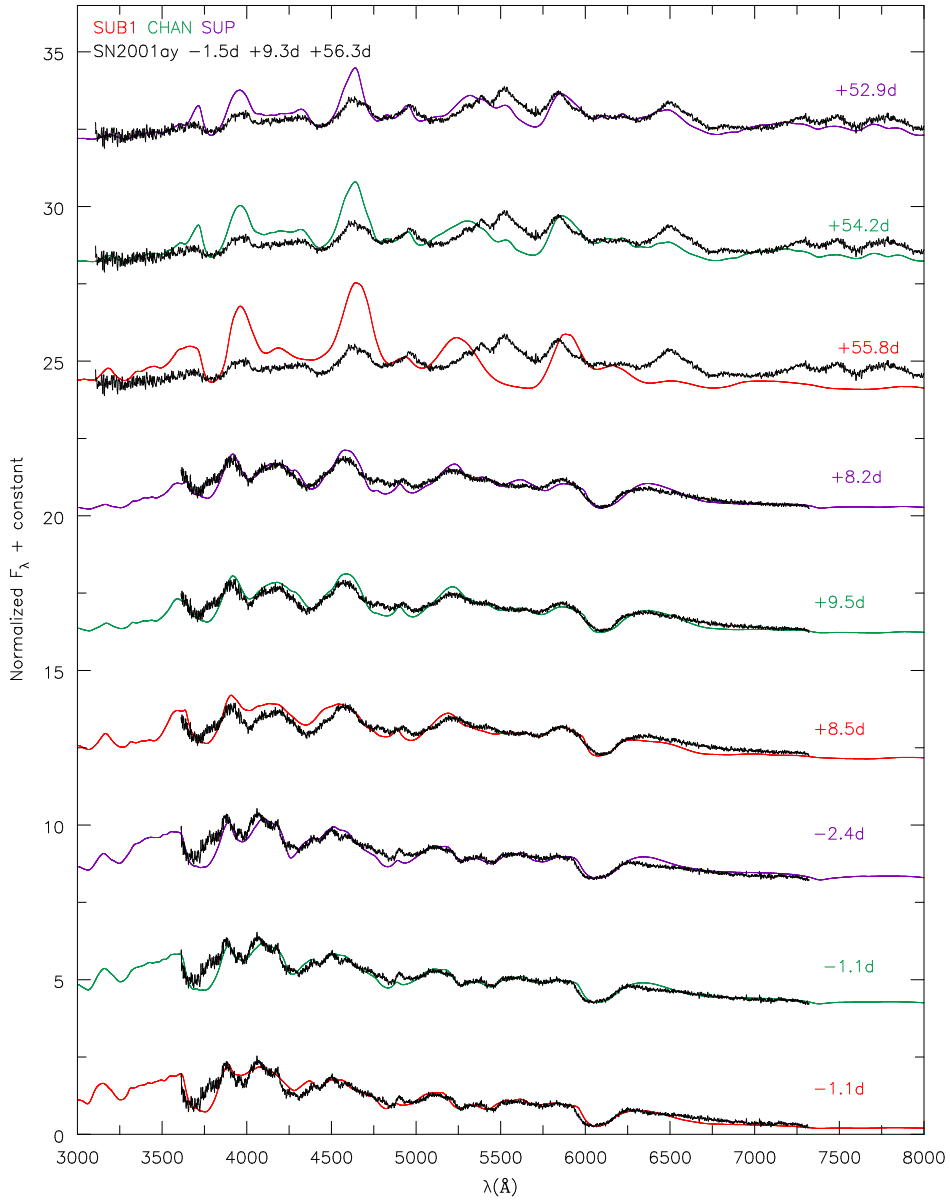

Figure 35 SN2001ay compared to models at epochs −1.5, +9.3, and +56.3 days relative to B-band maximum. Observed spectra have been corrected for a redshift of $z = 0.0302$. Models are reddened using $E(B-V)_{MW}$=0.026 mag, $E(B-V)_{\rm host}$=0.072 mag, and R_V=3.1. All fluxes are normalized in the range of 4000-7000 Å according to Eqn. 3.1. Observational data was taken from public CfA data https://www.CfA.harvard.edu/supernova/SNarchive.html. See section 3.6.2.3 for details.

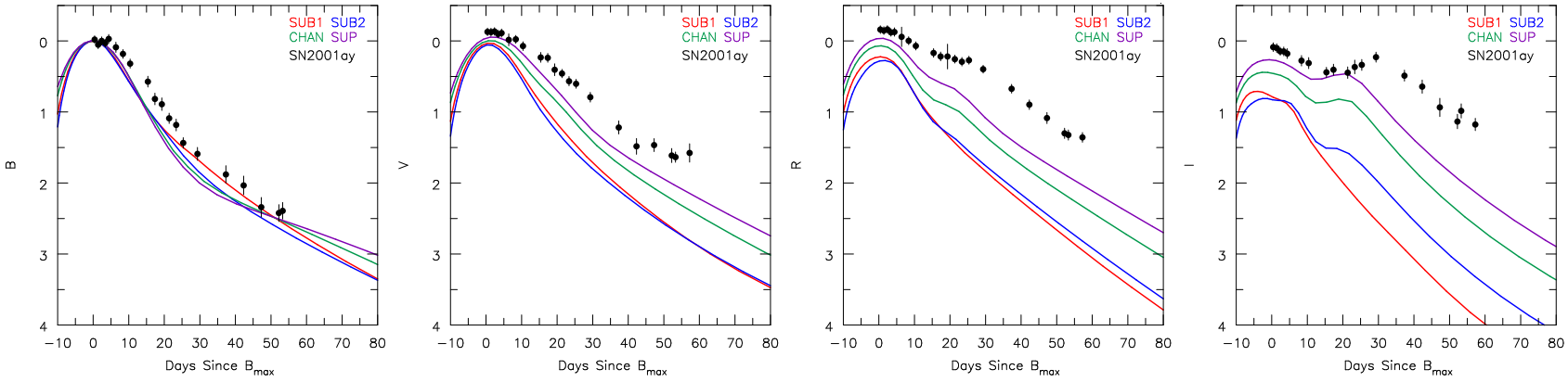

Figure 36 Multi-band LCs for SN2001ay normalized to $B_{\max}$ and corrected for reddening (see section 3.6.2.3). Our models fail to reproduce the post maximum decline except for U/B-bands. Models show too little $V/R/I$ flux in the decline post maximum. However, the peak flux ratio between bands matches to model SUP. A larger reddening and an adjustment of the time of B-band maximum would improve the comparison. Archived light curve photometry is taken from Open Supernova Catalog (Guillochon et al., 2017), with references from Ganeshalingam et al. (2010), and Silverman et al. (2012).

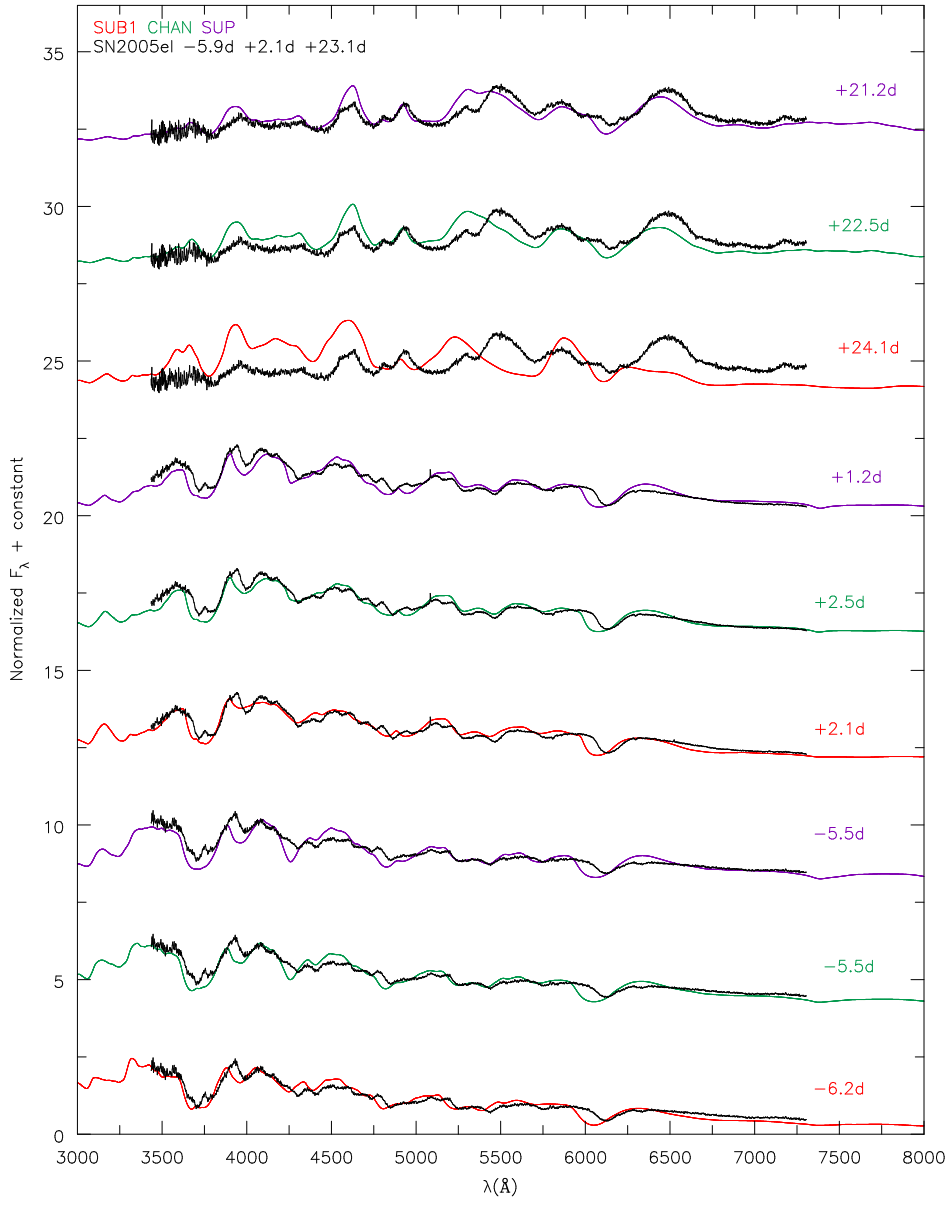

Figure 37 SN2005el compared to models at times −5.9, −4.9, and +23.1 days relative to B-band maximum. Observed spectrum is corrected for a redshift of 0.0148. Models are reddened with $E(B-V)$=0.136 mag and R_V=3.1. All fluxes are normalized between 4000-7000 Å according to Eqn. 3.1. This observational data was taken from public CfA data https://www.CfA.harvard.edu/supernova/SNarchive.html. See section 3.6.2.4 for details.

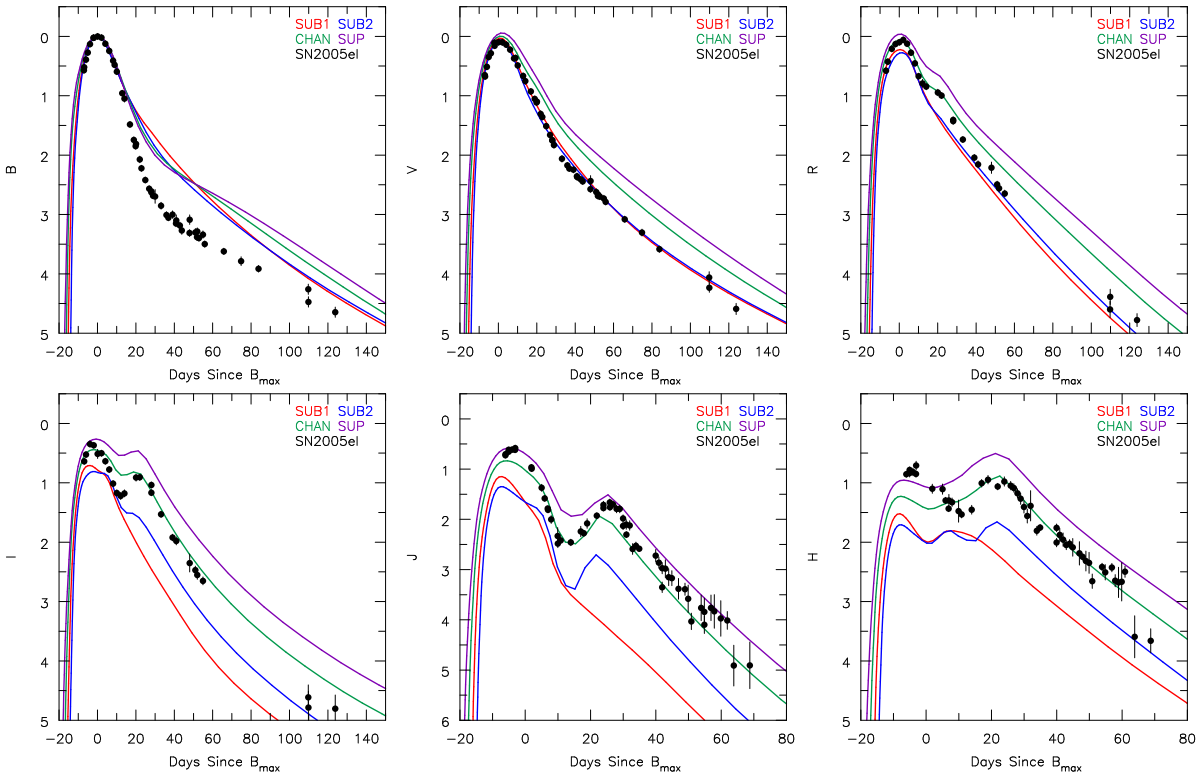

Figure 38 Multi-band LCs corrected for reddening and normalized to $B_{\max}$ (see section 3.6.2.4). Optical band normalized LCs of SN2005el agree in morphology with our SUB models. The NIR LCs do not agree with SUB models. Instead, the NIR LCs show better agreement with CHAN and SUP. Archived light curve photometry is taken from Open Supernova Catalog (Guillochon et al., 2017), with references from Contreras et al. (2010); Ganeshalingam et al. (2010); Silverman et al. (2012); Friedman et al. (2015).

4 UNDERSTANDING NEBULAR SPECTRA OF TYPE IA SUPERNOVAE

4.1 INTRODUCTION

The general consensus is that Type Ia supernovae (SNe Ia) are thermonuclear explosions of carbon-oxygen (C/O) white dwarfs (WDs) (Hoyle & Fowler, 1960). Whether this explosion is the result of a system of one WD and a non-degenerate star (known as the single degenerate (SD) channel) or via a system of two WDs (known as the double degenerate (DD) channel) remains uncertain.

SNe Ia come from compact WDs and cool quickly via adiabatic expansion, and without an additional energy supply, they would be extremely difficult to detect. What powers the observed luminosity of SNe Ia is the decay of radioactive material produced during the explosion. The main radioactive isotope produced is ^{56}Ni, whose decay chain is ^{56}Ni$\rightarrow^{56}$Co$\rightarrow^{56}$Fe, releasing 1.72 and 3.75 MeV for each part of the decay chain. Therefore, the production of ^{56}Ni is important in powering the luminosity of SNe Ia. However, the nickel yields (both stable and unstable) in SNe Ia are sensitive to both progenitor mass (ρ_c) and explosion scenario.

In 1D explosion modeling, higher central densities lead to enhanced electron capture and thus a larger neutron excess. As a consequence, more stable nickel (^{58}Ni, ^{60}Ni, and ^{62}Ni) is produced (Nomoto, 1984; Khokhlov, 1991a,b). Sub-M_{Ch} WDs have lower central densities, and 1D modeling of SNe Ia from sub-M_{Ch} progenitors shows a lower abundance of ^{58}Ni and ^{60}Ni compared to M_{Ch} SNe Ia. However, 3D DDT modeling does not produce a ^{56}Ni hole. Instead, the abundance of both ^{56}Ni and ^{58}Ni extend from the lowest velocities to about 10 000 km s^{-1} (Kasen et al., 2009; Seitenzahl et al., 2013). This result arises because they ignite the WD from the center. If you ignite from the surface, as in a double

detonation, the burning front moves in and there is no mixing of stable Ni outwards (Woosley & Weaver, 1994; Livne & Arnett, 1995; Fink et al., 2007, 2010). Overall, the 3D simulations of WD explosions are very artificial, and the outcome depends strongly on number of ignition points and distribution. Despite the time-scale for gravitational settling being $\sim 10^9 - 10^{10}$ yrs (Bildsten & Hall, 2001), ^{22}Ne settling in sub-M_{Ch} is proposed as a way to enhance the neutronization. Therefore, nebular nickel and IGE spectral features may constrain the physics of SNe Ia (Woosley, 1997; Iwamoto et al., 1999; Stehle et al., 2005; Mazzali & Podsiadlowski, 2006; Gerardy et al., 2007; Maeda et al., 2010b; Mazzali et al., 2011; Mazzali & Hachinger, 2012; Mazzali et al., 2015).

Without knowing the progenitor system and explosion scenario, we fundamentally cannot accurately predict (despite understanding flame physics) the amount of stable nickel produced, the overall abundances of IMEs, nor where in the ejecta these IMEs are produced relative to the original ^{56}Ni. However, studying nebular spectra will allow us to estimate these properties. At nebular times any nickel emission features are due to the remaining stable nickel, particularly from ^{58}Ni and ^{60}Ni. Since the width of any observed nebular feature is influenced by emission over the velocities at which the species exist, stable nickel features will help constrain the presence of the ^{56}Ni hole (irrespective of the model).

Nebular spectra are great tools to understand progenitors of SNe Ia. At this time, the ejecta is optically thin to continuum and most lines (with exceptions such as UV transitions), and much of the spectra comes from the inner part of the ejecta ($\lesssim 8000$ km s^{-1}), where the densities are highest and iron is the most abundant species. Because iron is most abundant in this region at nebular times, optical spectra are dominated by Fe II and Fe III lines and exhibit little to no flux from IME species such as S III and Ar III. The [Ca II] $\lambda\lambda$7291, 7324 may be blended with the [Fe II] $\lambda\lambda$7155, 7172, 7388 triplet, so its presence is difficult to determine.

Numerous previous studies have investigated nebular spectra (Houck & Fransson, 1992; Ruiz-Lapuente et al., 1992, 1995; Smareglia & Mazzali, 1997; Mazzali et al., 1998; Gerardy, 2002; Kozma et al., 2005; Maeda et al., 2010a; Blondin et al., 2012; Taubenberger et al., 2013a; Mazzali et al., 2015; Black et al., 2016; Botyánszki & Kasen, 2017; Graham et al., 2017; Maguire et al., 2018; Black, 2018; Diamond et al., 2018; Black et al., 2018).

Authors often study emission lines by fitting Gaussian profiles to features that may or may not be blended. Maguire et al. (2018), for instance, fit Gaussian profiles to emission lines, and assumes the levels are in LTE with respect to the ground state. These authors also try and fit the complicated feature around 7300 Å without knowing the possible contribution from [Ca II] $\lambda\lambda$7291, 7324. Work by Taubenberger et al. (2013a) utilised nebular spectra to understand the emission from [O I] $\lambda\lambda$6300, 6364 in the subluminous SN2010p (SN1991bg-like). These authors argued for a non-spherical distribution of oxygen located close to the core to produce these features.

Ruiz-Lapuente et al. (1995) struggled to obtain good model fits to nebular spectra despite their models matching the photospheric phase spectra. These authors also note the dominant form of iron is Fe^{2+}, with a sizable fraction of Fe^{+} that need not be coincident with Fe^{2+}. Ruiz-Lapuente et al. (1992) modeled spectra for distance determination by solving for the ionization structure, assuming collisional excitations dominate, and the energy loss is balanced by the thermalization of γ-rays and positrons from nuclear decays. These authors were able to fit some components (like the [Fe III] 4700 Å blend) to nebular spectra. Mazzali et al. (2015) also obtained good nebular spectral fits to SN2011fe with their 'ρ-11fe' model by means of abundance tomography. The authors claim that SN2011fe requires the innermost ejecta to be dominated by stable iron, which aids in cooling instead of heating (via radioactive decay) and rules out a low mass ($\sim$1.02 $M_{\odot}$) WD progenitor. Mazzali et al. (2018) also used abundance tomography to model the fast declining SNe Ia, SN2007bo and SN2011iv. By analyzing emission components of many [Fe II] and [Fe III] features, the authors reproduce the spectra by using a two component emission model (one blueshifted and one redshifted), which acts like two distinct nebulae. The authors do not rule out the possibility of an off-center ignition instead of two colliding WDs. In all of these works, however, the abundances and their distributions are free parameters.

Nebular modeling raises questions about the ionization/abundance structure of the "normal" SN Ia ejecta. Nebular modeling by Botyánszki & Kasen (2017) and Wilk et al. (2018) predicts strong emission lines of [S III] $\lambda\lambda$9069, 9531 (and [Ar III] λ71336, 7751 by Wilk et al. (2018)) in their ejecta mass models. Why are these emission lines largely absent or weak? What is the contribution of [Ca II] $\lambda\lambda$7291, 7324 to the observed 7300 Å feature?

What does it imply if IMEs are not seen in nebular spectra? Does this reflect the ionization structure or the abundances and/or chemical stratification? What causes the strength of the [Fe III] 4700 Å feature to be much stronger than other features beyond 5500 Å in models compared to observations (Botyánszki & Kasen, 2017; Wilk et al., 2018)?

The nebular model spectra of Wilk et al. (2018) indicate a higher ionization than what is generally observed. As clumping enhances the density, increases the recombination rate, and lowers the ionization, we introduce clumping in our nebular modeling of SNe Ia ejecta. Given the high ionization of SUB1 at nebular times (because the lack of a "^{56}Ni hole" facilitates more heating of the inner region), clumping is a natural choice given previous evidence of its role in reproducing spectral features (Chugai, 1992; Bowers et al., 1997; Thomas et al., 2002; Leonard et al., 2005; Leloudas et al., 2009; Srivastav et al., 2016; Porter et al., 2016). Previous theoretical modeling suggests clumping to be a byproduct of "nickel bubbles," an expansion of the iron and nickel regions relative to the surrounding material due to radioactive decay energy deposition (Woosley, 1988; Li et al., 1993; Basko, 1994; Wang, 2008), Rayleigh Taylor instabilities during DDT burning (Golombek & Niemeyer, 2005), or material interaction during detonation (Maier & Niemeyer, 2006).

In this chapter, we study the formation of nebular spectra and examine the influence of clumping. We highlight problems with the emission from IMEs and the ionization structure by examining the influence of clumping. In this study, we use models SUB1 and CHAN from Wilk et al. (2018). In section 4.2 we discuss our technique for introducing clumping in our models. In section 4.3 we present the impact of clumping on nebular SN Ia spectra. We highlight the changes to the ionization structure in section 4.3.2. Shifts in ionization are reflected in some species, so in sections 4.3.3, 4.3.4, and 4.3.5 we discuss the effects on iron features, nickel features, and IMEs respectively. Finally, we summarize our work in section 4.4.

4.2 TECHNIQUE

This research uses two hydrodynamic models of Wilk et al. (2018), DDC10 (CHAN) and SCH5p5 (SUB1). DDC10 is a M_{Ch} (1.40 $M_{\odot}$) model from Blondin et al. (2013). Model SCH5p5 is a sub-M_{Ch} (1.04 $M_{\odot}$) from Blondin et al. (2017), but we have scaled the density by 0.98 (see Wilk et al., 2018). Both CHAN and SUB1 have the same ^{56}Ni at 0.62 $M_{\odot}$. We use CMFGEN to solve the spherically symmetric, time-dependent, relativistic radiative transfer equation allowing for non-local thermodynamic equilibrium (non-LTE) processes. We take these two models at 216.5 days post-explosion from Wilk et al. (2018). Table 6 lists the initial masses for each model as well as the mass abundance of calcium, iron, cobalt, ^{58}Ni plus ^{60}Ni, and ^{56}Ni. We see CHAN has more than a factor of two stable nickel – M(^{58}Ni) + M(^{60}Ni) – than SUB1 as well as almost a factor of two more calcium.

4.2.1 Numerical Treatment

Our original radiative-transfer calculations for our models did not include the effects of clumping. Therefore, to treat clumping in our models, we make some simple assumptions with CMFGEN. We assume there is no inter-clump media and the clumping is uniform in a homogeneous flow (i.e. $f(V) = f_{\circ}$ for all species and hydrodynamic velocities V). Assumptions underlying our clumping approach and discussions of the influence of clumping on core-collapse SNe II-P are provided by Dessart et al. (2018). Our treatment of clumping in CMFGEN differs from that of a concentric shell-type structure, which is susceptible to radiative transfer effects across a shell and requires a large number of depth points to resolve the shells.

The clumping factor scales many variables, such as densities (scaled by $1/f$) and the emissivities and opacities (calculated using populations derived from clumps then scaled by f). This micro-clumping formalism leaves the mass column density unchanged. CMFGEN has incorporated this clumping method since Hillier & Miller (1999) first applied it to massive stars.

At a time step of 216.5 d post explosion (∼+200 d post maximum) we resolved the

relativistic radiative transfer equation for our models SUB1 and CHAN using a clumping factor (f) of 0.33, 0.25, and 0.1 (a value motivated by modeling of Wolf-Rayet stars (Hillier & Miller, 1999)). Since the previous time-step was not computed using clumping in the models, we scaled the initial input populations by $1/f$ between successive ionizations. This simple scaling is adequate since time-dependent effects have a negligible influence on the spectrum.

4.3 RESULTS

Figures 39 and 40 show the synthetic optical and near infrared (NIR) spectra of SUB1 and CHAN for the different values of a clumping factor (f = 1.00, 0.33, 0.25, and 0.10). In order to contrast the little amount of flux in the NIR, we show log F_λ vs. λ for wavelengths 1.0–2.4 μm. We also show the component spectrum for $f = 0.10$ and $f = 0.33$ for models SUB1 and CHAN in Figures 41, 42, 43, and 44.

4.3.1 Unclumped Models

Before we discuss clumping, it is necessary to understand and summarize the results of Wilk et al. (2018) that do not incorporate clumping. This chapter focuses on two ejecta models, a direct detonation of a sub-M_{Ch} WD and a DDT WD explosion model. Because our models come from two different explosion scenarios, the nucleosynthesis yields and stratification are model dependent. In 1D simulations of DDT explosions in M_{Ch} WDs produce what is known as a "^{56}Ni hole," which is an underabundance of ^{56}Ni in the innermost region. This arises due to neutron-rich nuclear statistical equilibrium (NSE) burning. Since our SUB1 model has lower central densities during explosion, it does not have a "^{56}Ni hole." Therefore, SUB1 has a factor of about 2.26 less stable nickel. Within the "^{56}Ni hole" of CHAN, the temperature and ionization is lower than in the region containing the original ^{56}Ni.

Since stable nickel is centralized to the innermost part of the ejecta, it only becomes visible as the photosphere recedes inwards and becomes optically thin, and hence the ejecta

transitions into the nebular phase. Thus, nebular spectra allow us to probe this once shielded inner region. At 216 days post explosion (roughly +200 days post maximum), we do not see stable nickel in our SUB1 model, unlike in model CHAN. SUB1 has very little stable nickel in the inner region and also has Ni^{2+} as its dominant ionization (see Figure 21). At nebular times we expect to see forbidden [Ni II] lines, particularly [Ni II] $\lambda\lambda$7378, 7412 and [Ni II] 1.939 μm, which are present in CHAN. Both models show strong emission from higher ionization states like Fe^{2+}, Co^{2+}, Ar^{2+}, and S^{2+}.

At nebular times, the energy deposited by radioactive decay is the energy radiated by the gas by numerous cooling lines. In the unclumped models, radioactive decay heats both the IGEs as well as the IMEs. However, it is necessary to determine if these ejecta models will still show spectral signatures of IMEs when clumping is introduced.

4.3.2 Ionization Shifts

We show the average charge per species for sulfur, argon, calcium, iron, cobalt, and nickel for models with different amounts of clumping in Figures 45 and 46. As expected, clumping shifts the ionization downward in both models for the IGEs from mostly doubly ionized to singly ionized (i.e. $Fe^{2+} \rightarrow Fe^{+}$). The strength of Fe III, Co III, Ni III, S III, and Ar III lines decreases considerably with increasing clumping, while Fe II and Co II lines increase. For both SUB1 and CHAN, the average charge of sulfur, argon, and cobalt differs by almost one electron between $f = 1.00$ and $f = 0.10$ in the inner ejecta regions.

4.3.3 Impact on Iron Lines

Figures 39 and 40, show that the Fe I, Fe II, and Fe III optical features changed significantly. The [Fe III] $\lambda\lambda$4658, 4702 feature dropped in flux by more than a factor of two in both ejecta models from $f = 1.00$ to $f = 0.10$, while we saw the emergence of Fe I features between 4100–4500 Å and between 5400–5600 Å (z $^5D^o_J$ – a $^5F_{J'}$ optical transitions). Figures 39 and 40 show the Fe I emission as a shoulder to the neighboring [Fe III] and [Fe II] emission for f =0.33 and 0.25, while we see a noticeable peak for $f = 0.10$.

While Fe II features were generally enhanced, the expected Fe II feature around

4359 Å (believed to be the $a^6S_{5/2} - a^6D_{7/2}$ transition and similarly the $a^6S_{5/2} - a^6D_{9/2}$ transition at 4287 Å) is weak or absent in our models compared with observations. An examination of the individual Fe I, Fe II, and Fe III spectra showed that the optical depth effects are very important. It appears that the emergence of partially thick Fe I lines, Ti II lines like 4395 Å, and permitted Fe II lines reduce the strength of the claimed [Fe II] $\lambda\lambda$4287, 4359 doublet believed to be seen in nebular spectra.

In Figures 47, 48, and 49 we show the optical depth to the [Fe II] λ4359 resonance zone (at velocity V) arising from interactions with other lines along the line of sight. There are tens of interacting lines to the outer ejecta and ∼25 000 interacting lines to the inner ejecta. Figures 47 and 48 show this optical depth (and the continuum optical depth) along a core ray through the ejecta. The line transitions with the largest optical depth contributions are Fe I] λ4384, Fe I] λ4375, Ti II λ4395, Fe II λ4385, and Fe I] λ4404. Differences between models and levels of clumping reflect the differences in the ionization of iron since the largest contributions to the optical depth primarily come from iron lines. Figure 49 shows this optical depth along various rays parallel to the z-axis towards the observer (V_y and V_z). In both models, [Fe II] λ4359 reaches an optical depth of unity at roughly 10 000 km s^{-1} for a clumping factor of 0.10. In model CHAN, the Sobolev line optical depth reaches unity around 5 000 km s^{-1} for $f = 0.33$, while for model SUB1 it is true around 2500 km s^{-1}. Figures 39 and 40 highlight how little flux is seen below 4500 Å.

Studies of SN Ia nebular spectra often investigate the [Fe II] feature around 12 600 Å (Maguire et al., 2018; Diamond et al., 2018) since it is the least blended feature in nebular SN Ia spectra (free from other lines and ionization states of Fe). Our models confirm it is "blend"-free. This line complex is therefore the best feature to constrain the Fe II emitting region. We show in Figure 50 that this [Fe II] feature can be reproduced by calculating an emission spectrum. To produce this emission spectrum, we use the temperature and ionization structure from CMFGEN and re-solve the level populations considering only collisional processes and radiative decays. The relativistic radiative transfer equation is then solved assuming zero opacity. We show this line complex can be inferred from tomography, as it is only sensitive to the temperature and ionization. However, this method will break down for departures from spherical symmetry.

Various observations of nebular SN Ia spectra show a slight shouldering on the 4600 Å iron complex due to a potential Fe I feature at 5500 Å – z $^5D^o_J$ – a $^5F_{J'}$ optical transitions – (Childress et al., 2015; Graham et al., 2017). Such Fe I features could constrain the level of ionization within SN ejecta and assist future modeling. Since Fe I features cause optical depth effects with [Fe II] λ4287, 4359, it is important to determine the Fe ionization. Despite all the observations showing [Fe II] λ4287, 4359, this feature has yet to be accurately modeled by other researchers (Spyromilio 2016, private communication; Sim 2016, private communication). Shifts in the ionization of iron ($Fe^{2+} \rightarrow Fe^{+} \rightarrow Fe$) are expected as the ejecta continuously expands and cools as less energy is deposited from radioactive decays (Fransson & Jerkstrand, 2015). Fransson & Jerkstrand (2015) showed that at very late times (1000 days), the 4600 Å iron complex, despite its similar appearance to early epochs, is dominated by emission from Fe I and Fe II.

4.3.4 [Ni II] 1.939 Microns

In SUB1 models, the ionization fraction for nickel (Ni^{+}/ Ni^{2+}) drops in the inner region ($\lesssim$ 5000 km s^{-1}) by roughly three orders of magnitude when changing $f = 1.00$ to $f = 0.10$. However, the [Ni II] 1.939 μm line is still absent in SUB1. Where the line formation occurs, below $\sim$6500 km s^{-1}, the electron density is higher than 10^7 cm^{-3} in the inner part of the ejecta, so its line emission scales linearly with density as we increase the amount of clumping. These densities are above the critical density for the upper level of this transition, so collisional de-excitations are important.

With $f = 0.10$ for SUB1, the weak [Ni II] 1.939 micron line is also a factor of a few weaker than [Co II] 1.9035 microns. SUB1 has more than a factor of 2 less stable nickel compared to CHAN (Table 6) in which we do still see the [Ni II] 1.939 micron line. With all of these factors such as ionization and abundance accounted for, it is not surprising that spectra of SUB1 still do not show this line.

4.3.5 IMEs

Due to the overlap in production/mixing of ^{56}Ni and IMEs in our models, the strengths of IMEs are sensitive to the non-thermal heating and ionization structure within the ejecta. Within our models, a consequence of clumping is the enhancement of the [Ca II] $\lambda\lambda$7291, 7324 doublet. The [Ca II] doublet is blended with the [Fe II] $\lambda\lambda$7155, 7172, 7388 triplet and [Ar III] λ7136, and it contributes a large portion of the flux to the blended feature (see Figures 41-44). The [Ca II] emission flux is model dependent. Not only is the mass of calcium $\sim$1.75 times larger in CHAN than SUB1 but also the distribution of calcium varies significantly between SUB1 and CHAN. In SUB1, the inner region containing 80 percent of the energy deposited only contains 25 percent of the calcium mass. In CHAN, however, the inner region containing 80 percent of the energy deposited contains 50 percent of the calcium mass. These models help constrain the amount of stratification between the original ^{56}Ni and IMEs required to produce SNe Ia nebular spectra.

Once the ionization is lowered, Ca^+ becomes the dominant cooling for the zone rich in IMEs, since S^+ and Ar^+, unlike their twice-ionized siblings, do not have strong cooling lines due to their low critical densities. We see the strength in the twice-ionized sulfur and argon lines ([S III] $\lambda\lambda$9068, 9530 and [Ar III] $\lambda\lambda$7135, 7751) decreases as we lower the clumping factor. However, it is unclear if such strong [Ca II] $\lambda\lambda$7291, 7324 emission is seen in spectra of classic SNe Ia blended into the feature around 7200 Å, which is thought to be mostly [Fe II] and [Ni II], in nebular spectra – Taubenberger et al. (2013b); Bikmaev et al. (2015); Graham et al. (2017); Maguire et al. (2018). For low luminosity 91bg-like SNe Ia (such as SN1999by), modeling suggests Ca emission is the dominant component of the 7200 Å feature at +180 days (Blondin et al., 2018).

If the 7200 Å feature is highly blended with [Ca II], then for a given electron density and temperature, we can predict emissivity per ion ratio of the [Ca II] doublet to the [Fe II] lines using some simple physical assumptions. Assuming only collisional processes and radiative decays, we can solve for the atomic level populations for a range of temperatures and electron densities. Figure 52 shows the emissivity ratio of the [Ca II] λ7291 transition to the [Fe II] λ7155 transition for a range of temperatures and electron densities with our simple

assumptions. As shown in Figure 52, for equal $N(\mathrm{Fe}^+)/N(\mathrm{Ca}^+) = 1$, the emissivity ratio between [Ca II] λ7291 and [Fe II] λ7155 for temperatures between 2000-7000 K and electron densities between 10^5-10^8 cm^{-3} is between a factor of 10-100. However, in our models, our $N(\mathrm{Fe}^+)/N(\mathrm{Ca}^+)$ is $\sim$5-30 between 5 000-10 000 km s^{-1}. Therefore, we expect to see [Ca II] $\lambda\lambda$7291, 7324 emission blended as long as the $N(\mathrm{Fe}^+)/N(\mathrm{Ca}^+)$ is $\lesssim 100$. Although this only relates to the stronger component of the [Ca II] doublet, the [Ca II] λ7324 line comprises roughly 40 percent of the overall contribution from [Ca II] (see Table 7). The other [Fe II] blended components will contribute much less flux as the Einstein A values are a factor of 2-3 less than the [Fe II] λ7155 transition.

Despite the level excitation energy of Ca$^+$ ^{2}D$_{5/2}$ and Fe$^+$ a^{2}G$_{9/2}$ being similar ($\sim$16 percent difference), the average level populations in LTE can be several orders of magnitude different for the same total ion population. The average LTE level population compared to the total is simply

$$\begin{aligned} \frac{\langle N(\mathrm{Fe}^+[\mathrm{a}\,^2\mathrm{G}_{9/2}])\rangle}{N(\mathrm{Fe}^+)} &= \frac{1}{Z} g_{\mathrm{a}\,^2\mathrm{G}_{9/2}} e^{-E[\mathrm{a}\,^2\mathrm{G}_{9/2}]/kT} \\ &= \frac{1}{Z} 10 e^{-1.964\,\mathrm{eV}/kT}, \end{aligned} \tag{4.1}$$

where Z is the partition function. For temperatures of 2000, 5000, and 10 000 K, the partition function (using the first 18 levels) is approximately 28, 43, and 58 respectively assuming the states are in LTE with respect to the ground state. Since Fe$^+$ has many easily excited lower levels, then even for the same ion abundance between Ca$^+$ and Fe$^+$, the emission from Ca II will dominate the blended feature at 7200 Å.

The strong emission of the [Ca II] $\lambda\lambda$7291, 7324 doublet is not only a result of the ionization, temperature, and electron density but also coupled to the radiation field. The Ca II H&K lines have large oscillator strengths and can pump electrons into the upper ^{2}P$^{\mathrm{o}}$ levels. They then decay to the ^{2}D state, which again decays to the ^{2}S ground state giving us [Ca II] $\lambda\lambda$7291, 7324 emission. We have taken our ionization, temperature, and electron density structure from CMFGEN and re-solved for the level populations of Ca$^+$ assuming only collisional and radiative decay processes. For levels that are coupled to UV transitions, this assumption is only accurate within 50%. We then solved the relativistic radiative transfer

equation for line emission of Ca II with zero opacity. Our results (see Figure 50) show the spectra of Ca II is sensitive to the radiation field. Flux is absorbed in the Ca II H&K lines which can then be emitted in the Ca II NIR triplet as well as the [Ca II] $\lambda\lambda$7291, 7324 doublet. Despite the critical densities for Ca^+ $^2D_{3/2}$ and $^2D_{5/2}$ being on the order of $\sim 10^5 - 10^6$ cm^{-3}, the atomic levels above the Ca^+ $^2D_{3/2}$ and $^2D_{5/2}$ have sufficiently high critical densities which inhibits collisional de-excitations locking these levels to their LTE value.

Such strong [Ca II] emission could indicate a problem with our atomic data for Fe I/Fe II or likely be an indication of more stratified material in our 1D models. Element stratification within the ejecta also influences the strength of the lines belonging to IMEs. In particular, the presence of some ^{56}Co in the IME zone means that positrons are available as a heating source after the ejecta has become optically thin to γ-ray photons. However, even at late times, this contributes only a fraction of non-thermal heating in the inner region. γ-rays still scatter out into the ejecta, heating some of the outer layers.

If the problem lies not with our atomic data, then stratification is the cause of strong IME emission. This puts a constraint on the nucleosynthetic distribution of calcium produced in SNe Ia. This either prohibits an overlap between the calcium and the radioactive isotopes like ^{56}Ni, or this constrains the mass of calcium produced during the nucleosynthesis. Not surprisingly, when we artificially scaled down the mass of calcium by a factor of 2 in our CHAN $f = 0.25$ clumped model, the peak flux drops by half. This also has implications for understanding the early-time light curves. In order to produce the blue colors of SNe Ia, studies routinely mix ^{56}Ni into the outer layers of the ejecta in DDT models.

4.4 CONCLUSION

We have performed 1D radiative transfer calculations using CMFGEN for two ejecta models (one sub-M_{Ch} detonation and one M_{Ch} DDT – see Chapter 3 for more details) utilizing micro-clumping at 216.5 days post explosion. Our goal was to understand the influence of micro-clumping on nebular spectra and to test when clumped models would provide a better fit to the observed level of ionization in Ia spectra. Clumping is expected to occur

naturally in SN ejecta and naturally reduces the ionization by enhancing recombination. We considered three different clumping factors, 0.33, 0.25, and 0.10, which we assumed were constant throughout the ejecta. Our models are in a regime where potentially small changes can shift the ionization. This also means that our models are sensitive to atomic physics.

Clumping lowers the average ionization of all species. The average ionization of IMEs is reduced by about one electron below 10 000 km s^{-1} and roughly one half of an electron for IGEs (except cobalt which is reduced by roughly an electron). Despite clumping lowering the ionization in SUB1, the nickel ionization remained high in the inner region due to a lack of a "^{56}Ni hole." With an already reduced stable nickel mass compared to CHAN, SUB1 failed to show strong emission from Ni II in the optical and in the NIR with the [Ni II] 1.939 μm line.

As iron is the most abundant species in the inner ejecta at 216 days, clumping had the most visible effect on the flux of [Fe III] features such as [Fe III] $\lambda\lambda$4658, 4702. As the iron ionization is lowered, the flux in Fe II features increases, and permitted Fe I lines near 5500 Å emerged. These Fe I lines cause a shoulder to form on the [Fe II] and [Fe III] optical blend between 4200-5400 Å. Our attempts to model the [Fe II] $\lambda\lambda$4287, 4359 feature were unsuccessful. While clumping generally enhanced the strength of [Fe II] features, absorption by other transitions limit its strength. Despite the difficulty in reproducing [Fe II] $\lambda\lambda$4287, 4359, we show that the [Fe II] complex around 12500 Å is completely reproduced under simple physics assumptions of collisional and radiative decays from a given ionization and temperature structure. In the IR, particularly from 10 000-11 800 Å, changes in the flux of Fe I lines of several orders of magnitude for a factor of a few change in density.

For the same ^{56}Ni mass, M_{Ch} explosions produce more IMEs compared to sub-M_{Ch} explosions. We have seen that only large clumping can sufficiently suppress emission from IMEs such as Ar III and S III. However, as we increase clumping, both models show an increase in the [Ca II] $\lambda\lambda$7291, 7324, which dominates over the [Fe II] λ7155 feature. Since the presence/absence of [Ca II] in this 7200 Å blend is still highly uncertain, we suggest that SN Ia ejecta require less mixing between the original ^{56}Ni and the calcium distribution.

Despite arguments that mixing is required to reproduce early-time LCs, mixing between layers of IMEs and ^{56}Ni is inconsistent with what is observed at nebular times, since

Model	Mass ($M_\odot$)	S ($M_\odot$)	Ar ($M_\odot$)	Ca ($M_\odot$)	Fe ($M_\odot$)	Co ($M_\odot$)	^{58}Ni + ^{60}Ni ($M_\odot$)	^{56}Ni ($M_\odot$)
SUB1	1.04	1.046(-1)	2.273(-2)	2.361(-2)	2.226(-2)	5.526(-2)	1.113(-2)	5.684(-1)
CHAN	1.40	1.661(-1)	3.693(-2)	4.120(-2)	1.020(-1)	5.713(-2)	2.517(-2)	5.708(-1)

Table 6 Model mass information in $M_\odot$ at 0.75 days post explosion. The parentheses (#) correspond to $\times 10^{\#}$.

the emission reflects where most of the energy is deposited. Therefore, the strength of time-dependent IME features in nebular spectra is a crucial diagnostic for understanding progenitors of SNe Ia.

Better atomic data can also assist determining the sensitivity it has on the Fe I/Fe II/ Fe III features in producing nebular spectra. Because the focus of this work is on nebular phase modeling, further work is necessary to test the time-dependent effects of various levels of clumping. It would be helpful to perform full time-series calculations. Clumping should be fully explored to truly understand the nature of the progenitors of SNe Ia.

Ca^+										
Upper level u			Lower level l			A_{ul}	Wavelength	$N_{\rm crit}(T_4=0.1)$	$N_{\rm crit}(T_4=0.5)$	$N_{\rm crit}(T_4=1.0)$
Term	g	E_u (eV)	Term	g	E_l (eV)	(s^{-1})	(Å)	(cm^{-3})	(cm^{-3})	(cm^{-3})
$^2D_{5/2}$	6	1.699932	$^2S_{1/2}$	2	0.000	8.025(-1)	7291.469	7.722(5)	1.717(6)	2.125(6)
$^2D_{3/2}$	4	1.692408	$^2S_{1/2}$	2	0.000	7.954(-1)	7323.888	6.070(5)	1.290(6)	1.645(6)
Fe^+										
Upper level u			Lower level l			A_{ul}	Wavelength	$N_{\rm crit}(T_4=0.1)$	$N_{\rm crit}(T_4=0.5)$	$N_{\rm crit}(T_4=1.0)$
Term	g	E_u (eV)	Term	g	E_l (eV)	(s^{-1})	(Å)	(cm^{-3})	(cm^{-3})	(cm^{-3})
a $^2G_{9/2}$	10	1.96448603	a $^4F_{9/2}$	10	0.23217278	1.4950(-1)	7155.157	5.165(6)	9.130(6)	9.618(6)
a $^2G_{7/2}$	8	2.02954814	a $^4F_{7/2}$	10	0.30129857	5.6950(-2)	7172.004	2.415(6)	4.010(6)	4.207(6)
a $^2G_{7/2}$	8	2.02954814	a $^4F_{5/2}$	6	0.35186476	4.3450(-2)	7388.178	2.415(6)	4.010(6)	4.207(6)
a $^2G_{9/2}$	10	1.96448603	a $^4F_{7/2}$	10	0.30129857	4.8450(-2)	7452.538	5.165(6)	9.130(6)	9.618(6)

Table 7 The parentheses (#) correspond to $\times 10^{\#}$. T_4 is just $T/(10^4 K)$.

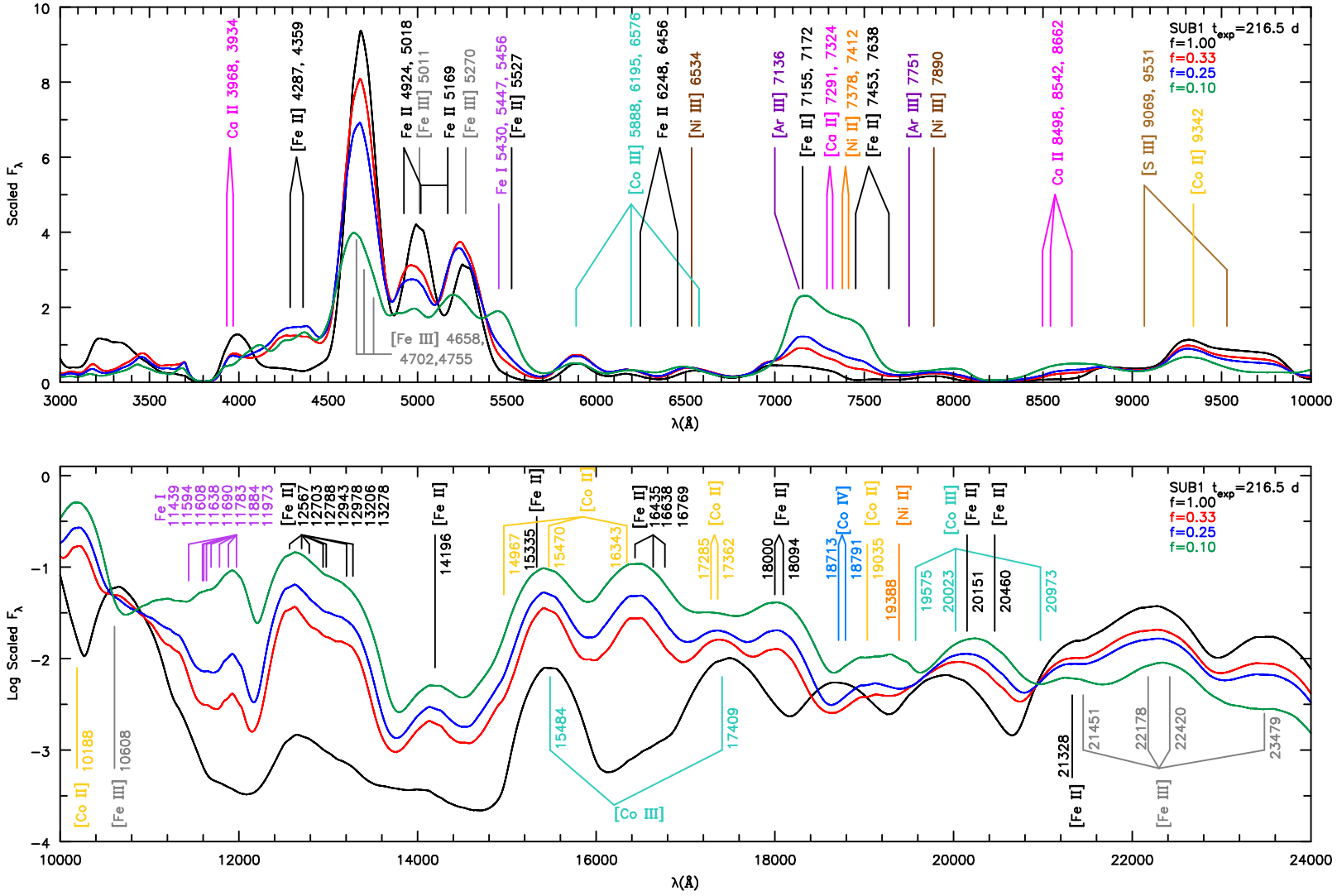

Figure 39 Spectra of SUB1 at 216.5 days post-explosion compared to the spectra computed using different clumping factor values (0.33, 0.25, and 0.1). The spectra have all been scaled by the same value. To contrast the little flux in the IR, we show the logarithm of the flux. In the IR, particularly from 10 000-11 800 Å, changes are several orders of magnitude for a factor of a few in density.

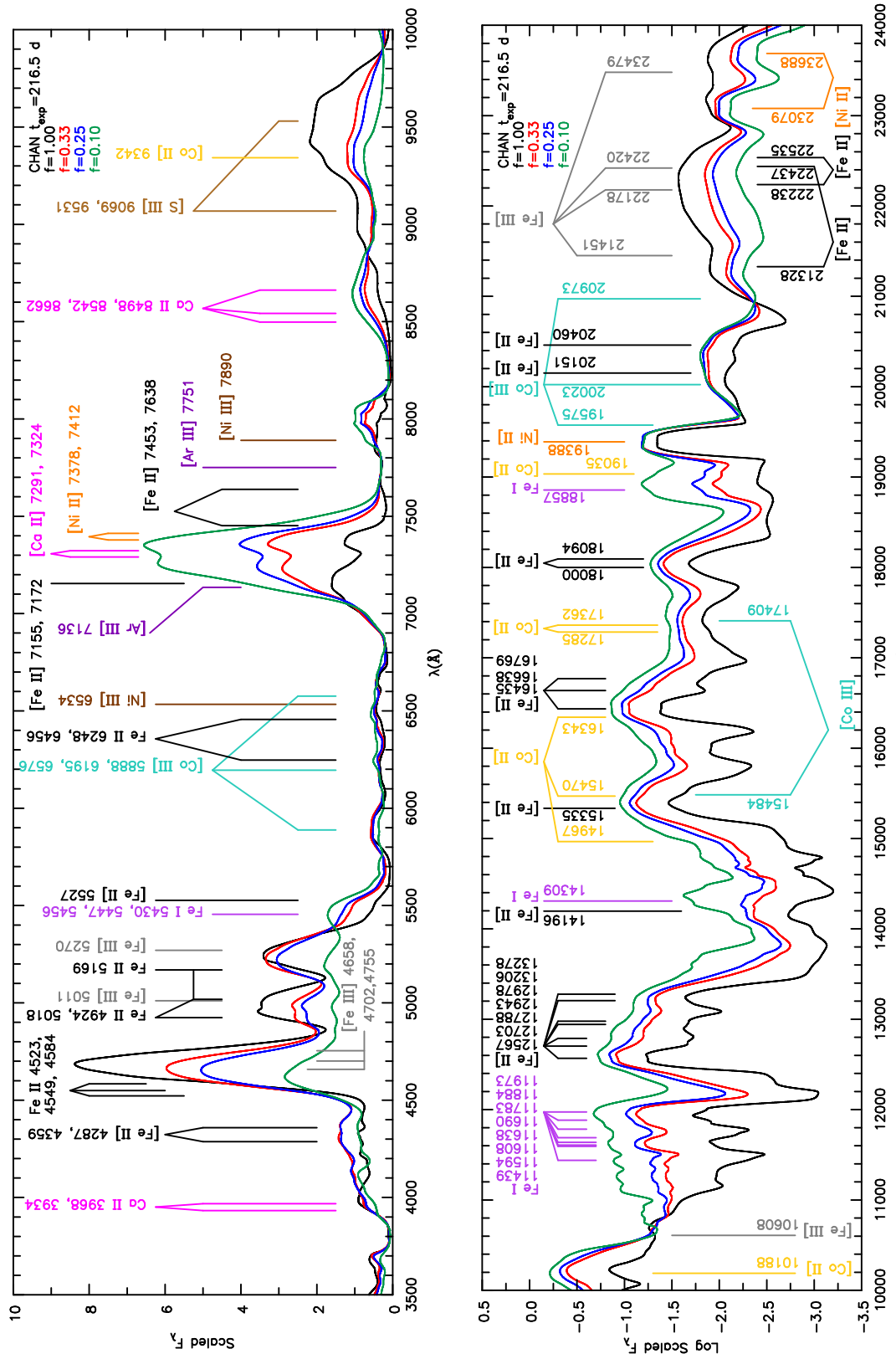

Figure 40 Spectra of CHAN at 216.5 days post-explosion compared to the spectra computed using different clumping factor values (0.33, 0.25, and 0.1). The spectra have all been scaled by the same value (and also to Figure 39). To contrast the little flux in the NIR, we show the logarithm of the flux. Differences between the spectra can be large (greater than a factor of 10) for Fe I and Fe II features for just a factor of 3 or more in density.

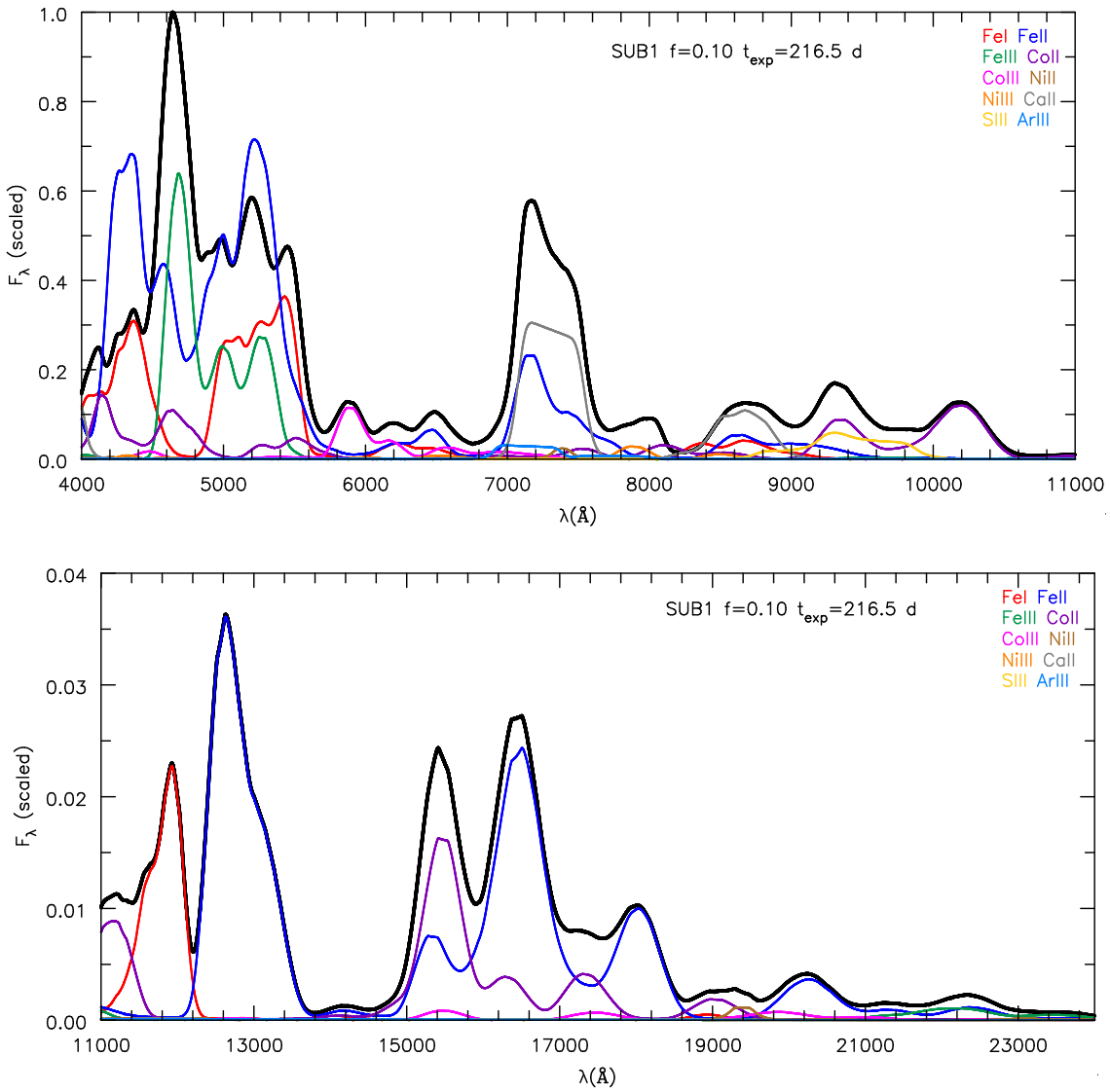

Figure 41 Observer's frame spectrum (thick black line) of SUB1 along with the component spectra of Fe I, Fe II, Fe III, Co II, Co III, Ni II, Ni III, Ca II, S III, and Ar III at 216.5 days post-explosion for a clumping factor of $f = 0.10$. If the optical depth effects are unimportant, the component spectrum will sum to the total to produce the full spectrum (thick black line). Conversely, we see that the features between 4000-5500 Å cannot be understood without allowing for optical depth effects.

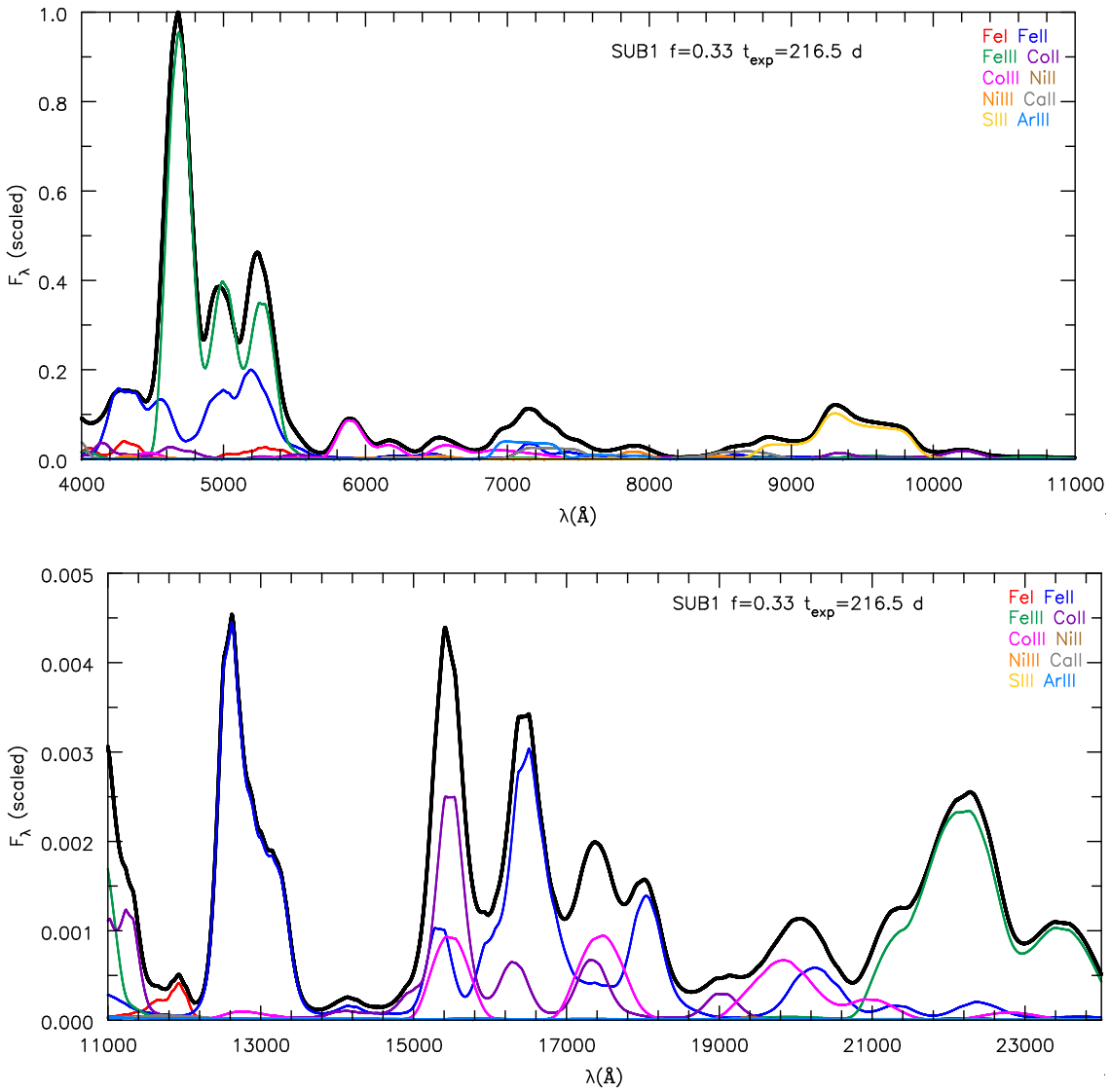

Figure 42 Observer's frame spectrum (thick black line) of SUB1 along with the component spectra of Fe I, Fe II, Fe III, Co II, Co III, Ni II, Ni III, Ca II, S III, and Ar III at 216.5 days post-explosion for a clumping factor of $f = 0.33$. If the optical depth effects are unimportant, the component spectrum will sum to the total to produce the full spectrum (thick black line). Conversely, we see that the features between 4000-5500 Å cannot be understood without allowing for optical depth effects.

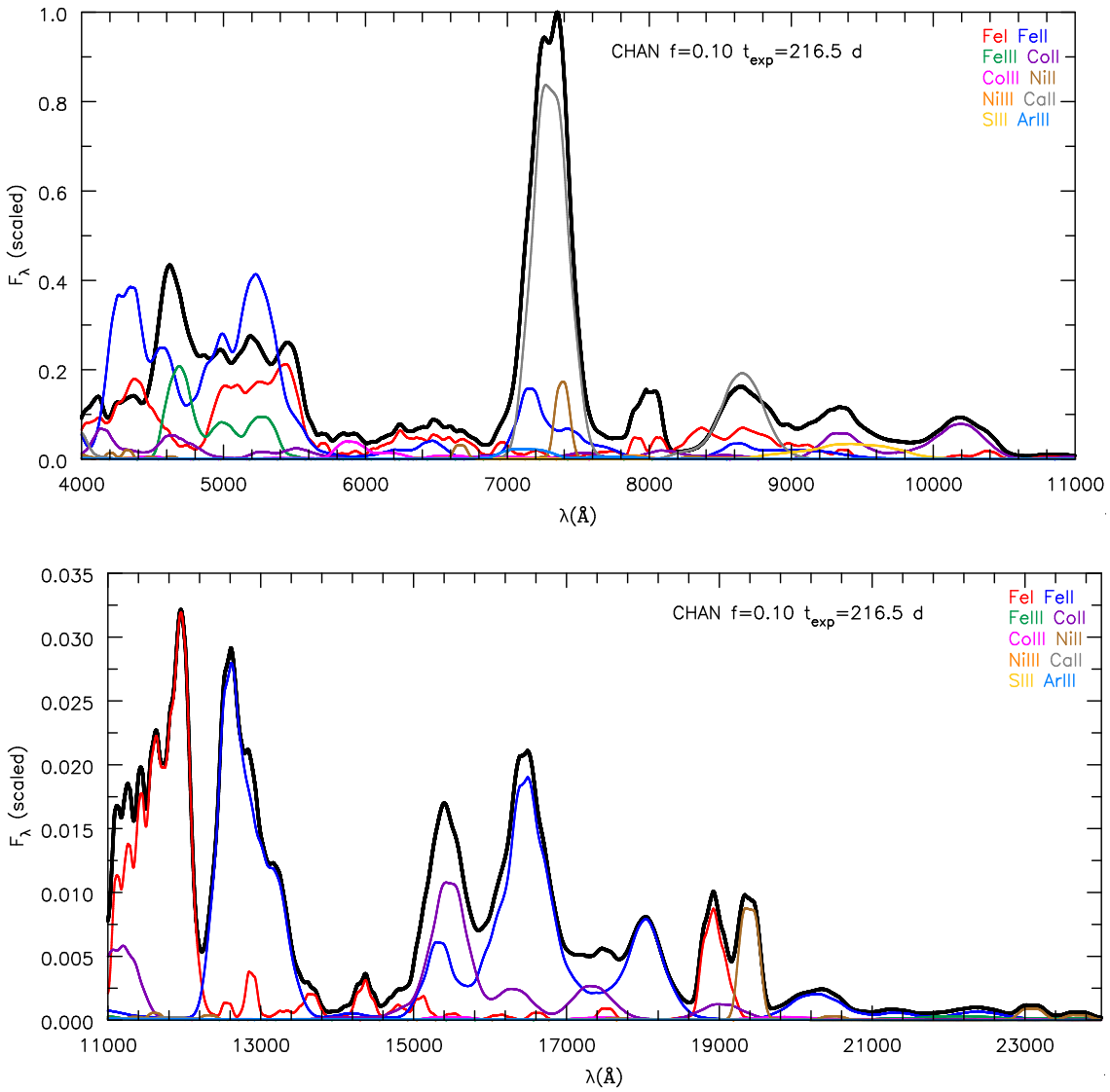

Figure 43 Observer's frame spectrum (thick black line) of CHAN along with the component spectra of Fe I, Fe II, Fe III, Co II, Co III, Ni II, Ni III, Ca II, S III, and Ar III at 216.5 days post-explosion for a clumping factor of $f = 0.10$. If the optical depth effects are unimportant, the component spectrum will sum to the total to produce the full spectrum (thick black line). Conversely, we see that the features between 4000-5500 Å cannot be understood without allowing for optical depth effects.

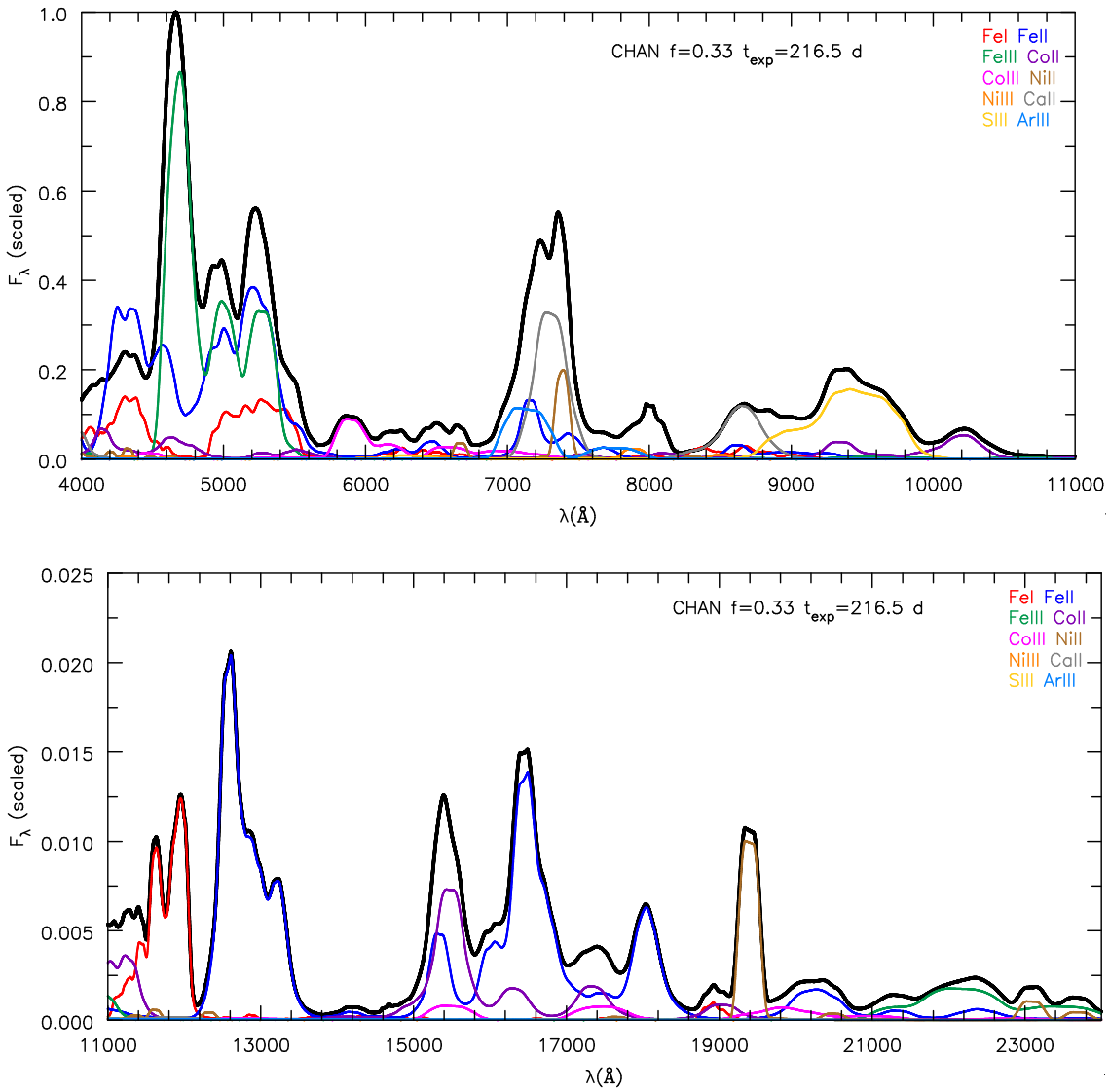

Figure 44 Observer's frame spectrum (thick black line) of CHAN along with the component spectra of Fe I, Fe II, Fe III, Co II, Co III, Ni II, Ni III, Ca II, S III, and Ar III at 216.5 days post-explosion for a clumping factor of $f = 0.33$. If the optical depth effects are unimportant, the component spectrum will sum to the total to produce the full spectrum (thick black line). Conversely, we see that the features between 4000-5500 Å cannot be understood without allowing for optical depth effects.

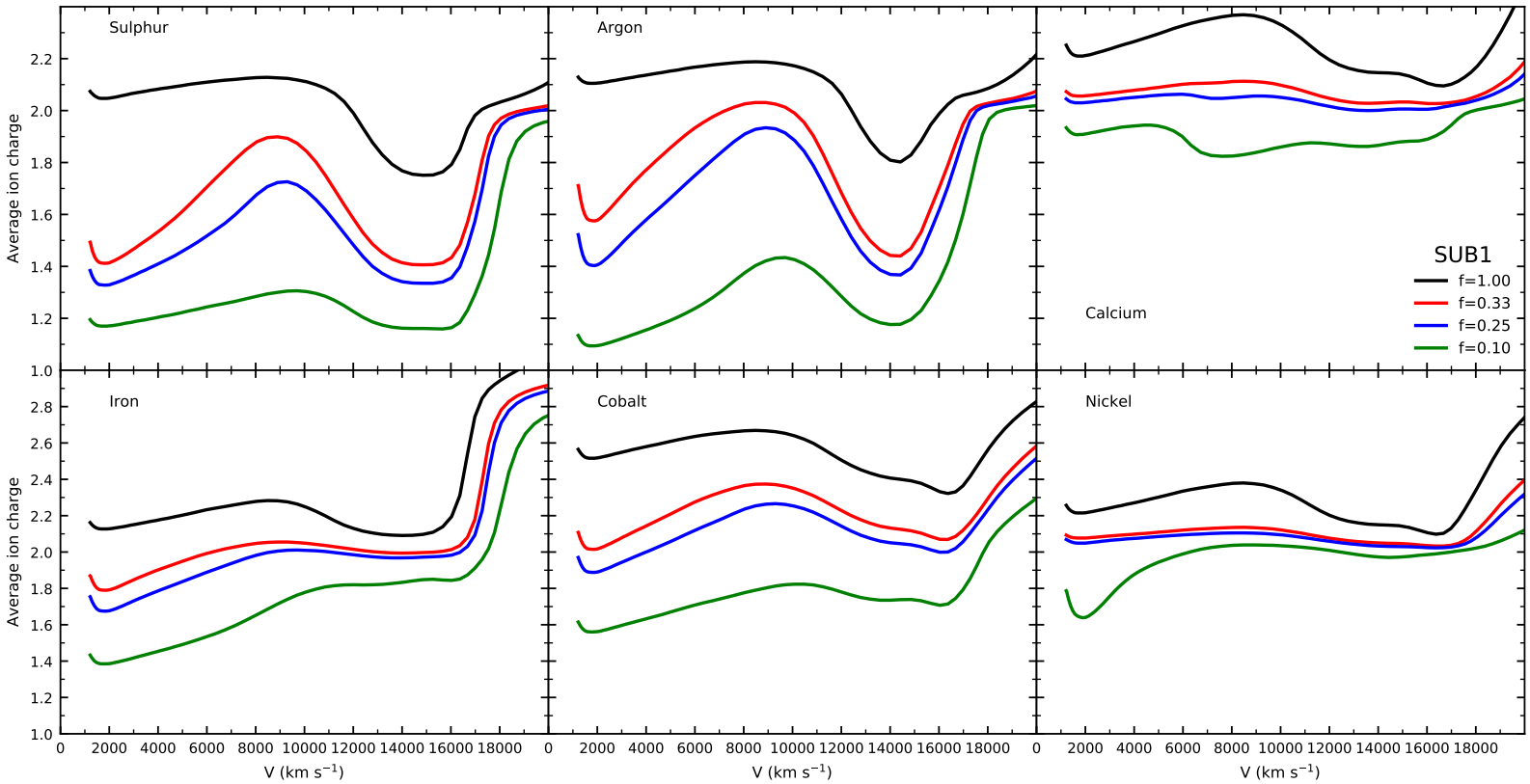

Figure 45 Model SUB1 average charge on species for sulfur, argon, calcium, iron, cobalt, and nickel for clumping factors of 1.00, 0.33, 0.25, and 0.10 at roughly +200 d after maximum. The ionization is largely sensitive to the clumping factor and the non-thermal energy deposition in the inner ejecta. Sulfur and argon show changes of roughly one electron, while iron shifts from mostly Fe^{2+} to nearly equal parts Fe^{2+} and Fe^{+}. The majority of the stable nickel is located in the inner ejecta, and in this region the ionization is driven by the radioactive decay deposition. These changes in the inner region relate to large changes on the spectra.

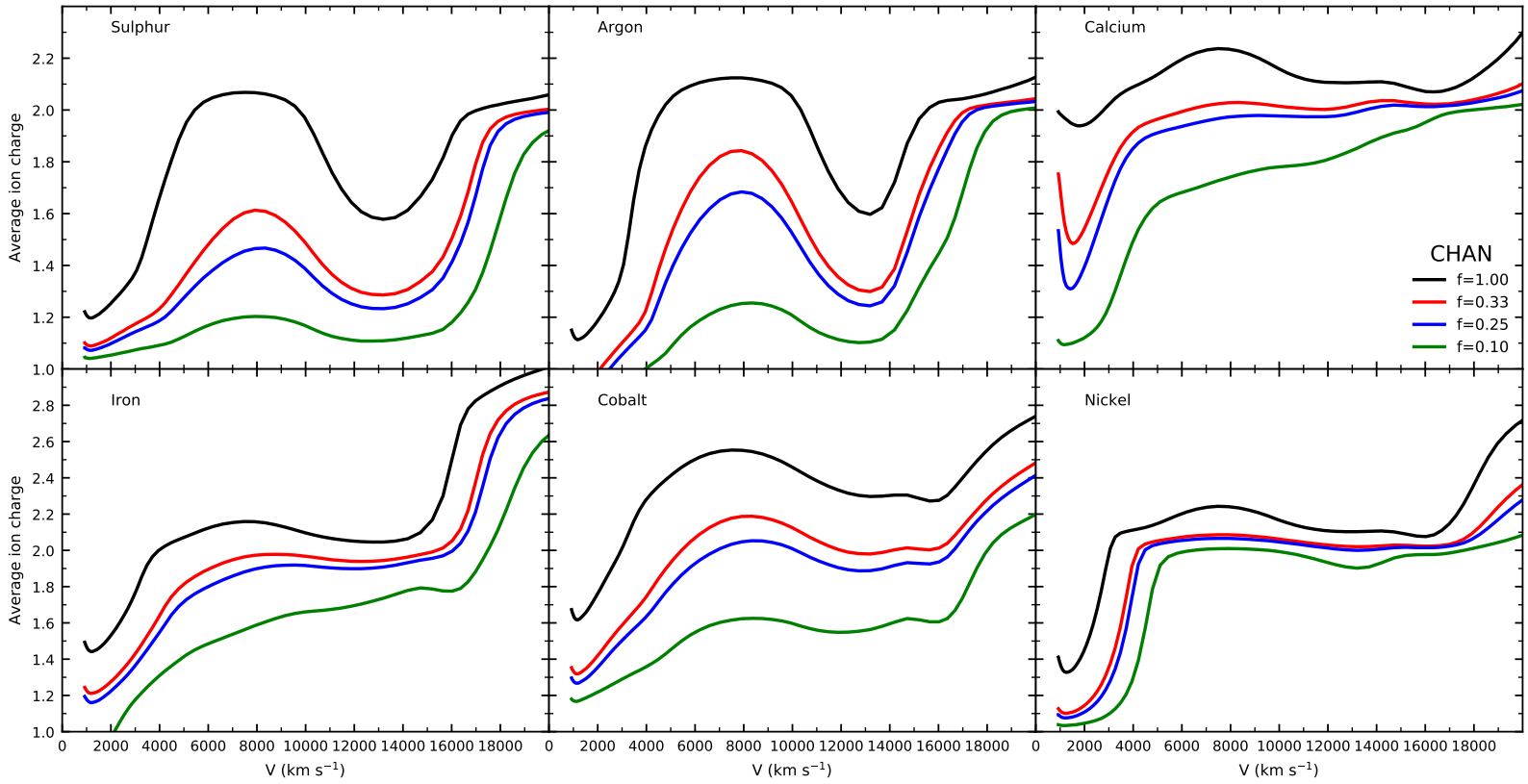

Figure 46 Same as Figure 45 but for model CHAN. The changes in the ionization are smallest (except for calcium) in the region of the "^{56}Ni hole" between different amounts of clumping. The slope of the average ionization of iron and other species in the inner region highlights that small changes can shift the ionization.

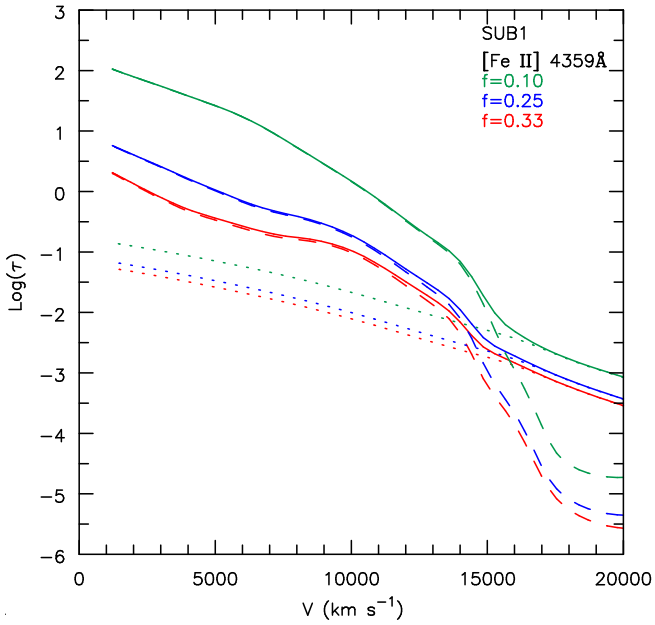

Figure 47 The optical depth to [Fe II] λ4359 resonance zone at velocity V for various clumping factors for SUB1. We consider this along the first core impact parameter ($p_1 = 0$). The dashed lines correspond to the sum total of all lines that interact with the [Fe II] λ4359 line emitted at a particular resonance zone. The dotted lines correspond to the continuum contribution, and the solid lines represent the total [Fe II] λ4359 optical depth to the resonance zone.

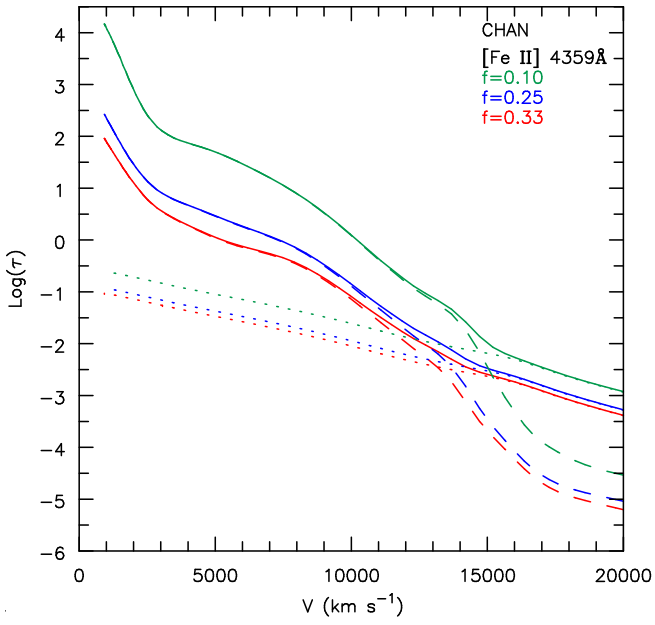

Figure 48 Same as Figure 47 but now for model CHAN.

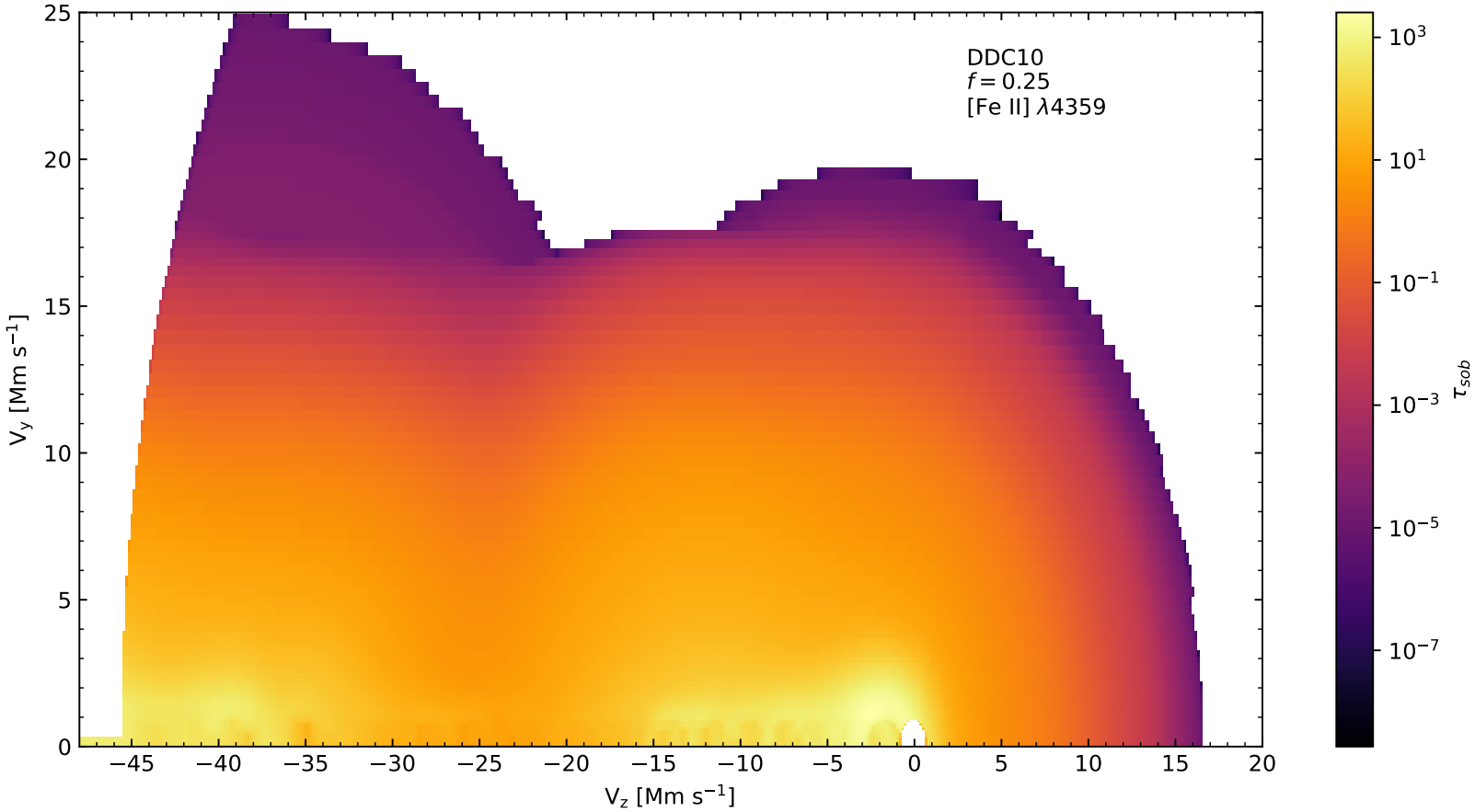

Figure 49 The 2D optical depth of the [Fe II] λ4359 (just as in Figures 47 and 48) along rays parallel to the z-axis for various impact parameters (y-direction). We only consider interacting lines whose Sobolev optical depth at their resonance zone is greater than 10^{-5}. We interpolate the results from our 1D grid onto a rectangular grid. The white space is where the optical depth is zero.

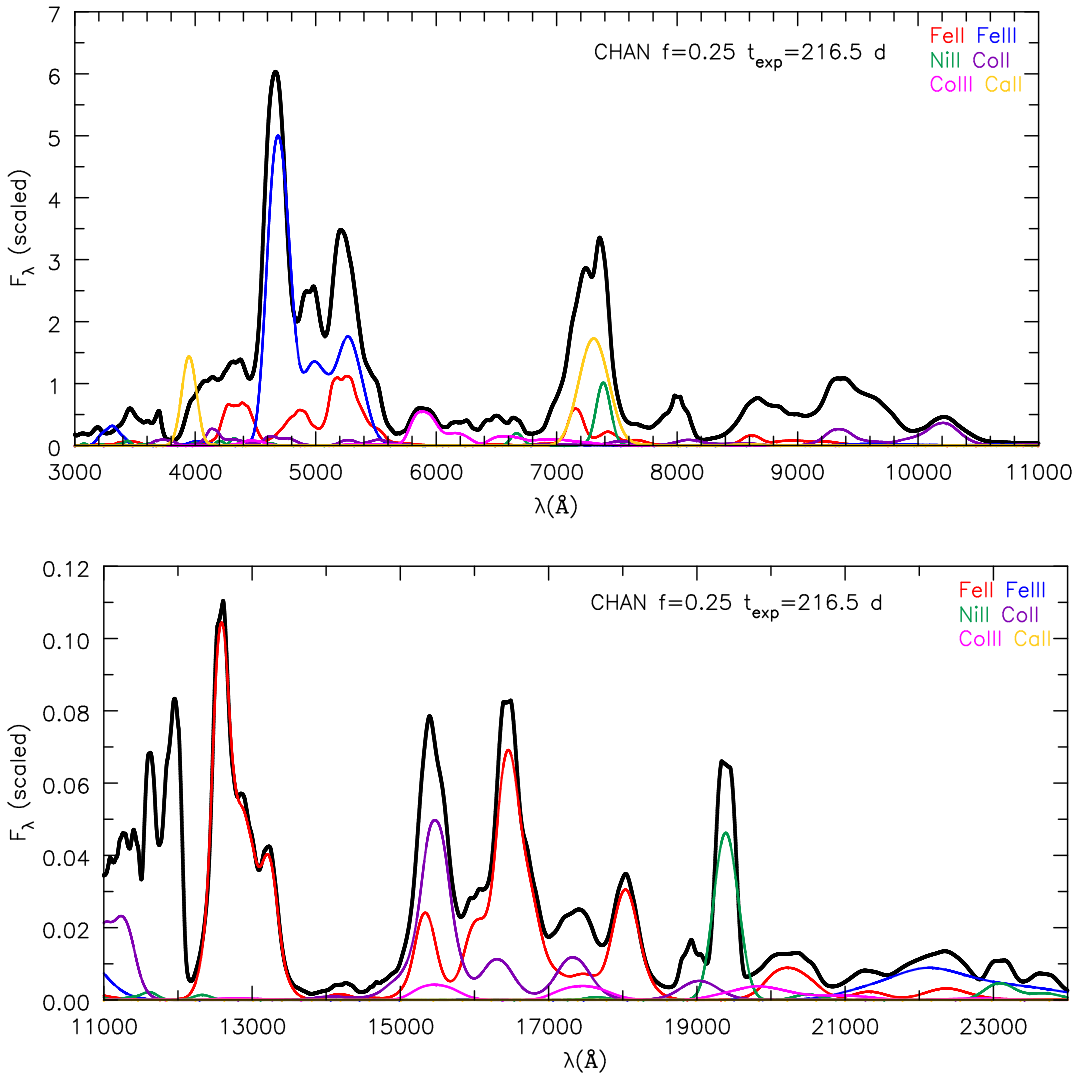

Figure 50 Observer's frame emission spectra of Fe II, Fe III, Ni II, Co II, Co III, and Ca II. We show the full observer's frame spectrum in black. The emission spectra are calculated by taking the temperature and ionization structure output from CMFGEN and re-solving the level populations assuming only collisional processes and radiative decays. We assume Gaussian emission profiles of 100 km s^{-1} in the CMF.

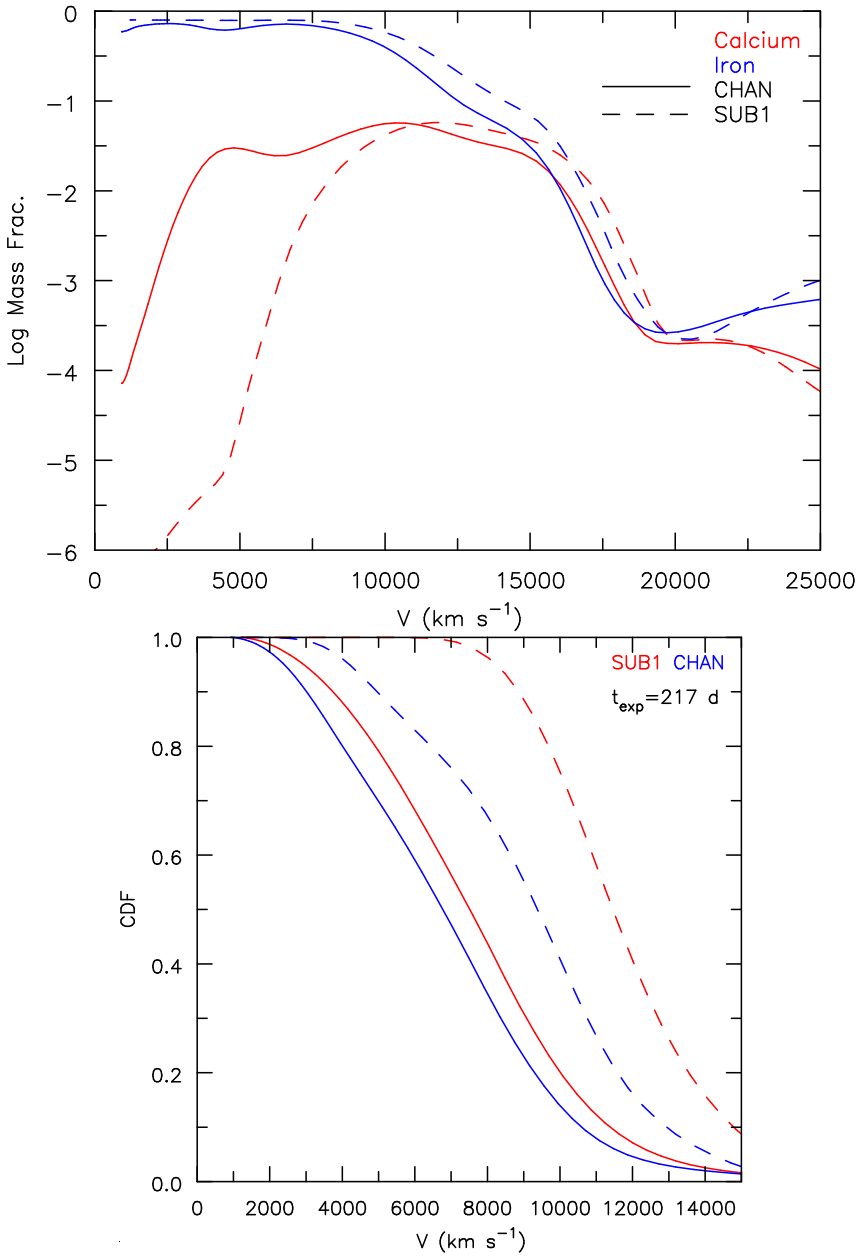

Figure 51 Top plot is the mass fractions for calcium and iron in both models. The solid line corresponds to model CHAN, and the dashed line corresponds to SUB1. The bottom plot is the cumulative distribution function for the energy deposition (solid lines) and the calcium mass (dashed lines) at 217 days after explosion (roughly +200 days).

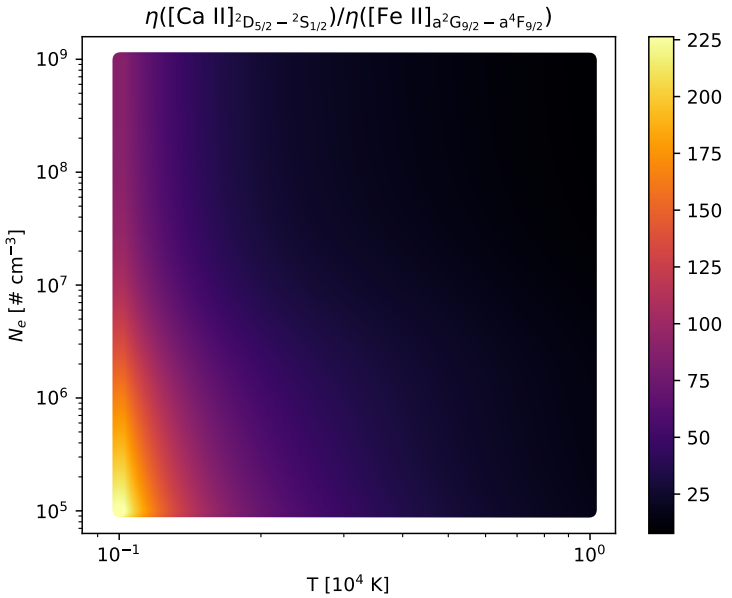

Figure 52 Line emission ratio of the [Ca II] λ7291 to [Fe II] λ7155 assuming N(Fe^+)/N(Ca^+) is unity. The emission ratio is calculated by solving the rate equations with only collisional and radiative decay terms for a fixed ionization of N(Fe^+)/N(Ca^+)=1. The emission ratio favors strong calcium. When this ionization ratio is $\gtrsim$50 the iron would begin to dominate the 7200 Å complex.

5 CONCLUSIONS

This thesis is an attempt to solve the unanswered questions regarding SNe Ia such as "What is the progenitor system?" and "What is the physics of the explosion?". To do this, I performed radiative transfer simulations on a set of 1D hydrodynamic explosion models to understand SNe Ia spectra during various epochs (0.75–217 days) and at different energies (γ-rays and UV through MIR). I wanted to determine and understand what predictions this set of hydrodynamic models make and if these predictions match observables seen in SNe Ia spectra. I did so by first focusing on developing a radiative transfer code for γ-rays in SNe ejecta (see chapter 2). Not only was this work important as a consistency check of the Monte Carlo code of Hillier & Dessart (2012) but also it was important for reliable energy deposition calculations. Next, I performed full time dependent radiative transfer simulations with our set of hydrodynamic models to investigate ejecta mass diagnostics for SNe Ia (see chapter 3), providing several important diagnostics for the community to investigate further. Finally, I focused on nebular modeling to understand the physics behind nebular spectra (see chapter 4). Since the photospheric phase seems largely insensitive to the explosion mechanism (see chapter 3) studying nebular spectra is crucial for determining the progenitor system and the explosion physics.

5.1 FUTURE WORK

Spectra are the best way to understand the nature of SNe Ia. Modeling spectra is the leading way to determine the important physics responsible for spectral formation. To expand this research further, additional modeling is necessary to provide constraints on SNe Ia. In my

study of ejecta mass diagnostics, I focused on a set of models with the same ^{56}Ni mass (0.62 $M_{\odot}$). In order to explore all possible ejecta mass diagnostics, additional ^{56}Ni masses should be investigated with varying ejecta mass at fixed nickel mass. My study of ejecta mass diagnostics also included two explosion scenarios (direct explosion of a sub-M_{Ch} and DDT of a M_{Ch} – see chapter 3). Additional investigation is required to test PDD and other explosion scenarios. PDD models are useful to test low velocity features of IMEs and possible C II features seen in photospheric spectra. Although our models were able to reproduce Ca II HVFs in early spectra, additional investigations are required to explain HVFs of Si II λ6355.

Although our knowledge of "standard" SNe Ia is substantial, our understanding of peculiar SNe Ia is lacking. SN1991T has been claimed to be both sub-M_{Ch} and super-M_{Ch}(Stritzinger et al., 2006; Scalzo et al., 2012; Sasdelli et al., 2014). A lack of consensus among the community warrants further investigation of SN1991T and SN1991T-like objects. Taubenberger (2017) highlights the open questions of peculiar thermonuclear SNe: What are the nature of SN1991T-like (luminous and early iron blanketing), SN1991bg-like (cool and subluminous), SN2002es-like (slow declining and subluminous) SNe? Performing radiative transfer modeling can constrain the parameter space from which these progenitor systems may come.

Studies of nebular spectra are investigations of the innermost part of the ejecta, as the ejecta has for the most part become optically thin. Future investigations should be able to reproduce the [Fe II] $\lambda\lambda$4287, 4359 line whose strength is dependent on the ionization structure of the ejecta. For clean nebular lines devoid of blended components, studies should focus on line shifts, which will help determine the ionization structure of the ejecta, and compare them with models. The relative distribution of ^{56}Ni and IMEs in the ejecta is crucial for understanding nebular spectra. Nebular phase modeling of ejecta arising from different explosion mechanisms for a range of mass can in principle be done as time dependent calculations, as much of the time dependence drops out of the rate equations since recombination time-scales are short. Additional investigations of clumping beyond what is included in this thesis are also important for understanding nebular spectra. This thesis only included the simple assumption that the clumping is homogeneous. This simple assumption should be relaxed and more complicated models, where the level of clumping is a function of radius

and species, should be compared to observations. However, this adds an additional level of "fine tuning" to the problem.

Gamma-ray astronomy for SNe is largely non-existent due to the few photons that reach us from these events. To date, two SNe (SN1987A and SN2014J – see chapter 2) have observations of γ-rays from radioactive decays. The telescope INTEGRAL obtained γ-ray observations of SN2014J, although this data is still of low resolution for the closest SNe Ia in 40 years. FERMI is another γ-ray telescope capable of such observations. With future γ-ray observations, measuring the line flux and blueshifts in the peak emission allow one to constrain the density structure and original ^{56}Ni distribution in SNe Ia models.

With the advent of new telescopes coming online in the upcoming years (such as LSST), the supernova community will have countless data to investigate the underlying nature of SNe Ia. We may very well soon be able to answer the questions, "Do SNe Ia originate from the SD or DD channel or both?" and "How do WDs explode to give rise to SNe Ia?"

APPENDIX A

ABBREVIATION SUMMARY

CCSN(e): core-collapse supernova(e)

CMF: comoving frame

C/O: carbon-oxygen

DD: double degenerate

DDT: delayed detonation transition

GCD: gravitationally confined detonation

HVF: high velocity feature

IGE(s): iron group element(s)

IME(s): intermediate mass element(s)

LC: light curve

LTE: local thermodynamic equilibrium

$\mathbf{M_{Ch}}$: Chandrasekhar mass

MIR: mid infrared

NIR: near infrared

non-LTE: non-local thermodynamic equilibrium

NSE: nuclear statistical equilibrium

PDD: pulsational delayed detonation

(R)RTE: (relativistic) radiative transfer equation

SD: single degenerate

SN(e): supernova(e)

SN(e) Ia: Type Ia supernova(e)

$\boldsymbol{\rho_t}$: transition density

UV: ultraviolet

WD: white dwarf

WLR: width luminosity relation

WR: Wolf-Rayet

APPENDIX B

INPUTS FOR MODEL COMPUTATION USING CMFGEN

In order to run a SN ejecta model time sequence, CMFGEN requires a SN hydrodynamic file (SN_HYDRO_DATA) that includes the following:

1. Number: hydro depth points, mass fractions, isotopes
2. time since explosion (necessary to adjust grid for expansion and track radioactive decays)
3. radial grid
4. velocity grid
5. temperature structure (initial temperature structure is either supplied from explosion hydro simulation or a static grey temperature can be used to generate an initial temperature profile)
6. mass density
7. atom density
8. electron density
9. mass fractions
10. isotope mass fractions

Another necessary input model specifier file (MODEL_SPEC) required for model computation specifies the following:

1. depth points (ND), number of core rays (NC), the number of impact parameters (NP)
2. number of bands (which specifies the way the equations are linearized – i.e. tri-diagonal, etc.)

3. maximum number of frequencies
4. maximum number of overlapping Doppler line profiles treated with blanketing
5. number of possible bound-bound transitions
6. each ionic species listing the number of important levels, super-levels, and total levels

CMFGEN also requires a variable options data file (VADAT) which allows the user to modify the control options while running a model. If an option is not included, CMFGEN uses the default values. For SNe, it is important to specify the following options:

- [DO_DDT]=T – Option to include advection terms (i.e. the CM derivative) in the rate equations.
- [USE_J_REL]=F
- [INCL_REL]=F – Includes relativistic terms in the transfer equation, but it used when USE_J_REL is true.
- [INCL_ADV_TRANS]=F – Option to include advection terms in the transfer equation. It should only be true when USE_J_REL and INCL_REL are both true.
- [INCL_DJDT]=T – Option to include the DJ_ν/Dt terms in the transfer equation for a homologous expansion (Hubble flow). If true, USE_DJDT_RTE and USE_FRM_REL should also be set to true.
- [USE_DJDT_RTE]=T – Option that forces the DJ_ν/Dt transfer routines to be used.
- [USE_FRM_REL]=T – This option uses the fully relativistic ray equation to solve for the Eddington factors ($f_\nu = K_\nu/J_\nu$).
- [REL_OBS]=T – This option determines if all relativistic terms are included when calculating the observer's frame solution.
- [REL_CMF]=T – This option determines if all relativistic terms are included when calculating the CMF solution for the observed intensity.
- [PURE_HUB]=T – This option will force the velocity law to be a pure Hubble flow, which is expected in SN ejecta.
- [INC_RAD_DECACYS]=T – SNe Ia are powered by radioactive decays, so it is crucial that this option is turned on. This option will require the use of nuclear decay data that

includes the isotope information such as decay channels, mass, half life, and energy per decay, along with decay kinetic energy from positrons.

- [GAMRAY_TRANS]=LOCAL – This option specifies the γ-ray transfer for energy deposition. At early times ($\leq$ 6 days), LOCAL should be used, after which ABS_TRANS or NON_LOCAL should be used. ABS_TRANS is a fast option that assumes the transfer is grey and averages the energy loss for a single scattering approximation. NON_LOCAL signifies that the energy deposition is being read in from a file. First, one must run the Monte Carlo γ-ray code to generate the energy deposition as a function of depth. This method is more accurate. A new option has been developed (only currently implemented for testing – see section 2) for time dependent calculations.
- [INS_DEP]=T – This option is somewhat new, and it allows one to include the instantaneous energy deposition from radioactive decays. It is likely more accurate than the default option to average the deposition over the time step.
- [TS_NO]=1,2,3, etc. – This option tells CMFGEN which time-step is being used for model calculation. If TS_NO is set to 1 for the first time-step, then the model must be computed ignoring time derivatives.
- [SN_AGE]=1.0 – This option specifies the age in days of the time step for model computation.
- [LIN_INT]=F – This option interpolates the level populations onto the new radius grid.
- [LTE_EST]=F – Option to use the LTE estimates of the level populations. In SNe, level populations are out of LTE.
- [FIX_T]=T – This option should be used to start any new model to allow corrections to stabilize before the temperature should vary.
- [T_MIN]=0.3 – This option set the lower limit for the temperature while converging a model.
- [DC_METH]=R – This option controls the independent variable when the coefficients used to quantify the departures from LTE are interpolated onto a new radius grid.
- [GF_CUT]=1.0D-03 – This option controls the minimum gaunt factor for which lines are included. The gaunt factor is a multiplicative factor in the absorption coefficient.

- [INC_AD]=T – This option is for including adiabatic cooling in the energy balance equation.
- [N_PAR]=5000 – This option controls after how many frequencies is the matrix used to solve the statistical equilibrium equations updated. Since SNe models have large model atoms, a large value like 5000 is adequate.
- [DO_NG]=T – Option to include an iteration called an Ng-acceleration as described above in section 1.8. It should be used when the fractional corrections to the populations are less than 5–10% and after at least 15 iterations have been performed.
- [EPS_TERM]=0.01 – This option specifies the percent fractional change in the populations for which the code terminates.

BIBLIOGRAPHY

Anderson, J. P., González-Gaitán, S., Hamuy, M., et al. 2014, ApJ, 786, 67

Arnett, W. D. 1969, APSS, 5, 180

—. 1982, ApJ, 253, 785

Baade, W., & Zwicky, F. 1934a, Contributions from the Mount Wilson Observatory, vol. 3, pp.79-83, 3, 79

—. 1934b, Proceedings of the National Academy of Science, 20, 254

Basko, M. 1994, ApJ, 425, 264

Benetti, S., Cappellaro, E., Mazzali, P. A., et al. 2005, ApJ, 623, 1011

Bevan, A., & Barlow, M. J. 2016, MNRAS, 456, 1269

Bikmaev, I. F., Chugai, N. N., Sunyaev, R. A., et al. 2015, Astronomy Letters, 41, 785

Bildsten, L., & Hall, D. M. 2001, ApJ, 549, L219

Bildsten, L., Shen, K. J., Weinberg, N. N., & Nelemans, G. 2007, ApJ, 662, L95

Black, C. S. 2018, PhD thesis, Dartmouth College

Black, C. S., Fesen, R. A., & Parrent, J. T. 2016, Monthly Notices of the Royal Astronomical Society, 462, 649

Black, C. S., Fesen, R. A., & Parrent, J. T. 2018, ArXiv e-prints, arXiv:1810.06788

Blondin, S., Dessart, L., & Hillier, D. J. 2018, MNRAS, 474, 3931

Blondin, S., Dessart, L., Hillier, D. J., & Khokhlov, A. M. 2013, MNRAS, 429, 2127

—. 2017, ArXiv e-prints, arXiv:1706.01901

Blondin, S., & Tonry, J. L. 2007, ApJ, 666, 1024

Blondin, S., Matheson, T., Kirshner, R. P., et al. 2012, AJ, 143, 126

Botyánszki, J., & Kasen, D. 2017, ApJ, 845, 176

Bowers, E. J. C., Meikle, W. P. S., Geballe, T. R., et al. 1997, MNRAS, 290, 663

Branch, D. 1986, ApJ, 300, L51

Branch, D., Chau Dang, L., & Baron, E. 2009, PASP, 121, 238

Branch, D., Fisher, A., & Nugent, P. 1993, AJ, 106, 2383

Branch, D., Dang, L. C., Hall, N., et al. 2006, PASP, 118, 560

Burrows, A. 2013, Rev. Mod. Phys., 85, 245

Burrows, A., Hayes, J., & Fryxell, B. A. 1995, ApJ, 450, 830

Burrows, A., & The, L.-S. 1990, ApJ, 360, 626

Bussard, R. W., Burrows, A., & The, L. S. 1989, ApJ, 341, 401

Cardelli, J. A., Clayton, G. C., & Mathis, J. S. 1989, ApJ, 345, 245

Childress, M. J., Filippenko, A. V., Ganeshalingam, M., & Schmidt, B. P. 2014, MNRAS, 437, 338

Childress, M. J., Scalzo, R. A., Sim, S. A., et al. 2013, ApJ, 770, 29

Childress, M. J., Hillier, D. J., Seitenzahl, I., et al. 2015, MNRAS, 454, 3816

Chugai, N. N. 1992, Soviet Astronomy Letters, 18, 168

Churazov, E., Sunyaev, R., Isern, J., et al. 2014, Nature, 512, 406

—. 2015, ApJ, 812, 62

Ciaraldi-Schoolmann, F., Seitenzahl, I. R., & Röpke, F. K. 2013, A&A, 559, A117

Cohen, D. H., Leutenegger, M. A., Wollman, E. E., et al. 2010, MNRAS, 405, 2391

Cohen, D. H., Wollman, E. E., Leutenegger, M. A., et al. 2014, MNRAS, 439, 908

Colgate, S. A., & McKee, C. 1969, ApJ, 157, 623

Colgate, S. A., & White, R. H. 1966, ApJ, 143, 626

Contardo, G., Leibundgut, B., & Vacca, W. D. 2000, A&A, 359, 876

Contreras, C., Hamuy, M., Phillips, M. M., et al. 2010, AJ, 139, 519

Cook, W. R., Palmer, D., Prince, T., et al. 1988, IAU Circ., 4527

Darnley, M. J., Henze, M., Steele, I. A., et al. 2015, A&A, 580, A45

Dessart, L., Blondin, S., Hillier, D. J., & Khokhlov, A. 2014a, MNRAS, 441, 532

—. 2014b, MNRAS, 441, 532

Dessart, L., & Hillier, D. J. 2005a, A&A, 439, 671

—. 2005b, A&A, 437, 667

—. 2008, MNRAS, 383, 57

—. 2010, MNRAS, 405, 2141

Dessart, L., Hillier, D. J., Blondin, S., & Khokhlov, A. 2014c, MNRAS, 441, 3249

Dessart, L., Hillier, D. J., Li, C., & Woosley, S. 2012, MNRAS, 424, 2139

Dessart, L., Hillier, D. J., & Wilk, K. D. 2018, A&A, 619, A30

Diamond, T. R., Hoeflich, P., Hsiao, E. Y., et al. 2018, ApJ, 861, 119

Dick, S. J. 2013, Discovery and classification in astronomy: controversy and consensus (New york, NY, USA: Cambridge University Press)

Elias, J. H., Matthews, K., Neugebauer, G., & Persson, S. E. 1985, ApJ, 296, 379

Ellis, R. S., Sullivan, M., Nugent, P. E., et al. 2008, ApJ, 674, 51

Filippenko, A. V. 1997, ARA&A, 35, 309

Fink, M., Hillebrandt, W., & Röpke, F. K. 2007, AAP, 476, 1133

Fink, M., Röpke, F. K., Hillebrandt, W., et al. 2010, AAP, 514, A53

Foley, R. J., & Kirshner, R. P. 2013, ApJ, 769, L1

Foley, R. J., Pan, Y.-C., Brown, P., et al. 2016, MNRAS, 461, 1308

Fransson, C., & Jerkstrand, A. 2015, ApJ, 814, L2

Friedman, A. S., Wood-Vasey, W. M., Marion, G. H., et al. 2015, ApJS, 220, 9

Friesen, B., Baron, E., Wisniewski, J. P., et al. 2014, ApJ, 792, 120

Friesen, B., Baron, E., Parrent, J. T., et al. 2017, MNRAS, 467, 2392

Galbany, L., Hamuy, M., Phillips, M. M., et al. 2016, AJ, 151, 33

Gamezo, V. N., Khokhlov, A. M., & Oran, E. S. 2005, APJ, 623, 337

Ganeshalingam, M., Li, W., Filippenko, A. V., et al. 2010, ApJS, 190, 418

Gerardy, C. L. 2002, PhD thesis, DARTMOUTH COLLEGE

Gerardy, C. L., Höflich, P., Fesen, R. A., et al. 2004, ApJ, 607, 391

Gerardy, C. L., Meikle, W. P. S., Kotak, R., et al. 2007, ApJ, 661, 995

Golombek, I., & Niemeyer, J. C. 2005, A&A, 438, 611

Graham, M. L., Kumar, S., Hosseinzadeh, G., et al. 2017, MNRAS, 472, 3437

Green, D. A. 2015, in Astrophysics and Space Science Proceedings, Vol. 43, New Insights From Recent Studies in Historical Astronomy: Following in the Footsteps of F. Richard Stephenson, ed. W. Orchiston, D. A. Green, & R. Strom, 91–100

Guillochon, J., Parrent, J., Kelley, L. Z., & Margutti, R. 2017, ApJ, 835, 64

Hauschildt, P. H. 1992, J. Quant. Spec. Radiat. Transf., 47, 433

Hawley, W. P., Athanassiadou, T., & Timmes, F. X. 2012, ApJ, 759, 39

Hicken, M., Challis, P., Jha, S., et al. 2009, ApJ, 700, 331

Hicks, E. P. 2015, ApJ, 803, 72

Hillier, D. J. 1987, ApJS, 63, 947

—. 1990, A&A, 231, 116

Hillier, D. J., & Dessart, L. 2012, MNRAS, 424, 252

Hillier, D. J., & Miller, D. L. 1998, APJ, 496, 407

—. 1999, ApJ, 519, 354

Hillman, Y., Prialnik, D., Kovetz, A., & Shara, M. M. 2016, ApJ, 819, 168

Hoeflich, P., & Khokhlov, A. 1996, ApJ, 457, 500

Hoeflich, P., Khokhlov, A., & Mueller, E. 1992, A&A, 259, 549

—. 1994, ApJS, 92, 501

Hoeflich, P., Khokhlov, A., Wheeler, J. C., et al. 1996a, ApJ, 472, L81

—. 1996b, ApJ, 472, L81

Hoeflich, P., Mueller, E., & Khokhlov, A. 1993, A&AS, 97, 221

Hoeflich, P., Wehrse, R., & Shaviv, G. 1986, A&A, 163, 105

Hoeflich, P., Hsiao, E. Y., Ashall, C., et al. 2017, ApJ, 846, 58

Höflich, P., Gerardy, C. L., Fesen, R. A., & Sakai, S. 2002, ApJ, 568, 791

Höflich, P., Wheeler, J. C., & Thielemann, F. K. 1998, ApJ, 495, 617

Höflich, P., Krisciunas, K., Khokhlov, A. M., et al. 2010, ApJ, 710, 444

Houck, J., & Fransson, C. 1992, in Bulletin of the American Astronomical Society, Vol. 24, American Astronomical Society Meeting Abstracts, 1243

Hoyle, F., & Fowler, W. A. 1960, APJ, 132, 565

Hubeny, I., & Mihalas, D. 2014, Theory of Stellar Atmospheres: An Introduction to Astrophysical Non-equilibrium Quantitative Spectroscopic Analysis, Princeton Series in Astrophysics (Princeton University Press)

Iben, Jr., I., & Tutukov, A. V. 1984, ApJS, 54, 335

Iwamoto, K., Brachwitz, F., Nomoto, K., et al. 1999, ApJS, 125, 439

Jackson, A. P., Calder, A. C., Townsley, D. M., et al. 2010, APJ, 720, 99

Janka, H.-T. 2012, Annual Review of Nuclear and Particle Science, 62, 407

—. 2017, Neutrino-Driven Explosions, ed. A. W. Alsabti & P. Murdin, 1095

Janka, H.-T., & Mueller, E. 1996, A&A, 306, 167

Jeffery, D. J. 1998, ArXiv Astrophysics e-prints, astro-ph/9811356

Jerkstrand, A. 2017, Spectra of Supernovae in the Nebular Phase, ed. A. W. Alsabti & P. Murdin, 795

Jha, S., Riess, A. G., & Kirshner, R. P. 2007, ApJ, 659, 122

Jordan, IV, G. C., Perets, H. B., Fisher, R. T., & van Rossum, D. R. 2012, ApJ, 761, L23

Karachentsev, I. D., & Kashibadze, O. G. 2006, Astrophysics, 49, 3

Kasen, D. 2006, ApJ, 649, 939

Kasen, D., Röpke, F. K., & Woosley, S. E. 2009, Nature, 460, 869

Kasen, D., Thomas, R. C., & Nugent, P. 2006, ApJ, 651, 366

Khokhlov, A. M. 1991a, AAP, 245, 114

—. 1991b, AAP, 245, L25

Kozma, C., Fransson, C., Hillebrandt, W., et al. 2005, A&A, 437, 983

Krisciunas, K., Phillips, M. M., Suntzeff, N. B., et al. 2004, AJ, 127, 1664

Krisciunas, K., Garnavich, P. M., Stanishev, V., et al. 2007, AJ, 133, 58

Krisciunas, K., Li, W., Matheson, T., et al. 2011, AJ, 142, 74

Kromer, M., Sim, S. A., Fink, M., et al. 2010, ApJ, 719, 1067

Kromer, M., Fink, M., Stanishev, V., et al. 2013, MNRAS, 429, 2287

Kushnir, D., Katz, B., Dong, S., Livne, E., & Fernández, R. 2013, ApJ, 778, L37

Leloudas, G., Stritzinger, M. D., Sollerman, J., et al. 2009, A&A, 505, 265

Lentz, E. J., Baron, E., Branch, D., Hauschildt, P. H., & Nugent, P. E. 2000, ApJ, 530, 966

Leonard, D. C., Li, W., Filippenko, A. V., Foley, R. J., & Chornock, R. 2005, ApJ, 632, 450

Li, H., McCray, R., & Sunyaev, R. A. 1993, ApJ, 419, 824

Livne, E., & Arnett, D. 1995, APJ, 452, 62

Livne, E., Asida, S. M., & Höflich, P. 2005, APJ, 632, 443

Macfarlane, J. J., Cassinelli, J. P., Welsh, B. Y., et al. 1991, ApJ, 380, 564

Madison, D. R., Baek, M., & Li, W. 2005, Central Bureau Electronic Telegrams, 233

Maeda, K. 2006, ApJ, 644, 385

Maeda, K., Röpke, F. K., Fink, M., et al. 2010a, ApJ, 712, 624

Maeda, K., Benetti, S., Stritzinger, M., et al. 2010b, Nature, 466, 82

Maguire, K. 2017, Type Ia Supernovae, ed. A. W. Alsabti & P. Murdin, 293

Maguire, K., Sim, S. A., Shingles, L., et al. 2018, MNRAS, 477, 3567

Maier, A., & Niemeyer, J. C. 2006, A&A, 451, 207

Makino, F., & Moore, G. K. 1987, IAU Circ., 4447

Maoz, D., Mannucci, F., & Nelemans, G. 2014, Annual Review of Astronomy and Astrophysics, 52, 107

Matz, S. M., Share, G. H., & Chupp, E. L. 1988a, IAU Circ., 4568

—. 1988b, IAU Circ., 4618

—. 1988c, IAU Circ., 4667

Matz, S. M., Share, G. H., Leising, M. D., et al. 1988d, Nature, 331, 416

Mazzali, P. A., Ashall, C., Pian, E., et al. 2018, MNRAS, 476, 2905

Mazzali, P. A., Benetti, S., Stehle, M., et al. 2005a, MNRAS, 357, 200

Mazzali, P. A., Cappellaro, E., Danziger, I. J., Turatto, M., & Benetti, S. 1998, ApJ, 499, L49

Mazzali, P. A., & Hachinger, S. 2012, MNRAS, 424, 2926

Mazzali, P. A., Maurer, I., Stritzinger, M., et al. 2011, MNRAS, 416, 881

Mazzali, P. A., & Podsiadlowski, P. 2006, MNRAS, 369, L19

Mazzali, P. A., Benetti, S., Altavilla, G., et al. 2005b, ApJ, 623, L37

Mazzali, P. A., Sullivan, M., Filippenko, A. V., et al. 2015, MNRAS, 450, 2631

Mezzacappa, A., Calder, A. C., Bruenn, S. W., et al. 1998, ApJ, 495, 911

Mihalas, D. 1980, ApJ, 237, 574

Milne, P. A., Hungerford, A. L., Fryer, C. L., et al. 2004, ApJ, 613, 1101

Minkowski, R. 1941, PASP, 53, 224

Morozova, V., Piro, A. L., & Valenti, S. 2017, ApJ, 838, 28

Mueller, E., Hoeflich, P., & Khokhlov, A. 1991, A&A, 249, L1

Müller, B. 2017, in IAU Symposium, Vol. 329, The Lives and Death-Throes of Massive Stars, ed. J. J. Eldridge, J. C. Bray, L. A. S. McClelland, & L. Xiao, 17–24

Nakano, S., Kushida, R., & Kushida, Y. 1995, IAU Circ., 6134

Ng, K. 1974, The Journal of Chemical Physics, 61, 2680

Nomoto, K. 1982, ApJ, 253, 798

—. 1984, ApJ, 277, 791

Nomoto, K., Sugimoto, D., & Neo, S. 1976, APSS, 39, L37

Nugent, P., Baron, E., Branch, D., Fisher, A., & Hauschildt, P. H. 1997, ApJ, 485, 812

Nugent, P., Phillips, M., Baron, E., Branch, D., & Hauschildt, P. 1995, ApJ, 455, L147

Nugent, P. E., Sullivan, M., Cenko, S. B., et al. 2011, Nature, 480, 344

Olson, G. L., & Kunasz, P. B. 1987, J. Quant. Spec. Radiat. Transf., 38, 325

Osterbrock, D., & Ferland, G. 2006, Astrophysics Of Gas Nebulae and Active Galactic Nuclei (University Science Books)

Owocki, S. P., & Cohen, D. H. 2001, ApJ, 559, 1108

Pakmor, R., Kromer, M., Röpke, F. K., et al. 2010, Nature, 463, 61

Pan, Y.-C., Sullivan, M., Maguire, K., et al. 2015, MNRAS, 446, 354

Parrent, J. T., Thomas, R. C., Fesen, R. A., et al. 2011, ApJ, 732, 30

Pereira, R., Thomas, R. C., Aldering, G., et al. 2013, A&A, 554, A27

Perlmutter, S., Aldering, G., Goldhaber, G., et al. 1999, APJ, 517, 565

Phillips, M. M. 1993, ApJ, 413, L105

Phillips, M. M., Li, W., Frieman, J. A., et al. 2007, PASP, 119, 360

Pinto, P. A., & Eastman, R. G. 2000a, ApJ, 530, 744

—. 2000b, ApJ, 530, 757

Pinto, P. A., & Woosley, S. E. 1988a, Nature, 333, 534

—. 1988b, ApJ, 329, 820

Plewa, T., Calder, A. C., & Lamb, D. Q. 2004, APJL, 612, L37

Pomraning, G. 1973, The Equations of Radiation Hydrodynamics, Dover books on physics (Dover Publications)

Porter, A. L., Leising, M. D., Williams, G. G., et al. 2016, ApJ, 828, 24

Pozdnyakov, L. A., Sobol, I. M., & Syunyaev, R. A. 1983, Astrophysics and Space Physics Reviews, 2, 189

Riess, A. G., Filippenko, A. V., Challis, P., et al. 1998, AJ, 116, 1009

Riess, A. G., Kirshner, R. P., Schmidt, B. P., et al. 1999, AJ, 117, 707

Riess, A. G., Li, W., Stetson, P. B., et al. 2005, ApJ, 627, 579

Romanik, C. J., & Leung, C. M. 1981, ApJ, 246, 935

Röpke, F. K., & Niemeyer, J. C. 2007, AAP, 464, 683

Ruiz-Lapuente, P., Kirshner, R. P., Phillips, M. M., et al. 1995, ApJ, 439, 60

Ruiz-Lapuente, P., Lucy, L. B., & Danziger, I. J. 1992, Mem. Soc. Astron. Italiana, 63, 233

Saio, H., & Nomoto, K. 1985, A&A, 150, L21

Sasdelli, M., Mazzali, P. A., Pian, E., et al. 2014, MNRAS, 445, 711

Sato, Y., Nakasato, N., Tanikawa, A., et al. 2015, ApJ, 807, 105

Scalzo, R., Aldering, G., Antilogus, P., et al. 2012, ApJ, 757, 12

—. 2014a, MNRAS, 440, 1498

Scalzo, R. A., Ruiter, A. J., & Sim, S. A. 2014b, MNRAS, 445, 2535

Seitenzahl, I. R., Ciaraldi-Schoolmann, F., Röpke, F. K., et al. 2013, MNRAS, 429, 1156

Seitenzahl, I. R., Kromer, M., Ohlmann, S. T., et al. 2016, A&A, 592, A57

Shen, K. J., & Bildsten, L. 2014, ApJ, 785, 61

Silverman, J. M., Vinkó, J., Marion, G. H., et al. 2015, MNRAS, 451, 1973

Silverman, J. M., Foley, R. J., Filippenko, A. V., et al. 2012, MNRAS, 425, 1789

Sim, S. A. 2007, MNRAS, 375, 154

Sim, S. A., & Mazzali, P. A. 2008, MNRAS, 385, 1681

Sim, S. A., Röpke, F. K., Hillebrandt, W., et al. 2010, ApJ, 714, L52

Sim, S. A., Röpke, F. K., Kromer, M., et al. 2013a, in IAU Symposium, Vol. 281, Binary Paths to Type Ia Supernovae Explosions, ed. R. Di Stefano, M. Orio, & M. Moe, 267–274

Sim, S. A., Seitenzahl, I. R., Kromer, M., et al. 2013b, MNRAS, 436, 333

Smareglia, R., & Mazzali, P. A. 1997, in Astronomical Society of the Pacific Conference Series, Vol. 125, Astronomical Data Analysis Software and Systems VI, ed. G. Hunt & H. Payne, 226

Srivastav, S., Ninan, J. P., Kumar, B., et al. 2016, MNRAS, 457, 1000

Starrfield, S., Truran, J. W., Sparks, W. M., & Kutter, G. S. 1972, ApJ, 176, 169

Stehle, M., Mazzali, P. A., Benetti, S., & Hillebrandt, W. 2005, MNRAS, 360, 1231

Stephenson, F. R., & Clark, D. H. 1976, Scientific American, 234, 100

Stritzinger, M., Leibundgut, B., Walch, S., & Contardo, G. 2006, A&A, 450, 241

Sullivan, M., Ellis, R. S., Howell, D. A., et al. 2009, ApJ, 693, L76

Summa, A., Ulyanov, A., Kromer, M., et al. 2013, A&A, 554, A67

Sunyaev, R., Kaniovsky, A., Efremov, V., et al. 1987, Nature, 330, 227

Swartz, D. A., Sutherland, P. G., & Harkness, R. P. 1995, ApJ, 446, 766

Swift, B., Li, W. D., & Schwartz, M. 2001, IAU Circ., 7611

Tanaka, M., Mazzali, P. A., Maeda, K., & Nomoto, K. 2006, ApJ, 645, 470

Tanaka, Y. 1988, in Lecture Notes in Physics, Berlin Springer Verlag, Vol. 305, IAU Colloq. 108: Atmospheric Diagnostics of Stellar Evolution, ed. K. Nomoto, 399

Taubenberger, S. 2017, The Extremes of Thermonuclear Supernovae, ed. A. W. Alsabti & P. Murdin, 317

Taubenberger, S., Kromer, M., Pakmor, R., et al. 2013a, ApJ, 775, L43

Taubenberger, S., Kromer, M., Hachinger, S., et al. 2013b, MNRAS, 432, 3117

The, L.-S., Burrows, A., & Bussard, R. 1990, ApJ, 352, 731

Thomas, R. C., Kasen, D., Branch, D., & Baron, E. 2002, ApJ, 567, 1037

Travaglio, C., Hillebrandt, W., Reinecke, M., & Thielemann, F.-K. 2004, AAP, 425, 1029

van Dyk, S. D., Treffers, R. R., Richmond, M. W., Filippenko, A. V., & Paik, Y. B. 1994, IAU Circ., 6105

Wagoner, R. V., Perez, C. A., & Vasu, M. 1991, ApJ, 377, 639

Walker, E. S., Hachinger, S., Mazzali, P. A., et al. 2012, MNRAS, 427, 103

Wang, C.-Y. 2008, ApJ, 686, 337

Wang, X., Wang, L., Filippenko, A. V., et al. 2012, ApJ, 749, 126

Webbink, R. F. 1984, ApJ, 277, 355

Wheeler, J. C., & Harkness, R. P. 1990, Reports on Progress in Physics, 53, 1467

Wheeler, J. C., & Levreault, R. 1985, ApJ, 294, L17

Whelan, J., & Iben, Jr., I. 1973, ApJ, 186, 1007

Wilk, K. D., Hillier, D. J., & Dessart, L. 2018, MNRAS, 474, 3187

Wood-Vasey, W. M., Friedman, A. S., Bloom, J. S., et al. 2008, ApJ, 689, 377

Woosley, S. E. 1988, ApJ, 330, 218

—. 1997, ApJ, 476, 801

Woosley, S. E., & Kasen, D. 2011, ApJ, 734, 38

Woosley, S. E., Kasen, D., Blinnikov, S., & Sorokina, E. 2007, ApJ, 662, 487

Woosley, S. E., Taam, R. E., & Weaver, T. A. 1986, ApJ, 301, 601

Woosley, S. E., & Weaver, T. A. 1994, APJ, 423, 371

Zhao, X., Wang, X., Maeda, K., et al. 2015, ApJS, 220, 20